

ROM2F/2003/13 published on Riv. N. Cim. 26 n.1 (2003) 1-73

Dark Matter search

R. Bernabei, P. Belli, F. Cappella, R. Cerulli, F. Montecchia¹, F. Nozzoli

Dip. di Fisica, Universita' di Roma "Tor Vergata" and INFN, sez. Roma2, I-00133 Rome, Italy

A. Incicchitti, D. Prosperi

Dip. di Fisica, Universita' di Roma "La Sapienza" and INFN, sez. Roma, I-00185 Rome, Italy

C.J. Dai, H.H. Kuang, J.M. Ma, Z.P. Ye²

IHEP, Chinese Academy, P.O. Box 918/3, Beijing 100039, China

Abstract

Main arguments on the Dark Matter particle direct detection approach are addressed on the basis of the work and of the results of the $\simeq 100$ kg highly radiopure NaI(Tl) DAMA experiment (DAMA/NaI), which has been operative at the Gran Sasso National Laboratory of the I.N.F.N. for more than one decade, including the preparation. The effectiveness of the WIMP model independent annual modulation signature is pointed out by discussing the results obtained over 7 annual cycles (107731 kg · day total exposure); the WIMP presence in the galactic halo is strongly supported at 6.3σ C.L. The complexity of the corollary model dependent quests for a candidate particle is also addressed and several of the many possible scenarios are examined.

Keywords: Dark Matter; WIMPs; underground Physics

PACS numbers: 95.35.+d

1 The physical problem

1.1 Evidence for Dark Matter in the Universe

The first evidence that much more than the visible matter should fill the Universe dates back to 1933 when F. Zwicky measured the dispersion velocity in the Coma galaxies [1]. This was soon after confirmed by S. Smith studying the Virgo cluster [2]. Nevertheless, only about 50 years later the fact that Dark Matter should be present in large amount in our Universe finally reached a wide consensus.

¹also: Universita' "Campus Biomedico" di Roma, 00155, Rome, Italy

²also: University of Zhao Qing, Guang Dong, China

Particular contribution was given in the seventies by two groups which systematically analysed the dispersion velocity in many spiral galaxies [3]: in fact, the velocity curves in the galaxy plane as a function of distance from the galactic center stay flat even outside the luminous disk, crediting the presence of a dark halo. Several other experimental evidences for the Dark Universe have been pointed out by the progresses – with time passing – in the astronomical observations, such as: i) the Large Magellanic Cloud spins around our Galaxy faster than expected in case only luminous matter would be present; ii) the observation of X-ray emitting gases surrounding elliptical galaxies; iii) the velocity distribution of hot intergalactic plasma in clusters. All these observations have further supported that the mass of the Universe should be much larger than the luminous one in order to explain the observed gravitational effects.

The existence of the Dark Universe is supported also by the standard cosmology (based on the assumption that the Universe arose from an initial singularity and went on expanding) in the inflationary scenario (proposed to avoid any fine tuning in the Big Bang initial conditions), which requires a flat Universe with density equal to the critical one: $\rho_c = \frac{3H_0^2}{8\pi G} = 1.88h^2 \cdot 10^{-29} \text{ g} \cdot \text{cm}^{-3}$, where G is the Newton constant and H_0 is the Hubble constant equal to $100h \text{ kms}^{-1} \text{Mpc}^{-1}$ and $0.55 < h < 0.75$. The uncertainty is due to the measurements of the actual value of the expansion rate of the Universe and to the considered models [4]; a recent determination from the WMAP data gives: $h = 0.72 \pm 0.05$ [5].

In particular, the density parameter $\Omega = \frac{\rho}{\rho_c}$, where ρ is the average density of the Universe (matter + energy), is a key parameter in the interpretation of the data from the measurements on Cosmic Microwave Background (CMB) since the global curvature of the Universe is related to it. The experimental results are consistent with a flat geometry of the Universe and, therefore, also support $\Omega \simeq 1$ [6]; the most recent determination from the WMAP gives: $\Omega = 1.02 \pm 0.02$ [5]. Thus, the scenario is consistent with adiabatic inflationary models and with the presence of acoustic oscillations in the primeval plasma and requires the existence of Dark Matter in the Universe since the average density of the Universe as measured by photometric methods is: $\Omega \simeq 0.007$. However, the detailed composition of Ω in term of matter, Ω_m , and of energy, Ω_Λ , cannot be inferred by CMB data alone; some information can be derived by introducing some other constraints [5, 7].

For the sake of completeness, we also mention that in last years studies have been performed [8] on astronomical standard candles as supernovae type Ia, that allow to evaluate relations between redshift and distance. These studies seem to point out an Universe whose expansion is accelerating, crediting the possible presence of a Dark Energy. When these results are combined with CMB data, Ω_Λ would account for about 70% of Ω [5, 9]. This form of energy, with repulsive gravity and possible strong implication on the future evolution of Universe, would not be a replacement for Dark Matter and is still a mysterious task; dedicated ground and space based experiments are planned in order to confirm this scenario.

Finally, as regards our Galaxy, from dynamical observations one can derive that it is wrapped in a dark halo, whose density nearby the Earth has been estimated to be for example in refs. [10, 11]: $\rho_{\text{halo}} \simeq (0.17 - 1.7) \text{ GeV cm}^{-3}$ (see also later).

1.2 The nature of the Dark Matter

The investigation on the nature of the Dark Universe has shown that large part of it should be in non-baryonic form.

In fact, as regards baryons, in the past from the theory of big-bang nucleosynthesis (BBN) and from a lower limit to the primordial deuterium abundance a baryon density $\Omega_B \lesssim 0.1$ was set [12]. This upper limit has been precised by recent measurements of primordial deuterium abundance, giving $\Omega_B h^2 = 0.020 \pm 0.001$ [13], that combined with the present determination of the Hubble constant implies: $\Omega_B \simeq 0.04$; the latest determination by CBM experiments: $\Omega_B h^2 = 0.022 \pm 0.003$ [5, 7], is also in good agreement. Recently, large efforts have been devoted to the investigation on Dark Baryonic Matter by experiments like EROS, MACHO and OGLE, which search for massive compact halo objects as baryonic candidates looking at microlensing effect toward Large and Small Magellanic Clouds and toward the Milky Way bulge. At present, in agreement with the expectations, the obtained results [14, 15] strongly limit the possible amount of Galactic Dark Matter in this form. In addition, a further argument, which also supports that the major part of the Dark Matter in the Universe should be in non-baryonic form, is the following: it is very difficult to build a model of galaxy formation without the inclusion of non-baryonic Dark Matter.

Thus, a significant role should be played by non-baryonic relic particles from the Big Bang. They must be stable or with a lifetime comparable with the age of the Universe to survive up to now in a significant amount. They must be neutral, undetectable by electromagnetic interactions and their cross section with ordinary matter should be weak (in fact, if their annihilation rate would be greater than the Universe expansion rate, they should disappear). The Dark Matter candidate particles are usually classified in *hot* Dark matter (particles relativistic at decoupling time with masses $\lesssim 30$ eV) and in *cold* Dark Matter (particles non relativistic at temperatures greater than 10^4 K with masses from few GeV to the TeV region or axions generated by symmetry breaking during primordial Universe). The light neutrinos are the natural candidates for *hot* Dark Matter; they are strongly constrained by cosmology and a value over the limit $\Omega_\nu \simeq 0.05$ gives an unacceptable lacking of small-scale structure[16]. In addition, a pure *hot* Dark Matter scenario is also ruled out by the measurements of the CMB radiation, which does not show sufficiently large inhomogeneity.

Thus, *cold* Dark Matter candidates, which can be responsible for the initial gravitational collapse, should be present and in large amount, although a pure *cold* Dark Matter scenario seems to be not favoured by the observed power spectrum of the density perturbation. In practice, a mixed Dark Matter scenario is generally favourably considered. However, other possibilities can be considered such as, for example, the so-called "tilted Dark matter scenario" that introduces a significant deviation from the Zeldovich scale invariance of the power spectrum of the initial fluctuations. Anyhow, in all the possible scenarios a significant fraction of *cold* Dark Matter particles is expected.

As mentioned above, *cold* Dark Matter can be in form of axions or of WIMPs (Weakly Interacting Massive Particles). The axions are light bosons, hypothesized to solve the CP problem in strong interactions. Direct detection experiments are in progress since time by studying their interactions with strong electromagnetic fields,

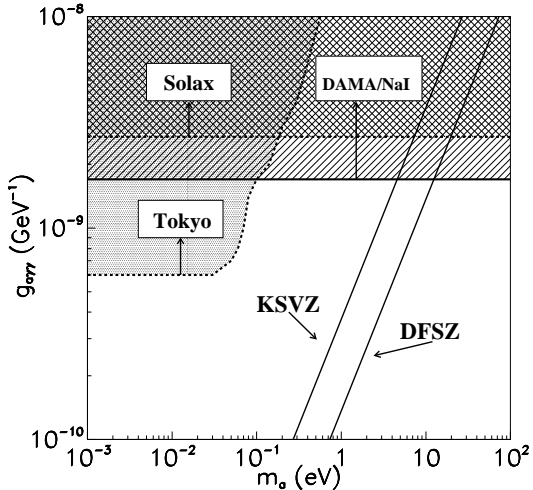


Figure 1: Exclusion plot in the plane axion to photon coupling constant, $g_{a\gamma\gamma}$, versus axion mass, m_a , achieved by DAMA/NaI in ref. [18]. The limit quoted in the paper ($g_{a\gamma\gamma} \leq 1.7 \times 10^{-9} \text{ GeV}^{-1}$ at 90% C.L.) is shown together with the expectations of the KSVZ and DFSZ models; see ref.[18] for details.

but no positive evidence has been found so far [17]. For completeness, we mention that some experiments (including DAMA/NaI, see Fig. 1) have also searched for possible axions produced in the Sun (see e.g. [18, 19]) and that some other will be realized in near future. However, these latter experiments cannot be classified as experiments for Dark Matter direct detection since they are not searching for relic axions.

For the sake of completeness, we remind that also more exotic candidates (which generally could account for small fraction of Dark Matter in the galactic halo) have been considered and searched for, such as e.g. the magnetic monopoles with mass $10^{16} - 10^{17} \text{ GeV}$ [20], the neutral Strongly Interacting Massive particles (SIMPs) and the neutral nuclearities[21, 22, 23], the Q-balls[24], etc.; experimental searches for such candidates have given always negative results. Some of them have also been investigated by DAMA/NaI [22, 24].

2 The particles searched for

The WIMPs are particles in thermal equilibrium in the early stages of the Universe, decoupled at freeze out temperature. Considering the WIMP particles as stable and with the same initial density for particles and antiparticles, their annihilation cross section, σ_{ann} , should be such that their annihilation rate should be lower than the expansion rate of the Universe: $\langle \sigma_{ann} \cdot v \rangle \simeq \frac{10^{-26}}{\Omega_{WIMP} \cdot h^2} \text{ cm}^3 \text{ s}^{-1}$, where v is the relative velocity of the particle-antiparticle pair; thus, the interaction cross section is of the same order as those known of weak interactions. In case the particles and antiparticles would not have the same initial density, this relation would represent a lower limit.

The velocity-spatial distribution of the WIMPs in our galactic halo is not well known. So far the simplest, non-consistent and approximate isothermal sphere model has generally been considered in direct WIMP searches; under this assumption the WIMPs form a dissipationless gas trapped in the gravitational field of our Galaxy in an equilibrium steady state and have a quasi-maxwellian velocity distribution with a cut-off at the escape velocity from the galactic gravitational field. More realistic halo models have been proposed by various authors such as Evans' power-law halos, Michie models with an asymmetric velocity distribution, Maxwellian halos with bulk rotation, etc. [25]. In particular, a devoted discussion on a wide (but still not complete) number of consistent halo models and their implications on available experimental data has been carried out e.g. in refs. [11, 25]; they will be summarized in §7.1.3.

At present, the most widely considered candidate for WIMP is the lightest supersymmetric particle named neutralino, χ . In the Minimal Supersymmetric Standard Model (MSSM) where R-parity is conserved, the lightest SUSY particle, χ , must be stable and can interact neither by electromagnetic nor by strong interactions (otherwise it would condensate and would be detected in the galactic halo with the ordinary matter). The χ is defined as the lowest-mass linear combination of photino ($\tilde{\gamma}$), zino (\tilde{Z}) and higgsinos (\tilde{h}_1, \tilde{h}_2): $\chi = a_1\tilde{\gamma} + a_2\tilde{Z} + a_3\tilde{h}_1 + a_4\tilde{h}_2$ (where $\tilde{\gamma}$ and \tilde{Z} are linear combination of U(1) and SU(2) neutral gauginos, \tilde{B} and \tilde{W}_3) and is a Majorana particle. Under some assumptions, the χ mass and the a_i coefficients depend on the Higgs mass mixing parameter, μ , on the \tilde{B} and \tilde{W}_3 masses and on $tg\beta$ (the ratio between the v.e.v's which give masses to up and down quarks). Thus, often the theoretical estimates and sometimes the experimental results are presented in terms of μ , $tg\beta$ and wino mass, M_2 . The χ cross section on ordinary matter is described by three Feynman diagrams: i) exchange between χ and quarks of the ordinary matter through Higgs particles (spin-independent – SI – interaction); ii) exchange between χ and quarks of the ordinary matter through Z_0 (spin-dependent – SD – interaction); iii) exchange between χ and quarks of the ordinary matter through squark (mixed – SI/SD – interaction). The evaluation of the expected rates for χ depends on several parameters and procedures, which are affected by significant uncertainties, such as e.g. the considered neutralino composition, the present uncertainties on the measured top quark mass and on certain sectors of the fundamental nuclear cross sections, on some lack of information about physical properties related to Higgs bosons and SUSY particles, on the possible use of constraints from GUT schemes and/or from $b \rightarrow s + \gamma$ branching ratio, on the used rescaling procedure, etc.; in conclusion, considering also the large number of involved parameters, the supersymmetric theories have unlikely no practical predictive capability.

Other candidates can also be considered as WIMPs; in particular, we remind an heavy neutrino of a 4-th family [26] and the sneutrino in the scenario described in ref. [27].

The heavy neutrino of a 4-th family was one of the first candidate proposed to solve the Dark Matter problem. Still now it may be considered as a good and realistic candidate, although unable to account for the whole Dark Matter missing mass. Such a neutrino could contribute – by its pair annihilation in the galactic halo – to positrons, antiprotons and diffused gamma background and these signatures might be better fit to the observed data [26]; moreover, it might dominate the Higgs decay mode in near

future LHC accelerator. The cosmological relic abundance of heavy neutrinos can be

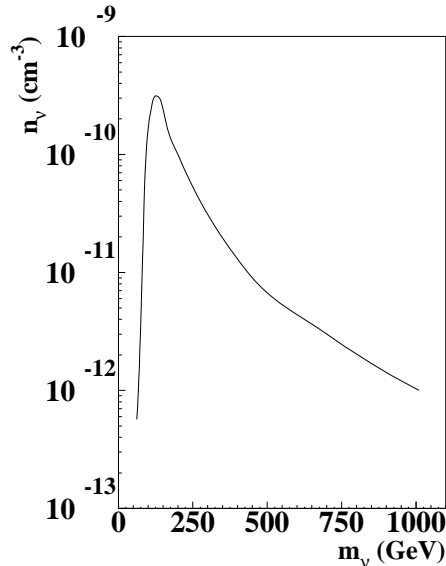


Figure 2: Relic abundance of an heavy neutrino as a function of its mass according to the calculation of ref. [28]; masses above the Z_0 pole are considered.

evaluated, as reported in Fig. 2, taking into account that the couplings are described within the Standard Model of elementary particles. Applying the condition that the density of such heavy neutrinos cannot exceed the critical density, a window in their mass can be evaluated [29]: $3 \text{ GeV} < m_\nu < 3 \text{ TeV}$. Considering the measurements of Z_0 decay into invisible channels carried out at LEP and some implications of the measured cosmic ray flux [28], a mass range around 50 GeV with a reasonable local abundance (which permits to consider it as a Dark Matter candidate) is still open.

In some supersymmetric models the lightest supersymmetric particle (LSP) can be the sneutrino, $\tilde{\nu}$, the spin-0 partner of the neutrino. In supersymmetric theories with no violation of leptonic number, a sneutrino with mass in the range $550 \text{ GeV} \lesssim m_{\tilde{\nu}} \lesssim 2300 \text{ GeV}$ could have a relevant cosmological abundance ($0.1 \lesssim \Omega_{\tilde{\nu}} h^2 \lesssim 1$) [30]; however, because of its large interaction cross sections, the sneutrino cannot generally be considered as major component of Cold Dark Matter. Anyhow, a sneutrino as a candidate remains still possible in supersymmetric models with violation of lepton number [31]. In this framework the sneutrino can exist in two mass states, $\tilde{\nu}_\pm$, with a $\delta \simeq \Delta m^2 / 2m_{\tilde{\nu}}$ mass splitting (for $\Delta m^2 \ll m_{\tilde{\nu}}^2$), being Δm^2 a term introduced by the leptonic number violating operator. The two mass eigenstates have off-diagonal coupling with Z_0 boson and only couplings between $\tilde{\nu}_+$ e $\tilde{\nu}_-$ exist. As a consequence, the elastic scattering cross section on nuclei is extremely low [31] and sneutrinos with mass around 40-80 GeV and δ about 5 GeV could have cosmological relic abundance in the range 0.1-1 [31]. Moreover, whatever scalars would be introduced in the theory, they can mix with sneutrinos and, consequently, the gauge interaction would be

reduced through the mixing angle [32]. The suppression of this interaction implies a sizeable relic abundance of the sneutrino even for low δ values (e.g. around ~ 100 keV). A similar sneutrino has been proposed as a possible WIMP candidate providing – through the transition from lower to upper mass eigenstate – inelastic scattering with nuclei [27] (see also later).

Finally, we remind that – in principle – even whatever massive and weakly interacting particle, not yet foreseen by theories, can be a good candidate as WIMP.

In the following we will focus our attention on the WIMP direct detection technique in underground laboratory, where the low environmental background allows to reach the highest sensitivity; this is the process investigated by DAMA/NaI. We will later mention few arguments on the indirect detection approach, mainly in the light of some recent analyses.

3 Some general arguments on the WIMP direct detection approach

The WIMP direct detection approach mainly investigates the WIMP elastic scattering on the nuclei of a target-detector; the recoil energy is the measured quantity. In fact, the additional possibility to investigate the WIMP-nucleus inelastic scattering producing low-lying excited nuclear states (originating successive de-excitation gamma rays and, thus, presence of characteristic peaks in the measured energy spectrum) is disfavoured by the very small expected counting rate; for this reason, only few preliminary efforts have been carried out so far on this subject[33, 34, 35].

In the following subsections only few general arguments are addressed on the direct detection approach, while we simply remind that most experienced detection techniques have already been briefly commented in ref. [36], mainly in the light of a possible effective search for a WIMP signature.

3.1 Some generalities

A direct search for Dark Matter particles requires: i) a suitable deep underground site to reduce at most the background contribution from cosmic rays; ii) a suitable low background hard shield against electromagnetic and neutron background; iii) a deep selection of low background materials and a suitable identification of radio-purification techniques to build a low background set-up; iv) severe protocols and rules for building, transporting, handling, installing the detectors; v) an effective Radon removal system and control on the environment nearby the detectors; vi) a good model independent signature; vii) an effective monitoring of the running conditions at the level of accuracy required by the investigated WIMP signature.

As an example of the suitable performances of a deep underground laboratory we remind those measured at the Gran Sasso National Laboratory of I.N.F.N. where the DAMA/NaI experiment has been carried out: i) muon flux: $0.6 \text{ muons m}^{-2} \text{ h}^{-1}$ [37]; ii) thermal neutron flux: $1.08 \cdot 10^{-6} \text{ neutrons cm}^{-2} \text{ s}^{-1}$ [38]; iii) epithermal neutron

flux: $1.98 \cdot 10^{-6}$ neutrons $\text{cm}^{-2} \text{ s}^{-1}$ [38]; iv) fast ($E_n > 2.5 \text{ MeV}$) neutron flux: $0.09 \cdot 10^{-6}$ neutrons $\text{cm}^{-2} \text{ s}^{-1}$ [39]; v) Radon in the hall: $\simeq 10\text{-}30 \text{ Bq m}^{-3}$ [40].

The low background technique requires very long and accurate work for the selection of low radioactive materials by sample measurements with HP-Ge detectors (placed deep underground in suitable hard shields) and/or by mass spectrometer analyses; thus, these measurements are often difficult experiments themselves, depending on the required level of radiopurity. In addition, uncertainties due to the sampling procedures and to the subsequent handling of the selected materials to build the apparatus also require further time and efforts. As an example of an investigation of materials and detector radiopurity, one can consider ref. [41], where the residual radioactivity measured in materials and detectors developed for DAMA/NaI is reported. Moreover, some arguments on how to further improve the radiopurity of NaI(Tl) detectors (largely followed e.g. in the developments of the new DAMA/LIBRA set-up, now in test runs) can be found e.g. in ref. [42]. An interesting paper on the low background techniques is also e.g. ref. [43].

Main efforts regard the reduction of standard contaminants: ^{238}U and ^{232}Th (because of their rich chains) and ^{40}K (because of its large presence in nature). When suitable radiopurity is reached for these components, the possible presence of non-standard contaminants should be also seriously investigated by devoted measurements. As shown e.g. in ref. [44] for the case of a ionizing Ge experiment, several orders of magnitude of rate reduction can be obtained with time and efforts in improving the experimental conditions.

3.2 The "traditional" model dependent approach

Since often the used statistics in direct experiments is very poor, the simple comparison of the measured energy distribution with an expectation from a given model framework is carried out. This "traditional" approach – the only one which can be pursued by either small scale or very poor duty cycle experiments – allows only to calculate model dependent limits on WIMP-nucleus cross section at given C.L.. In fact, although for long time the limits achieved by this approach have been presented as robust reference points, similar results are quite uncertain not only because of possible underestimated systematics when relevant data handling and reduction is performed, but also because the result refers only to a specific model framework. In fact the model is identified not only by the general astrophysical, nuclear and particle physics assumptions, but also by the needed theoretical and experimental parameters and by the set of values chosen in the calculations for them. Some of these parameters, such as the WIMP local velocity, v_0 , and other halo parameters, form factors' parameters, quenching factor, etc. are also affected by significant uncertainties. Therefore the calculation of the expected differential rate, which has to be compared with the experimental one in order to evaluate an exclusion plot in the plane WIMP cross section versus WIMP mass, is strongly model dependent. As an example, Fig. 3 shows how an exclusion plot is modified by changing (within the intervals allowed by the present determinations) the values of the astrophysical velocities [45]. Analogous effects will be obtained when varying – within allowed values – every other of the several needed parameters as well as when varying every one of the general assumptions considered in the calcu-

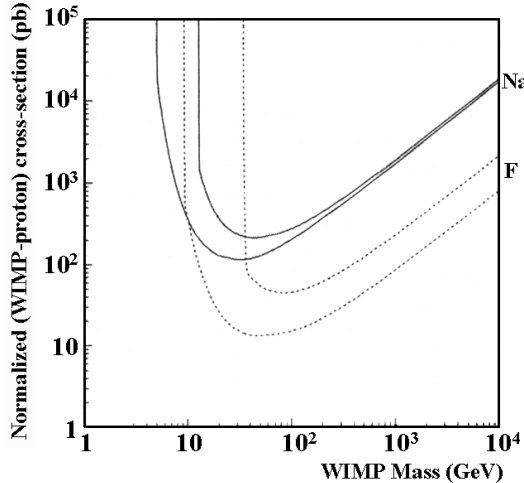


Figure 3: Example of the effects due to the uncertainties in a given model framework when calculating exclusion plots. Here the simple case for the halo local velocity, v_0 , and the escape velocity, v_{esc} , is shown in case of spin-dependent coupled WIMPs as from ref. [45]. The top curve for each nucleus has been calculated – in a given model framework – assuming $v_0 = 180$ km/s and $v_{esc} = 500$ km/s, while the lower one has been calculated assuming $v_0 = 250$ km/s and $v_{esc} = 1000$ km/s; all the considered values are possible at present stage of knowledge. Analogous effects will be found for every kind of experimental result when varying experimental/theoretical parameters/assumption for whatever target-nucleus.

lations. Thus, each exclusion plot should be considered only strictly correlated with the "cooking list" of the used experimental/theoretical assumptions and parameters as well as with detailed information on possible data reduction/selection, on efficiencies, calibration procedures, etc. Moreover, since WIMP-nucleus cross sections on different nuclei cannot directly be compared, generally cross sections normalized to the WIMP-nucleon one are presented; this adds further uncertainties in the results and in the comparisons, requiring the assumptions of scaling laws ³.

Thus, comparisons should be very cautious since they have not an universal character. In addition, different experiments can have e.g. different sensitivity to the different possible WIMP couplings.

In conclusion, this model dependent approach has no general meaning, no potentiality of discovery and - by its nature - can give only "negative" results. Therefore, experiments offering model independent signature for WIMP presence in the galactic halo are mandatory.

³We take this occasion also to stress that exclusion plots given in terms of cross sections on nucleus are not model independent as quoted sometimes "traditionally" in literature, since they depend e.g. on the considered halo model, on the considered nuclear form factors, etc.

3.2.1 ... with electromagnetic background rejection technique

In order to overcome the long and difficult work of developing very low background set-ups, strategies to reject electromagnetic background from the data are sometimes pursued. This can be realized in several scintillators by pulse shape discrimination (since electrons show a different decay time respect to nuclear recoils, as carried out in NaI(Tl) and LXe e.g. by DAMA/NaI in ref. [46] and by DAMA/LXe in ref. [47]) or by comparing, for the same event, two different signals (when the recoil/electron response ratio is expected to be different, such as heat/ionization in Ge or Si [48, 49] and heat/light in CaWO₄ [50, 51]). The first case offers a relatively safer approach than the second one since basic quantities (such as e.g. the sensitive volume) are well defined, while the second one is more uncertain. Just as an example, in case of heat/ionization read-out the precise knowledge of the effective sensitive volume for each one of the two signals and the related efficiencies as a function of the energy are required. A further discrimination strategy, which uses a two-phases gas/liquid Xenon detector with an applied electric field, has been also suggested for future experiments; there the light amplitudes of the primary and of the secondary scintillation pulses are compared [52]. However, in this case the discrimination critically depends e.g. on the definition of the real sensitive volume, on the dependence of the discrimination power with ionization position, on gas purity, etc.

In every case, whatever strategy is followed, always only a statistical discrimination is possible (on the contrary of what is often claimed) because e.g. of tail effects from the two populations, from the noise, etc. Furthermore, the existence of known concurrent processes (due e.g. to end-range alphas, neutrons, fission fragments or in some case also the so-called surface electrons), whose contribution cannot be estimated and subtracted in any reliable manner at the needed level of precision, excludes that an unambiguous result on WIMP presence can be obtained following a similar approach.

Moreover, when using similar procedures, the real reached sensitivity is based e.g. on the proper estimate of the systematic errors, on the accuracy of all the involved procedures and on the proper accounting of all the related efficiencies, on the proper knowledge of the energy scale and energy threshold (see also §7.1.6) and on the verified stability of the running conditions. Consider e.g. the difficulty to manage the efficiency due to the coincidence of the few keV heat/ionization or heat/scintillation signals or, in case of the two-phases LXe detectors, the triggering of the primary and secondary scintillations. We note also that sometimes in literature some methodologically incorrect methods are also considered which allow to claim for a larger sensitivity than the correct one.

In conclusion, the possibility to achieve a control of the systematic error in rejection procedures at level of $\simeq 10^{-4}$, as it has recently been claimed (see §5.1.1), appears unlikely whatever rejection approach would be considered.

Finally, it is worth to note that rejection strategies cannot safely be applied to the data when a model independent signature based on the correlation of the measured experimental rate with the Earth galactic motion is pursued (see later); in fact, the effect searched for (which is typically at level of few %) would be largely affected by the uncertainties associated to the – always statistical – rejection procedure. On the other hand the signature itself acts as an effective background rejection as pointed out

e.g. for the WIMP annual modulation signature since ref. [53].

3.3 An unambiguous signature for WIMPs in the galactic halo is needed

To obtain a reliable signature for WIMPs is necessary to follow a suitable model independent approach. In principle, three main possibilities exist; they are based on the correlation between the distribution of the events, detected in a suitable underground set-up, with the galactic motion of the Earth.

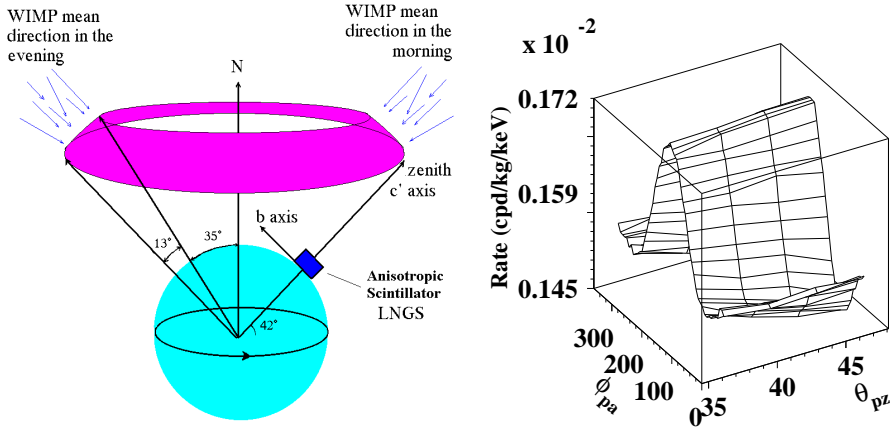


Figure 4: Left: schematic representation of the experimental approach considered in ref. [54] to investigate the correlation between the recoil direction and the Earth velocity direction by using anisotropic scintillators. The anisotropic scintillator is placed ideally at LNGS with c' axis in the vertical direction and b axis pointing to the North. The area in the sky from which the WIMPs are preferentially expected is highlighted. Right: expected rate, in the 3-4 keV energy window, versus the detector (or Earth) possible velocity directions. This example refers to the particular assumptions of a WIMP mass equal to 50 GeV, a WIMP-proton cross section equal to $3 \cdot 10^{-6}$ pb and to the model framework of ref. [54]. The dependence on the “polar-azimuth” angle (ϕ_{pa}) induces a diurnal variation of the rate.

The first one correlates the recoil direction with that of the Earth velocity, but it is practically discarded mainly because of the technical difficulties in reliably and efficiently detecting the short recoil track. Few R&D attempts have been carried out so far such as e.g. [55, 56], while a suggestion – based on the use of anisotropic scintillators – was originally proposed by DAMA collaborators in ref. [57] and recently revisited in ref. [54]. As an example, Fig. 4 (left) shows a schematic representation of the experimental approach studied in ref. [54]; an example of the dependence of the expected rate on the WIMP arrival direction, with respect to the crystal axes, for the considered experimental case is given in Fig.4 (right).

The second approach correlates the time occurrence of each event with the diurnal rotation of the Earth. In fact, a diurnal variation of the low energy rate in WIMP direct searches can be expected during the sidereal day since the Earth shields a given detector with a variable thickness, eclipsing the WIMP “wind” [58]. However, this effect can be appreciable only for relatively high cross section candidates and, therefore, it can only test a limited range of Cold Dark Matter halo density. For a recent experimental result see e.g. ref. [59], where a statistics of 14962 kg·day collected by DAMA/NaI has been investigated in the light of this signature. As an example the dependence of θ (the angle defined by the Earth velocity in the Galactic frame with the vector joining the center of the Earth to the position of the laboratory) on the sidereal time, is shown in Fig. 5(left) in case of the Gran Sasso National Laboratory location. The expected signal rate, in case of the experimental set-up and assumptions quoted in ref. [59], is given in Fig. 5 (right).

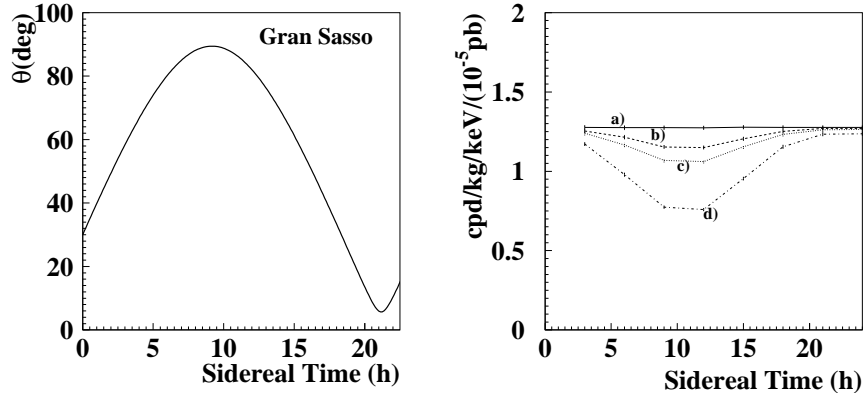


Figure 5: Schematic description of the approach which correlates the time occurrence of each event with the diurnal rotation of the Earth. Left: the θ angle (defined by the Earth velocity in the Galactic frame with the vector joining the center of the Earth to the position of the laboratory) as a function of the sidereal time; here the case for the Gran Sasso National Laboratory of the I.N.F.N. is considered. Right: signal rate expected in the 2–6 keV energy interval when assuming a 60 GeV WIMP mass, a WIMP-proton cross section equal to: a) $7.0 \cdot 10^{-6}$ pb, b) $5 \cdot 10^{-2}$ pb, c) 10^{-1} pb, d) 1.0 pb, and the model framework of ref. [59].

The third possibility, feasible and able to test a large interval of cross sections and of WIMP halo densities, is the so-called annual modulation signature [53]. This is the main signature exploited by DAMA/NaI [60, 61, 62, 63, 64, 65, 66, 11]. The annual modulation of the signal rate is induced by the Earth revolution around the Sun; as a consequence, the Earth is crossed by a larger WIMP flux in June (when its rotational velocity is summed to the one of the solar system with respect to the Galaxy) and by a smaller one in December (when the two velocities are subtracted) (see Fig.6).

In particular, the expected differential rate as a function of the recoil energy,

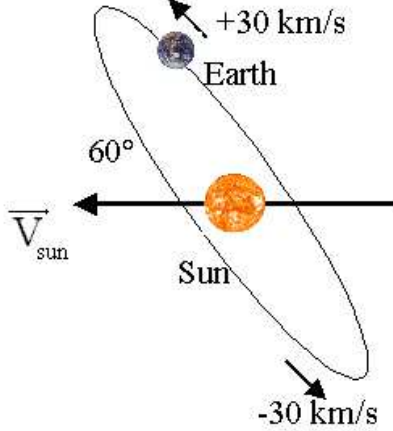


Figure 6: Schematic view of the Earth motion around the Sun.

dR/dE_R (see §7.1 for detailed discussion), depends on the WIMP velocity distribution and on the Earth's velocity in the galactic frame, $\vec{v}_e(t)$. Projecting $\vec{v}_e(t)$ on the galactic plane, one can write:

$$v_e(t) = v_\odot + v_\oplus \cos \gamma \cos \omega(t - t_0) \quad (1)$$

here v_\odot is the Sun's velocity with respect to the galactic halo ($v_\odot \simeq v_0 + 12$ km/s and v_0 is the local velocity whose value is in the range 170-270 km/s [62, 67]); $v_\oplus = 30$ km/s is the Earth's orbital velocity around the Sun on a plane with inclination $\gamma = 60^\circ$ respect to the galactic plane; furthermore, $\omega = 2\pi/T$ with $T=1$ year and roughly $t_0 \simeq 2^{nd}$ June (when the Earth's speed is at maximum). The Earth's velocity can be conveniently expressed in unit of v_0 : $\eta(t) = v_e(t)/v_0 = \eta_0 + \Delta\eta \cos \omega(t - t_0)$, where – depending on the assumed value of the local velocity – $\eta_0 = 1.04-1.07$ is the yearly average of η and $\Delta\eta = 0.05-0.09$. Since $\Delta\eta \ll \eta_0$, the expected counting rate can be expressed by the first order Taylor approximation:

$$\frac{dR}{dE_R}[\eta(t)] = \frac{dR}{dE_R}[\eta_0] + \frac{\partial}{\partial \eta} \left(\frac{dR}{dE_R} \right)_{\eta=\eta_0} \Delta\eta \cos \omega(t - t_0). \quad (2)$$

Averaging this expression in a k -th energy interval one obtains:

$$S_k[\eta(t)] = S_k[\eta_0] + \left[\frac{\partial S_k}{\partial \eta} \right]_{\eta=\eta_0} \Delta\eta \cos \omega(t - t_0) = S_{0,k} + S_{m,k} \cos \omega(t - t_0), \quad (3)$$

with the contribution from the highest order terms less than 0.1%. The first time-independent term is:

$$S_{0,k} = \frac{1}{\Delta E_k} \int_{\Delta E_k} \frac{dR}{dE_R}[\eta_0] dE_R, \quad (4)$$

while the second term is the modulation amplitude given by:

$$S_{m,k} = \frac{1}{\Delta E_k} \int_{\Delta E_k} \frac{\partial}{\partial \eta} \left(\frac{dR}{dE_R} \right)_{\eta=\eta_0} \Delta\eta dE_R \simeq \frac{S_k[\eta_{max}] - S_k[\eta_{min}]}{2}, \quad (5)$$

with $\eta_{max} = \eta_0 + \Delta\eta$ and $\eta_{min} = \eta_0 - \Delta\eta$. The $S_{0,k}$ and $S_{m,k}$ are functions of the parameters associated with the WIMP interacting particle (such as e.g. mass and interaction cross sections), of the experimental response of the detector, of the considered model framework and of the related parameters (see later).

It is worth to note that the $S_{m,k}$ values can be not only positive, but also negative or zero, due to the expected energy distribution profiles in June and in December within a finite energy window [68]. Therefore, the highest sensitivity can be obtained when considering the smallest energy bins allowed by the available statistics in the energy region of interest.

Although the modulation effect is expected to be relatively small (the fractional difference between the maximum and the minimum of the rate is of order of $\simeq 7\%$), a suitable large-mass, low-radioactive set-up with an efficient control of the running conditions – such as DAMA/NaI [41] – would point out its presence. In fact, a suitable correlation analysis can allow to extract even a small periodic component, superimposed with a time independent signal and a background [53]. With the present technology, the annual modulation remains the main signature of a WIMP signal.

In addition, the annual modulation signature is very distinctive since a WIMP-induced seasonal effect must simultaneously satisfy all the following requirements: the rate must contain a component modulated according to a cosine function (1) with one year period (2) and a phase that peaks roughly around $\simeq 2^{nd}$ June (3); this modulation must only be found in a well-defined low energy range, where WIMP induced recoils can be present (4); it must apply to those events in which just one detector of many actually "fires", since the WIMP multi-scattering probability is negligible (5); the modulation amplitude in the region of maximal sensitivity must be $\lesssim 7\%$ (6). Only systematic effects able to fulfil these 6 requirements could mimic this signature and – as far as we know – no other effect investigated so far in the field of rare processes offers a so stringent and unambiguous signature.

Of course, the amount of the measured effect depends e.g. on the sensitivity of the experiment to the coupling of the WIMP candidate, on the WIMP particle physics features, on the nuclear features of the used target-nucleus and on the quality of the running conditions.

4 The DAMA experiment

The DAMA experiment has been worked and works as an observatory for rare processes (such as WIMP direct detection, $\beta\beta$ decay processes, charge-non-conserving processes, Pauli exclusion principle violating processes, nucleon instability, solar axions and exotics [18, 22, 24, 34, 35, 41, 46, 47, 59, 60, 61, 62, 63, 64, 65, 66, 68, 69, 70, 71, 72, 11]) by developing and using low radioactive scintillators. It is installed deep underground in the Gran Sasso National Laboratory of I.N.F.N..

The main developed and used experimental set-ups are: the $\simeq 100$ kg NaI(Tl) set-up (DAMA/NaI) [41] (which has completed its data taking in July 2002), the $\simeq 6.5$ kg liquid Xenon set-up (DAMA/LXe) [70], the so-called "R&D" apparatus (DAMA/R&D) and the new LIBRA (Large sodium Iodide Bulk for RARe processes; $\simeq 250$ kg of ultra-radiopure NaI(Tl)) set-up (DAMA/LIBRA) whose installation has

been started in fall 2002 and which is presently in test run. Moreover, an underground low-background germanium detector allows to select materials for radiopurity.

In the following the final model independent result of DAMA/NaI on the investigation of the WIMP annual modulation signature is discussed. We remind that DAMA/NaI is the largest mass, highest sensitivity experiment, built before the new DAMA/LIBRA, having as main aim the investigation of WIMPs in the galactic halo. It was a pioneer experiment proposed in 1990 [73], which has opened for other experiments and approaches in the field; moreover, its results on the investigation of WIMPs in the galactic halo by the annual modulation signature have - by the fact - motivated the wide interest in the field arisen in recent years.

4.1 DAMA/NaI

The DAMA/NaI set-up [41] can effectively exploit the WIMP annual modulation signature because of its well known technology, of its high intrinsic radiopurity, of its mass, of its suitable control of all the operational parameters and of the deep underground experimental site.

The detailed description of the $\simeq 100$ kg NaI(Tl) DAMA set-up, of its radiopurity, of its performance, of the used hardware procedures, of the determination of the experimental quantities and of the data reduction has been given in refs. [41, 63, 64].

Here we only recall that the detectors used in the annual modulation studies are nine 9.70 kg highly radiopure NaI(Tl) scintillators especially built for this purpose in a joint effort with Crismatec company. The bare NaI(Tl) crystals are encapsulated in suitably radiopure Cu housings; 10 cm long Tetrasil-B light guides act as optical windows on the two end faces of the crystals and are coupled to specially developed EMI9265-B53/FL photomultipliers (PMT), which are supplied by positive voltage with ground cathode. The two PMTs of a detector work in coincidence and their threshold is set at the single photoelectron level; the measured light response is 5.5 – 7.5 photoelectrons/keV depending on the detector [41]. The software energy threshold has been cautiously taken at 2 keV [41, 46, 64]. The detectors are inside a low radioactivity sealed copper box installed in the center of a low radioactivity Cu/Pb/Cd-foils/polyethylene/paraffin shield. Moreover, about 1 m concrete (made from the Gran Sasso rock material) almost fully surrounds (outside the barrack) this passive shield, acting as a further neutron moderator. The copper box is maintained in a high purity (HP) Nitrogen atmosphere in slightly overpressure with respect to the external environment. Furthermore, also the whole shield is sealed and maintained in the HP Nitrogen atmosphere. The whole installation is air-conditioned and the temperature is monitored. On the top of the shield a glove-box (also maintained in the HP Nitrogen atmosphere) is directly connected to the inner Cu box, housing the detectors, through Cu pipes. The pipes are filled with low radioactivity Cu bars (covered by 10 cm of low radioactive Cu and 15 cm of low radioactive Pb) which can be removed to allow the insertion of radioactive sources for calibrating the detectors in the same running condition, without any contact with external air [41].

An hardware/software system to monitor the running conditions has been operative; in particular, several probes have been read out by the data acquisition system and stored with the production data. Moreover, self-controlled computer processes are

operational to automatically control several parameters and to manage alarms [41, 64].

The electronic chain and the data acquisition system used during the DAMA/NaI-0 to DAMA/NaI-5 running periods has been described in ref. [41]. At completion of the DAMA/NaI-5 data taking (summer 2000) the whole electronics and DAQ have been completely substituted; they are briefly summarized in the following. This new system has been operative during DAMA/NaI-6 to -7 running periods, that is up to the end of the DAMA/NaI data taking.

The new DAQ system has been based on a Digital Alpha Workstation with Digital Unix operating system interfaced with the VXI and CAMAC components of the electronic chain via a GPIB bus; the acquisition program has been developed on the basis on the system discussed in ref. [74] and on a specific applicative software. In the new configuration the HV power supply for the PMTs has been given by a CAEN multichannel voltage supply with voltage stability of 0.1%.

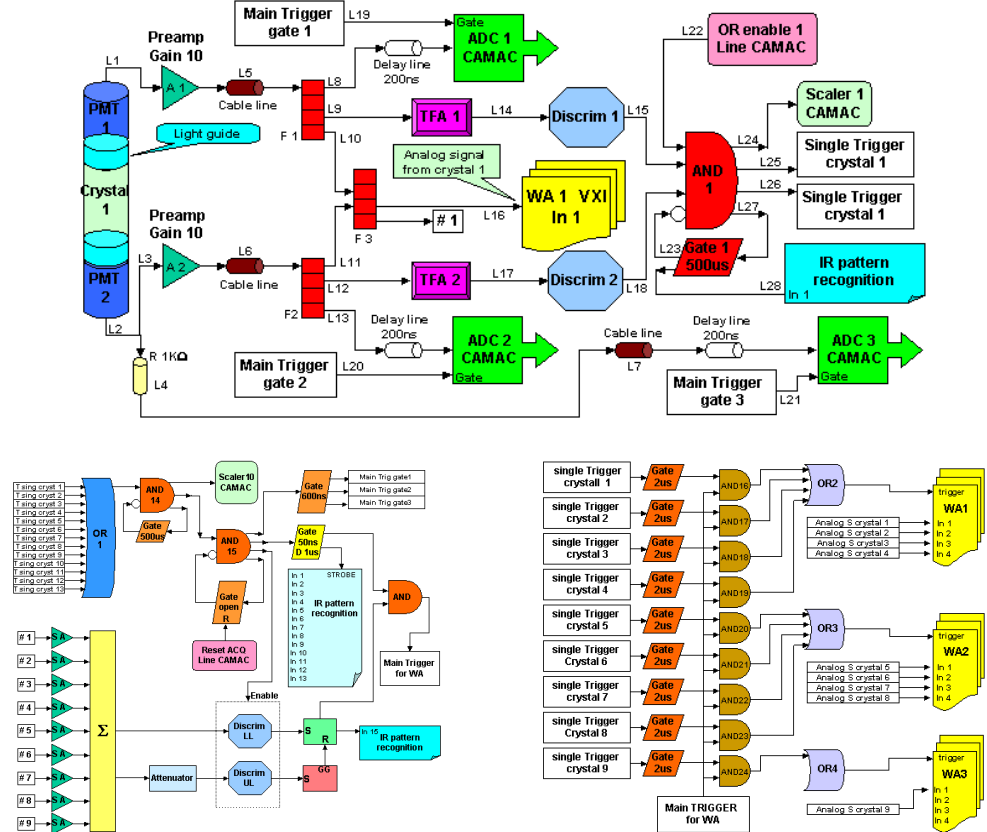


Figure 7: The new electronic chain installed after the completion of the DAMA/NaI-5 running period. Top: schema of the electronic chain of a single detector with its trigger in the new electronic chain. Bottom left: schema of the main trigger of the new acquisition system. Bottom right: schema of the trigger of the new Waveform Analyzers (WA).

In Fig. 7 the analogic part of this new electronic chain for one detector and its trigger are shown as well as the main trigger of the acquisition system and the trigger system of the new waveform analyzer. We note that the analogic part and the trigger for single detector are similar to the ones in the previous electronic chain, but the multiplexer system – which was used in the past (having there at disposal only one single channel Transient Digitizer LeCroy 8828D with 200 MSample/s sampling frequency) – has been removed since now each detector has a devoted waveform analyzer (*WA*) channel. This is accomplished using fast VXI Tektronix four-channel TSV641A digitizers with a sampling frequency of 1 GSsample/s and 250 MHz bandwidth. The digitizers provide a VXI word-serial protocol for commands, while a specific Fast Data Channel (FDC) driver developed by [75] has been used to speed up the data transfer through the GPIB bus. The main trigger part of the electronic schema and the high energy data acquisition are also similar to the ones in the previously used electronic chain [41].

For completeness and for template purpose, let us briefly describe this new electronic chain. The signal $L1$ (see Fig. 7 for the definition of the symbols) from the first PMT is sent to the $A1$ preamplifier having 0-250 MHz bandwidth, a factor 10 gain and a voltage integral linearity $\pm 0.2\%$. The signal $L2$ from the second PMT is divided in two branches: 19/20 of the signal is sent to the input of the $A2$ preamplifier, while the remaining 1/20 – suitably delayed – feeds a charge ADC ($ADC3$) channel. This last part processes the pulses with amplitude such to saturate the remaining part of the electronics (they correspond to high energy events). The preamplified signals – through linear Fan-in/Fan-out devices – provide the inputs for the charge ADCs (left signals and right signals) and for the VXI waveform analyzer ($WA1$ in Fig. 7) (which processes the signal in a $2\ \mu s$ time window)⁴.

The electronic devices, that provide the trigger of a single detector, are shown in Fig. 7. In particular, the copies of the PMT signals are the inputs of the Timing Filter Amplifiers ($TFA1$ and $TFA2$) which amplify and integrate the signal (integration time 50 ns); their outputs are discriminated ($Discrim1$ and $Discrim2$) with single photoelectron trigger level. The coincidence ($AND1$) between the two logical NIM outputs provides the *single* trigger of the detector. The other inputs of $AND1$ are: the signal $L23$ given by a Gate Generator ($GG1$) which allows to reject afterglow and Bi-Po events in a $500\mu s$ time window after the occurrence of the event (introducing a systematic error on the measured rate of about 10^{-4}) and the signal $L22$ given by a CAMAC I/O Register. The latter permits to enable or disable the *single* detector trigger during the calibrations. The outputs of $AND1$ provide: i) the signal for a CAMAC scaler ($Scaler1$) to count the events for each detector; ii) the $L25$ and $L26$ used in the main trigger (see later); iii) $L27$ giving the start to the Gate Generator ($GG1$) which – in addition to the veto of the coincidence – gives the signal $L28$ issued to a 16-bit CAMAC I/R Pattern Recognition which allows to identify the detector or the detectors which have generated the trigger.

The general trigger of the acquisition – see Fig. 7 – is provided by the logic $OR1$ of all the crystals. The output of $AND14$ is issued to a Scaler, which counts the number

⁴For completeness we note that the 4 detectors named SIMP in ref. [41] which have been used only as additional anticoincidence and – sometimes – in special triggers, have not been equipped in the new electronic chain with waveform analyzers.

of main triggers sent to the coincidence *AND15*. The coincidence *AND15* generates triggers only when the acquisition is ready to manage them. Therefore, the dead time of the acquisition is properly accounted in the estimate of the running time by using the information from the scaler after *AND14*. When a general trigger occurs, the following logic signals are issued to: i) the Gate Generator (*GG2*) generating the 600 ns gates the charge ADCs; ii) the Delay Gate Generator which gives the strobe signal to the I/R Pattern Recognition and generates the LAM (and, therefore, the interrupt to the CPU of the acquisition computer) in the CAMAC system; iii) the Delay Gate Generator which gives the signal to the trigger of the waveform analyzers. This last condition is verified only if the total energy deposited in the detectors is in an energy window suitably chosen (1 to 90 keV). For this purpose, each line feeds a Spectroscopy Amplifier whose gain is equalized in order to have the same response for each detector. Therefore, a Single Channel Analyzer made by the two discriminators, *Discrim LL* and *Discrim UL*, allows to select only events in the chosen energy window.

A devoted electronic circuit [76], shown in Fig. 7, allows to trigger only the *WA*'s which correspond to fired detectors; it gives a trigger to each *WA* when: i) at least one of its corresponding lines has a trigger; ii) the *main trigger* is present; iii) the total energy of the events is in the chosen energy window. Let us remind that for the events with energy outside this energy window (e.g. high energy events) the ADC values are acquired in any case.

As regards other aspects, we recall that the linearity and the energy resolution of the detectors have been investigated using several sources [41, 64] such as, for the low energy region, ^{55}Fe (5.9 keV X-rays), ^{109}Cd (22 keV X-rays and 88 keV γ line) and ^{241}Am (59.5 keV γ line) sources. In particular, in the production runs, the knowledge of the energy scale is assured by periodical calibrations with ^{241}Am source and by monitoring (in the production data themselves summed every $\simeq 7$ days) the position and energy resolution of the 46.5 keV γ line of the ^{210}Pb [41, 46, 60, 61, 63, 64]. The latter peak is present – at level of few counts per day per kg (cpd/kg) – in the measured energy distributions mainly because of a contamination (by environmental Radon) of the external surface of the crystals' Cu housings, occurred during the first period of the underground storage of the detectors. The calibration sources are introduced in the proximity of the detectors by means of the pipes connected – as already described – with the upper "glove-box", which is also continuously maintained in the HP Nitrogen atmosphere.

As in every experiment in the field, obvious noise events (whose number sharply decreases when increasing the number of available photoelectrons) have to be removed; the used procedure has been described e.g. in refs. [41, 64]⁵. We remind that the noise in this experiment is given by PMT fast single photoelectrons with decay times of the order of tens ns, while the "physical" (scintillation) pulses have decay times of order of hundreds ns. Thus, the large difference in decay times and the relatively large number of available photoelectrons response assure an effective noise rejection

⁵This procedure assures also the rejection of any possible contribution either from afterglows (when not already excluded by the dedicated 500 μs veto time; see above) induced by high energy events or from any possible Čerenkov pulse in the light guide or in the PMTs; in fact, they also have time decay of order of tens ns as the noise events.

[41, 63, 64]. Several variables can be built by using the pulse information recorded by the waveform analyzer [41, 64]). In particular, for each energy bin, we plot the $Y = \frac{\text{Area}(\text{from } 0 \text{ ns to } 50 \text{ ns})}{\text{Area}(\text{from } 0 \text{ ns to } 100 \text{ ns})}$ value versus the $X = \frac{\text{Area}(\text{from } 100 \text{ ns to } 600 \text{ ns})}{\text{Area}(\text{from } 0 \text{ ns to } 600 \text{ ns})}$ value calculated for every event. In the X, Y plane the slow scintillation pulses are grouped roughly around ($X \simeq 0.7$, $Y \simeq 0.5$) well separated from the noise population which is grouped around small X and high Y values (see e.g. ref. [41]). The scintillation pulses are selected by applying an acceptance window in X, Y . Since the statistical spread of the two populations in the X, Y plane becomes larger when the number of available photoelectrons and the signal/noise ratio decrease, windows with smaller acceptance become necessary to maintain the same noise rejection power. In the DAMA/NaI experiment they are kept enough stringent to assure also the absence of any possible residual noise tail in the scintillation data to be analysed [41]. According to standard procedures, the acceptance of the considered window for scintillation pulses in the X, Y plane is determined by applying the same procedure to the scintillation data induced – in the same energy intervals – by calibration sources [41, 63, 64]. In particular, for this purpose, about 10^4 - 10^5 events per keV are typically collected in the low energy region just above the 2 keV software energy threshold during routine calibration runs [41, 64]. All the periodical long calibration procedures [41, 46] and the time specifically allocated for maintenance and/or for improvements are the main components affecting the duty cycle of the experiment. Moreover, in the DAMA/NaI-1 running period the data have been taken only in the two extreme conditions for the annual modulation signature (see Table 1).

The energy threshold, the PMT gain, the electronic line stability are continuously verified and monitored during the data taking by the routine calibrations, by the position and energy resolution of the ^{210}Pb line (see above) and by the study of the hardware rate behaviours with time.

In particular, the measured low energy distributions of interest for the WIMP investigation have been given in refs. [59, 63, 64, 71], where the corrections for efficiencies and acquisition dead time have already been applied. We note that usually in DAMA/NaI the low energy distributions refer to those events where only one detector of many actually fires (that is, each detector has all the others in the same installation as veto; this assures a background reduction, which is of course impossible when a single detector is used).

5 The first DAMA/NaI results on the annual modulation signature

The presence of a model independent effect has been firstly pointed out since the TAUP conference in 1997 [77] and corollary model dependent quests for a candidate particle have been analysed in some of the many possible model frameworks, improving the quest with time (see Table 1). Cumulatively during four annual cycles a model independent effect (exposures up to 57986 kg · day; see Table 1) has been pointed out [63, 64]. No systematics or side reactions able to mimic the annual modulation signature has been found [64]; this can be well understood when considering the particularly stringent and numerous specific requirements which identify the WIMP annual

modulation signature itself (see §3.3). No other experiment has at present suitable

Table 1: Summary of the first running periods which have already cumulatively shown a 4σ C.L. model independent effect. The related references are given in the third column. In the last column the improvements with time in the model-dependent quest for the candidate are summarized.

Periods	Statistics (kg \times day)	Ref.	Considered scenarios in corollary quests for the candidate (prior on mw from accelerator expts included)
DAMA/NaI-1	3363.8 (winter) + 1185.2 (summer)	[60]	WIMP pure SI, Isothermal spherical halo, $v_0 = 220$ km/s, Helm Form Factor, All the parameters fixed to their central value
DAMA/NaI-2	14962 (Nov. \rightarrow end of July)	[61], [62]	as DAMA/NaI-1 + halo (co-)rotation + uncertainty on v_0
DAMA/NaI-3	22455 (middle Aug. \rightarrow end of Sept.)	[63]	as DAMA/NaI-2 + prior from DAMA/NaI-0
DAMA/NaI-4	16020 (middle Oct. \rightarrow middle Aug.)	[63]	as DAMA/NaI-3
TOTAL	57986	[63], [64], [65], [66], [11]	as DAMA/NaI-3 and DAMA/NaI-4 + SI&SD, “inelastic” + Other consistent halo models, SD form factor from [117] Uncertainties on some parameters
+ DAMA/NaI-0	4123.2	[46]	Limits on recoils measured by pulse shape discrimination

sensitivity, mass and control of the running conditions to effectively exploit the WIMP annual modulation signature as DAMA/NaI.

As mentioned, the implications of the observed model independent effect have been in addition studied also under some – of the many possible – different model–dependent frameworks. In fact, some scenarios for purely spin-independent (SI), purely spin-dependent (SD)⁶, mixed SI and SD coupled WIMPs and also WIMPs with *preferred inelastic* scattering [60, 61, 62, 63, 64, 65, 66, 11] have been considered, including in the data analyses the lower bound on the mass of the supersymmetric candidate as derived from the LEP data in the usually adopted supersymmetric schemes based on GUT assumptions as e.g. in ref. [78]. This corollary investigation on the quest for a candidate particle has been improved with time in several aspects as summarized in Table 1. Theoretical implications of these results in terms of a neutralino with dominant SI interaction have been discussed e.g. in ref. [79, 80] for some theoretical model frameworks and in terms of an heavy neutrino of the fourth family in ref. [26].

⁶For the sake of completeness, we comment that JHEP 0107 (2001) 044 is not at all in conflict with a possible SD solution since it considered only two particular purely SD couplings (of the many possible) in a strongly model dependent context and using modulation amplitudes valid instead only in a particular purely SI case.

5.1 Comparison with some model dependent results

5.1.1 ... from direct searches

As mentioned above no other experiment directly comparable with the model independent DAMA/NaI result on WIMPs in the galactic halo is available at present.

Only few experiments [48, 49, 81], which use different target nuclei and different methodological approaches, have released extremely poor statistics following the so-called model dependent "traditional" approach (see section 3.2). We have reported several times (see e.g. ref. [82]) some specific arguments; here we only summarize in Table 2 some main items.

In particular, these experiments exploit a huge data selection releasing typically extremely poor exposures with respect to generally long data taking and, in some cases, to several used detectors. Their counting rate is very high and few/zero events are claimed after applying several strong and hardly safe rejection procedures (involving several orders of magnitude; see Table 2). These rejection procedures are also poorly described and, often, not completely quantified. Moreover, most efficiencies and physical quantities entering in the interpretation of the claimed selected events (see Table 2) have never been discussed in the needed details; as an example, we mention the case of the quenching factor of the recoil target nuclei in the whole bulk material for the bolometer cases, which is arbitrarily assumed to be 1 (see §7.1.6), implying a substantially arbitrarily assumed energy scale and energy threshold. The reproducibility of the results over different running periods has also not been proved as well as the values of the effective sensitive volumes for read-outs of the two signals (when applied) and the overall efficiencies. Further uncertainties are present when, as in ref. [48], a neutron background modeling and subtraction is pursued in addition.

As regards in particular the Zeplin-I result of ref. [81, 83], a very low energy threshold is claimed (2 keV), although the light response is very poor: between $\simeq 1$ ph.e./keV [81] (for most of the time) and $\simeq 2.5$ ph.e./keV (claimed for 16 days) [83]⁷. Moreover, a strong data filtering is applied to the high level of measured counting rate ($\simeq 100$ cpd/kg/keV at low energy, which is nearly two orders of magnitude larger than the DAMA NaI(Tl) background in the same energy region) by hardware vetoes, by fiducial volume cuts and, largely, by applying down to few keV a standard pulse shape discrimination procedure, although the LXe scintillation pulse profiles (pulse decay time < 30 ns) are quite similar even to noise events in the lower energy bins and in spite of the poor light response. Quantitative information on experimental quantities related to the used procedures has not yet been given [81, 83].

In addition to the experimental aspects, these experiments generally perform an uncorrect quotation of the DAMA/NaI first quests for a purely SI coupled candidate in some given model frameworks and ignore the published interpretation of the DAMA/NaI model independent effect in terms of candidates with other kind of couplings. Anyhow, intrinsically no reliable result can be achieved in a comparison of the exclusion plots quoted by these experiments with regions allowed by DAMA/NaI in corollary quests for a candidate. In fact, any exclusion plot always refers to a partic-

⁷For comparison we remind that the data of the DAMA/LXe set-up, which has a similar light response, are analysed by using the much more realistic and safer software energy threshold of 13 keV [47].

Table 2: Features of the first DAMA/NaI results on the WIMP annual modulation signature ($57986 \text{ kg} \times \text{day}$ exposure) [60, 61, 62, 63, 64, 65, 66, 11] with those of refs. [48, 49, 81]. See text. Here (as well as in the text) keV always means keV electron equivalent if not otherwise mentioned.

	DAMA/NaI	CDMS-I	Edelweiss-I	Zeplin-I
Signature	annual modulation	None	None	None
Target-nuclei	$^{23}\text{Na}, {}^{127}\text{I}$	${}^{nat}\text{Ge}$	${}^{nat}\text{Ge}$	${}^{nat}\text{Xe}$
Technique	well known	poorly experienced	poorly experienced	critical optical liquid/gas interface in this realization
Target mass	$\simeq 100 \text{ kg}$	0.5 kg	0.32 kg	$\simeq 3 \text{ kg}$
Exposure	$57986 \text{ kg} \times \text{day}$	$15.8 \text{ kg} \times \text{day}$	$8.2 \text{ kg} \times \text{day}$	$280 \text{ kg} \times \text{day}$
Depth of the experimental site	1400 m	10 m	1700 m	1100 m
Software energy threshold	2 keV (5.5 – 7.5 p.e./keV)	10 keV	20 keV	2 keV (but: $\sigma/E = 100\%$ mostly 1 p.e./keV; [81]) (2.5 p.e./keV for 16 days; [83])
Quenching factor	Measured	Assumed = 1	Assumed = 1	Measured
Measured event rate in low energy range	$\simeq 1 \text{ cpd/kg/keV}$	$\simeq 60 \text{ cpd/kg/keV}$ (10^5 events)	2500 events total	$\simeq 100 \text{ cpd/kg/keV}$
Claimed events after rejection procedures		23 in Ge, 4 in Si, 4 multiple evts in Ge + MonteCarlo on neutron flux	0	$\simeq 20\text{-}50 \text{ cpd/kg/keV}$ after rejection and ?? after standard PSD [81, 83]
Events satisfying the signature in DAMA/NaI	modulation amplitude integrated over the given exposure $\simeq 2000$ events			
Expected number of events from DAMA/NaI effect		from few down to zero depending on the models (and on quenching factor)	from few down to zero depending on the models (and on quenching factor)	depends on the models (even zero)

ular model framework where, in addition, all the involved nuclear cross sections are scaled to cross section(s) on nucleon (see §7.1); thus, it has no "universal" validity and – even within the same general assumptions for a model (e.g. purely SI coupling) – the proper accounting for parameters uncertainties, scaling laws uncertainties, form factors uncertainties, halo model uncertainties, etc. (see §7.1.3) significantly vary the

result of any comparison (even when assuming as correct the evaluation of the selected number of events and the energy scale and energy threshold determinations given in refs. [48, 49, 81, 83]). Moreover, there exist scenarios (see e.g. later in §7.1.3) to which Na and I are sensitive and other nuclei, such as e.g. ^{nat}Ge , ^{nat}Si and ^{nat}Xe , are not. Just as an example, a possible WIMP with a SI cross section of few 10^{-7} pb and with SD cross section of few 10^{-1} pb would produce a sizeable signal in DAMA/NaI, but almost nothing in the Ge and Si experiments of refs. [48, 49] as well as in the Xenon target of ref. [81, 83] if the SD component would have $\theta \simeq 0$ or $\theta \simeq \pi$ (see §7.1.1).

In conclusion:

1. no other experiment, whose result can be directly comparable in a model independent way with that of DAMA/NaI, is available so far.
2. as regards in particular CDMS-I, EDELWEISS-I and Zeplin-I, e.g.:
 - i) they are insensitive to the model independent WIMP annual modulation signature exploited by DAMA/NaI; ii) they use different methodological approaches, which do not allow any model independent comparison and they have different sensitivities to WIMPs; in particular, the number of counts they could expect on the basis of the model independent DAMA/NaI result varies from few to zero events depending on the models, on the assumptions and on the theoretical/experimental parameters' values adopted in the calculations; iii) they do not make neither correct nor complete comparisons with the DAMA/NaI experimental result; iv) they use extremely poor statistics; v) they reduce their huge measured counting rate of orders of magnitude by various rejection procedures claiming for very optimistic rejection powers; vi) their energy scale determination and/or energy threshold appear questionable (in the first two cases because of the quenching factors values and in the second because of the poor number of photoelectrons/keV); etc.

Finally, in addition, these experiments ⁸ intrinsically could never reliably claim for a signal because of the used approach, as mentioned in §3.2.1.

5.1.2 ... from indirect searches

It has been suggested that Dark Matter particles could loose their velocity down to a value lower than the escape velocity of a celestial body (Earth, Sun) scattering off nuclei and, therefore, remaining trapped in its gravitational field. Subsequently, via their annihilation in the celestial bodies or in the Galactic halo they could give rise to high energy neutrinos, positrons, antiprotons and gamma's. In principle, the Sun could capture WIMPs more effectively than the Earth because of the higher escape velocity, but the smaller distance detector – center of the Earth and the "resonant" scattering on the heavy nuclei in the Earth (mostly on iron) could compensate this effect.

A possible signature of WIMP annihilation in celestial bodies is given by the produced ν_μ , whose interactions in the rock below a detector would give rise to "upgoing"

⁸Recent updates of some results, appeared during the publication of this paper, leave the arguments discussed in this section unchanced in the essence.

muons in the detector itself. The expected μ flux depends on the WIMP annihilation rate in the celestial body and on the neutrino energy spectrum produced in the annihilations. However, several sources of uncertainties are present in similar estimates (and, therefore, in the obtained results) such as for example the assumption that a "steady state" has been reached in the considered celestial body and the significant uncertainty which arises from the estimate and subtraction of the existing competing process offered by the atmospheric neutrinos.

Anyhow, when a model and the related parameters' values are assumed, it is possible to estimate the differential flux expected for the secondary neutrinos. According to ref. [84] (where the neutralino in the MSSM model has been considered), this flux can be written as

$$\frac{dN_\nu}{dE_\nu} = \frac{\Gamma_A}{4\pi d^2} \sum_{F,f} B_{\chi f}^{(F)} \frac{dN_{f\nu}}{dE_\nu}, \quad (6)$$

where Γ_A is the annihilation rate, d is the distance between the detector and the source (e.g. the Earth center or the Sun center), F is the final state of the annihilation process, $B_{\chi f}^{(F)}$ are the branching ratios of the heavy quarks decays; the $dN_{f\nu}/dE_\nu$ term represents the differential distribution of neutrinos produced by τ and by the quarks and gluons hadronization and of the subsequent semileptonic decays of the produced hadrons.

Considering, in particular, the ν_μ and $\bar{\nu}_\mu$, an estimate of the produced neutrino flux can be obtained by measuring the up-going muons given by the ν_μ and $\bar{\nu}_\mu$ interactions with the rock below the detector. Their energy distribution can be written as:

$$\frac{dN_\mu}{dE_\mu} = N_A \int_{E_\mu^{th}}^{\infty} dE_\nu \int_0^{\infty} dX \int_{E_\mu}^{E_\nu} dE'_\nu P_{surv}(E_\mu, E'_\mu; X) \frac{d\sigma(E_\mu, E'_\mu)}{dE'_\mu} \frac{dN_\nu}{dE_\nu}, \quad (7)$$

where X is the muon range in the rock, $d\sigma(E_\mu, E'_\mu)/dE'_\mu$ is the charge current cross section for muon production of energy E'_μ from a neutrino of energy E_ν and $P_{surv}(E_\mu, E'_\mu; X)$ is the survival probability of a muon with E'_μ initial energy and E_μ final energy after crossing a thickness X of rock; E_μ^{th} is, finally, the energy threshold of the detector. The function $P_{surv}(E_\mu, E'_\mu; X)$ obviously account for the muon energy loss in the rock.

As mentioned, the up-going muons produced by atmospheric neutrinos are side reactions for the process searched for, however – in principle – they are expected to have a flat angular distribution while those induced by WIMPs have a preferred impinging direction (e.g. the Sun–laboratory direction or Earth center–laboratory direction).

Model dependent analyses with a similar approach have been carried out by large experiments deep underground such as e.g. MACRO and Superkamiokande. It is worth to remark that no quantitative comparison can be directly performed between the results obtained in direct and indirect searches because it strongly depends on the assumptions and on the considered model frameworks. In particular, a comparison would always require the calculation and the consideration of all the possible WIMP configurations in the given particle model (e.g. for χ : in the allowed parameters space), since it does not exist a biunivocal correspondence between the observables in the two

kinds of experiments: WIMP-nucleus elastic scattering cross section (direct detection case) and flux of muons from neutrinos (indirect detection case). In fact, the counting rate in direct search depends on the spin-dependent (SD) and on the spin-independent (SI) cross sections of the elastic processes, while the muon flux is connected not only to them, but also to the WIMP annihilation cross section. In principle, the three cross sections can be correlated, but only when a specific model is adopted and by non directly proportional relations. As an example, we report in Fig. 8 the scatter plot

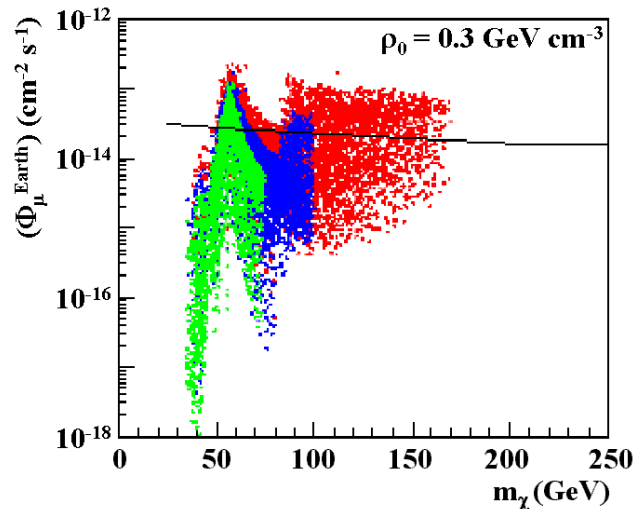


Figure 8: Scatter plot for the up-going muon flux from the center of the Earth vs neutralino mass. The configurations (MSSM) – here the model dependent constraints from the LEP data of 2000 have been used – have been selected by the DAMA annual modulation region obtained for the model framework considered in ref. [63]. For details see [79]. The solid line is the model dependent upper bound derived from MACRO experiment; the one from Superkamiokande is only marginally more stringent.

for the up-going muon flux from the center of the Earth for a standard Maxwellian distribution versus χ mass in MSSM [79]; here the configurations have been selected by the DAMA annual modulation region for the particular purely SI model framework considered in ref. [63]. As it is evident, the up-going muon flux spans several orders of magnitude although the cross section of the DAMA region, allowed in the model framework considered there, spans almost one. The solid line in this figure is the model dependent upper bound derived from MACRO experiment[85]; the one from Superkamiokande is only marginally more stringent, thus it is still compatible with the DAMA result even when – as in the quoted ref. [63] – the uncertainties on several assumptions and parameters are not yet included (see e.g. [11]).

As we mentioned at the beginning, the annihilation of the Dark Matter particles in the halo could also produce antimatter particles and gamma's. The antimatter searches have to be carried out outside the atmosphere, i.e. on balloons or satellites. In particular, the WIMP annihilation would result in an excess of antiprotons or of positrons up to the WIMP mass with respect to the background arising from other

possible sources. Again the estimate and subtraction of such a background together with the influence of the Earth and of the galactic magnetic field on these particles plays a crucial role on the possibility of a reliable extraction of a signal. However, at present some interesting results have been reported in the analysis of the HEAT balloon-borne experiment and in some others, as reported in Fig. 9a) and b). In fact, an excess of positrons with energy $\simeq 5 - 20$ GeV has been found; it – interpreted in terms of WIMP annihilation [87] – gives a result not in conflict with the effect observed

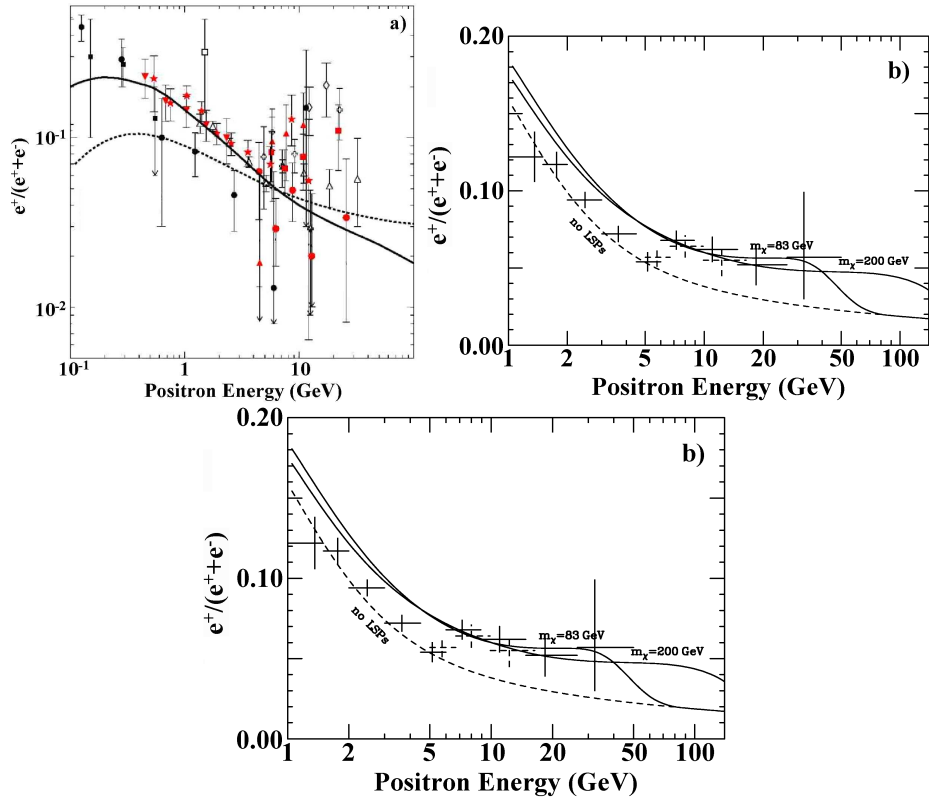


Figure 9: Experimental results and theoretical predictions for the indirect searches: a) Positron fraction measured by several experiments (Caprice98, AMS, Caprice94, HEAT, Clem et al., TS93, MASS89, Golden et al., Muller and Tang, Fanselow et al.; see ref. [86] for details). The two lines are two models of background from secondary production; an excess of positrons over the background modelling is present in both cases. b) Positron fraction measured by HEAT in the interpretation of ref. [87], where the excess of positrons with respect to the background modelling is explained in terms of neutralino annihilation in the galactic halo. c) Gamma ray energy spectrum of the inner Galaxy as measured by EGRET compared with the background modelling (lower line). The large excess of gamma's is explained in ref. [88] by a neutralino annihilation in the galactic halo (the upper curve is the total contribution). These preliminary indications are not in conflict with the DAMA/NaI model independent results previously published.

by DAMA/NaI. Further results can be expected in future by experiments operating in space [89].

As regards the possibility to detect γ 's from WIMP annihilation in the galactic halo, experiments in space are planned. However, at present it is difficult to estimate their possibilities considering e.g. the background level, the uncertainties in its reliable estimate and subtraction as well as the smallness of the expected signal (even more, if a subdominant component would be present) when properly calculated with rescaling procedure. However, we mention the analysis of ref. [90] which already suggests the presence of a γ excess from the center of the Galaxy in the EGRET data [91] as reported in Fig. 9c). This excess match with a possible WIMP annihilation in the galactic halo [90] and is not in conflict with the DAMA/NaI model independent result previously published. Other activities are in preparation and will further clarify the situation [92].

We stress, however, that the specific parameters of a WIMP candidate (mass and cross sections), which can be derived from the indirect searches, critically depend on several assumptions used in the calculations such as the estimation of the background, the halo model, the amount of WIMP in the galactic dark halo, the annihilation channels, the transport of charged particle to the Earth, etc.; thus, they have the same relative meaning as those obtained in the quest for a candidate in direct search approach as described later.

5.2 Conclusions

In conclusion, no model independent comparison with the DAMA/NaI effect is available. Only few model dependent approaches have been used in the direct search approach to claim for a particular model dependent comparison, which appears in addition – as discussed above – neither based on solid procedures nor fully correct nor complete. On the other hand, the indirect search approaches, which also can offer only model dependent comparisons, are either not in contradiction or in substantial agreement with the DAMA/NaI observed effect.

Thus, the interest in the further available DAMA/NaI data is increased; the model independent result on the WIMP annual modulation signature from the data of seven annual cycles as well as some (of the many possible) model dependent quests for a candidate are discussed in the following, reviewing as well the general aspects related to the WIMP direct detection.

6 The DAMA/NaI model independent result on the WIMP annual modulation signature from the data of seven annual cycles

As mentioned, the main goal of the DAMA/NaI experiment is the investigation on a WIMP component in the galactic halo by exploiting the WIMP annual modulation signature introduced in §3.3. The experiment has collected data during seven annual cycles.

The data of each annual cycle have been taken in the same experimental conditions; in particular, the Copper box housing the detectors has always been closed and sealed

and the detectors have always been in contact only with an atmosphere of HP Nitrogen [41, 64]. Moreover, the data taking of each annual cycle has been started before the expected minimum of the signal rate (which is roughly around $\simeq 2^{nd}$ December) and concluded after the expected maximum (which is roughly around $\simeq 2^{nd}$ June).

As mentioned, several operational parameters have been regularly acquired with the production data, such as the operating temperature, the HP Nitrogen flux into the inner Cu box housing the detectors, the pressure of the HP Nitrogen atmosphere in the inner Cu box, the environmental Radon from which however the detectors are excluded (see above and later) and the hardware rate (including the noise) above single photoelectron threshold. Computer controlled processes immediately inform the operator during production runs in case one of the parameters goes outside the stringent allowed interval of stability values. In addition, the recorded parameters values allow a deep analysis and control of possible systematics as performed e.g. in ref. [64] and discussed in the following.

6.1 The evidence

A model independent investigation of the annual modulation signature has been realized by exploiting the time behaviour of the residual rates of the single hit events in the lowest energy regions over the seven annual cycles (total exposure: $107731 \text{ kg} \cdot \text{day}$), as previously performed in refs. [63, 64]. These residual rates are calculated from the measured event rate after subtracting the constant part (the weighted mean of the residuals must obviously be zero over each period): $\langle r_{ijk} - flat_{jk} \rangle_{jk}$. There r_{ijk} is the rate in the considered i -th time interval for the j -th detector in the k -th considered energy bin, while $flat_{jk}$ is the rate of the j -th detector in the k -th energy bin averaged over the cycles. The average is made on all the detectors (j index) and on all the energy bins in the considered energy interval.

This model independent approach on the data of the seven annual cycles offers an immediate evidence of the presence of an annual modulation of the rate of the single hit events in the lowest energy region as shown in Fig. 10, where the time behaviours of the (2–4), (2–5) and (2–6) keV single hit residual rates are depicted. They refer to 4549, 14962, 22455, 16020, 15911, 16608, 17226 $\text{kg} \cdot \text{day}$ exposures, respectively for the DAMA/NaI-1 to -7 running periods ⁹.

In fact, the data favour the presence of a modulated cosine-like behaviour ($A \cos \omega(t - t_0)$) at 6.3σ C.L. ¹⁰ and their fit for the (2–6) keV larger statistics energy interval offers modulation amplitude equal to $(0.0200 \pm 0.0032) \text{ cpd/kg/keV}$, $t_0 = (140 \pm 22) \text{ days}$ and $T = \frac{2\pi}{\omega} = (1.00 \pm 0.01) \text{ year}$, all parameters kept free in the fit.

⁹In particular, the DAMA/NaI-5 data have been collected from August 1999 to end of July 2000 (statistics of $15911 \text{ kg} \cdot \text{day}$); then, the DAQ and the electronics have been fully substituted (see §4.1). Afterwards, the DAMA/NaI-6 data have been collected from November 2000 to end of July 2001 (statistics of $16608 \text{ kg} \cdot \text{day}$), while the DAMA/NaI-7 data have been collected from August 2001 to July 2002 (statistics of $17226 \text{ kg} \cdot \text{day}$), when the data taking with this set-up has been concluded.

¹⁰It is worth to note that the confidence level given in ref. [63] was instead referred to the particular model framework considered there in the quest for a candidate. Here the confidence level refers to the model independent effect itself and is calculated on the basis of the residual rate in the (2–6) keV energy interval. Applying the same procedure to the residuals given in ref. [63], one gets 4.6σ C.L. which is in agreement with the presently quoted value once scaling it by the square root of the ratio of the relative exposures.

The fitting function has been derived from eq. (3) integrated over each time bin. The period and phase agree with those expected in the case of a WIMP induced effect ($T = 1$ year and t_0 roughly at $\simeq 152.5$ -th day of the year). The χ^2 test on the (2–6) keV residual rate in Fig. 10 disfavours the hypothesis of unmodulated behaviour giving a probability of $7 \cdot 10^{-4}$ ($\chi^2/d.o.f. = 71/37$). We note that, for simplicity, in Fig. 10 the same time binning already considered in ref. [63, 64] has been used. The result of this approach is similar by choosing other time binnings; moreover, the results given in the following are not dependent on time binning at all.

The residuals given in Fig. 10 have also been fitted, according to the previous

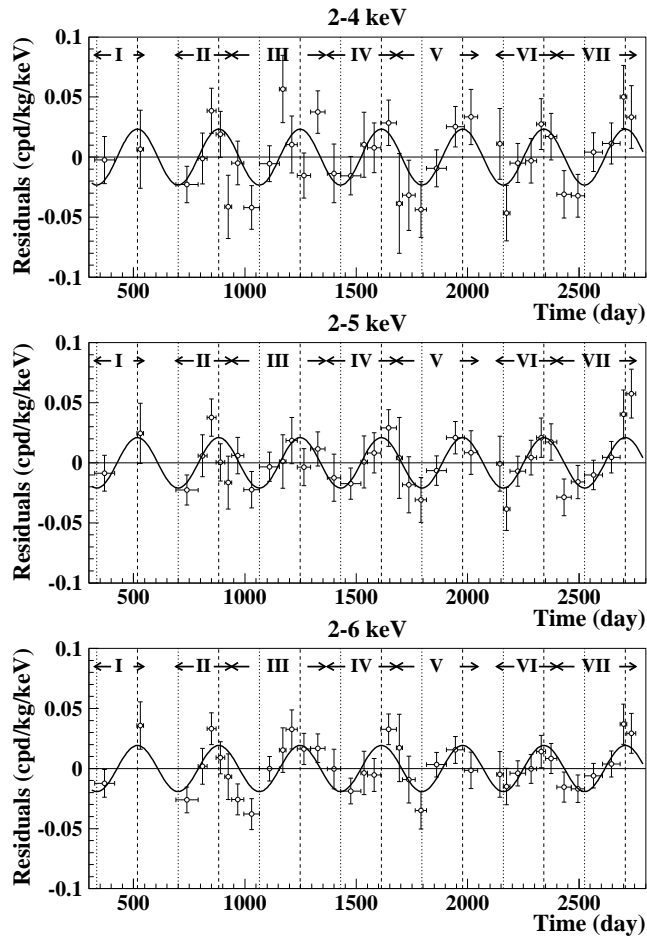


Figure 10: Model independent residual rate for single hit events, in the (2–4), (2–5) and (2–6) keV energy intervals as a function of the time elapsed since January 1-st of the first year of data taking. The experimental points present the errors as vertical bars and the associated time bin width as horizontal bars. The superimposed curves represent the sinusoidal behaviours expected for a WIMP signal with a period equal to 1 year and phase at 2nd June; the modulation amplitudes have been obtained by best fit. See text. The total exposure is $107731 \text{ kg} \cdot \text{day}$.

procedure, fixing the period at 1 year and the phase at 2nd June; the best fitted modulation amplitudes are: (0.0233 ± 0.0047) cpd/kg/keV for the (2–4) keV energy interval, (0.0210 ± 0.0038) cpd/kg/keV for the (2–5) keV energy interval, (0.0192 ± 0.0031) cpd/kg/keV for the (2–6) keV energy interval, respectively.

The same data have also been investigated by a Fourier analysis (performed according to ref. [93] including also the treatment of the experimental errors and of the time binning), obtaining the result shown in Fig. 11, where a clear peak for a period of 1 year is evident.

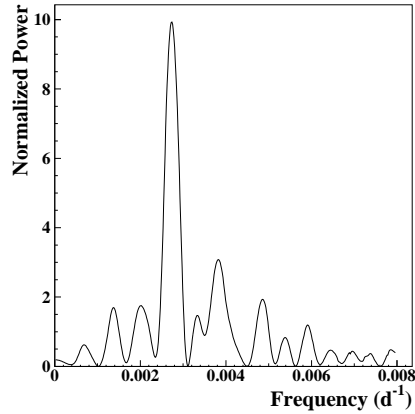


Figure 11: Power spectrum of the measured (2–6) keV single hit residuals calculated according to ref. [93], including also the treatment of the experimental errors and of the time binning. As it can be seen, the principal mode corresponds to a frequency of $2.737 \cdot 10^{-3} \text{ d}^{-1}$, that is to a period of $\simeq 1$ year.

In Fig. 12 the single hit residual rate in a single annual cycle from the total exposure of $107731 \text{ kg} \cdot \text{day}$ is presented for two different energy intervals; as it can be seen the modulation is clearly present in the (2–6) keV energy region, while it is absent just above.

Finally, Fig. 13 shows the distributions of the variable $\frac{S_m - \langle S_m \rangle}{\sigma}$, where S_m are the modulation amplitudes evaluated by a maximum likelihood method [60] for each detector, each annual cycle and each considered energy bin (taken there as an example equal to 0.25 keV) and σ are their errors. The $\langle S_m \rangle$ represent the mean values of the modulation amplitudes over the detectors and the annual cycles for each energy bin. The left panel of Fig. 13 shows the distribution referred to the region of interest for the observed modulation: 2–6 keV, while the right panel includes also the energy region just above: 2–14 keV. These distributions allow one to conclude that the individual S_m values follow a normal distribution, since the variable $\frac{S_m - \langle S_m \rangle}{\sigma}$ is distributed as a gaussian with an unitary standard deviation. In particular, this demonstrates that the modulation amplitudes are statistically well distributed in all the crystals, in all the data taking periods and considered energy bins.

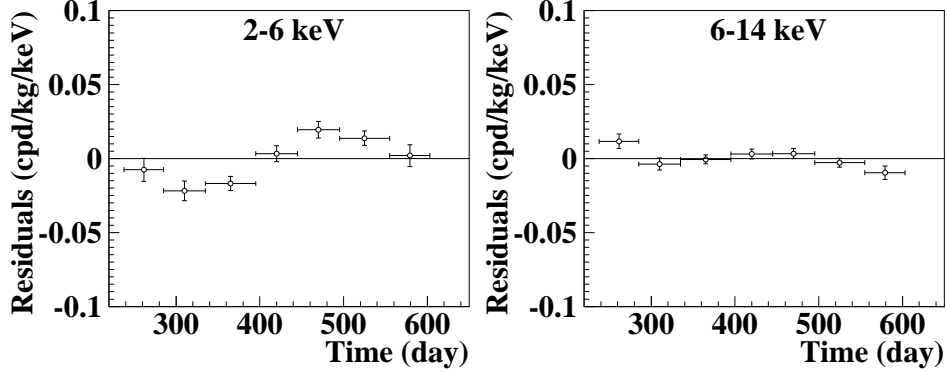


Figure 12: Single hit residual rate in a single annual cycle from the total exposure of $107731 \text{ kg} \cdot \text{day}$. The experimental points present the errors as vertical bars and the associated time bin width as horizontal bars. The initial time is taken at August 7th. Fitting the data with a cosinusoidal function with period of 1 year and phase at 152.5 days, the following amplitudes are obtained: $(0.0195 \pm 0.0031) \text{ cpd/kg/keV}$ and $-(0.0009 \pm 0.0019) \text{ cpd/kg/keV}$, respectively. Thus, a clear modulation is present in the lowest energy region, while it is absent just above.

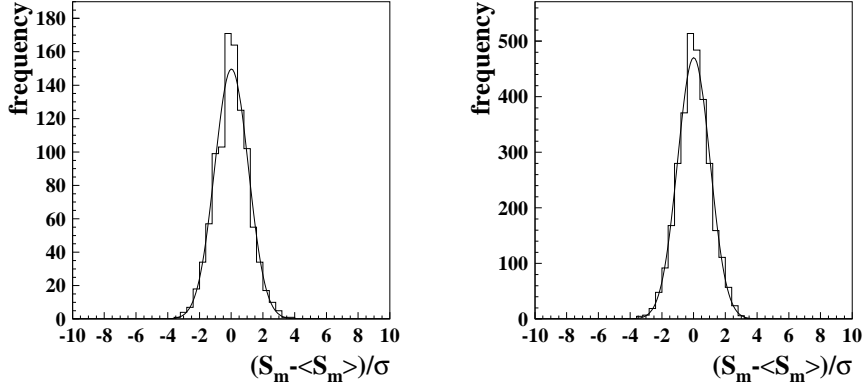


Figure 13: Distributions of the variable $\frac{S_m - \langle S_m \rangle}{\sigma}$ (where σ is the error associated to the S_m) evaluated for each detector, for each annual cycle and each considered energy bin: i) in the region of interest for the observed modulation, 2–6 keV (left panel); ii) including also the energy region just above, 2–14 keV (right panel). See text.

6.2 The investigation of possible systematic effects and side reactions

As previously mentioned – to mimic the annual modulation signature a systematic effect or side reaction should not only be quantitatively significant, but also able to satisfy the six requirements as for a WIMP induced effect (see §3.3); no effect able to mimic the signature has been found. A careful investigation of all the known possible sources of systematics and side reactions has been regularly carried out by DAMA/NaI

Table 3: Modulation amplitudes obtained by fitting the time behaviours of the main running parameters including a WIMP-like cosine modulation. These running parameters, acquired with the production data, are: i) the operating temperature of the detectors; ii) the HP Nitrogen flux in the inner Cu box housing the detectors; iii) the pressure of the HP Nitrogen atmosphere of the inner Cu box housing the detectors; iv) the environmental Radon in the inner part of the barrack from which the detectors are however excluded (see text); v) the hardware rate above single photoelectron threshold. See also the discussion in the whole section.

	DAMA/NaI-5	DAMA/NaI-6	DAMA/NaI-7
Temperature	$-(0.033 \pm 0.050)^\circ\text{C}$	$(0.021 \pm 0.055)^\circ\text{C}$	$-(0.030 \pm 0.056)^\circ\text{C}$
Flux	$(0.03 \pm 0.08) \text{ l/h}$	$(0.05 \pm 0.14) \text{ l/h}$	$(0.07 \pm 0.14) \text{ l/h}$
Pressure	$-(0.6 \pm 1.7)10^{-3} \text{ mbar}$	$(0.5 \pm 2.5)10^{-3} \text{ mbar}$	$(0.2 \pm 2.8)10^{-3} \text{ mbar}$
Radon	$-(0.09 \pm 0.17) \text{ Bq/m}^3$	$(0.06 \pm 0.14) \text{ Bq/m}^3$	$-(0.02 \pm 0.03) \text{ Bq/m}^3$
Hardware rate	$(0.10 \pm 0.17)10^{-2} \text{ Hz}$	$-(0.09 \pm 0.19)10^{-2} \text{ Hz}$	$-(0.22 \pm 0.19)10^{-2} \text{ Hz}$

and presented at time of each data release [60, 61, 63, 64]. In particular, in ref. [64] a detailed discussion has been carried out considering in the quantitative evaluations the data of DAMA/NaI-3 and -4. The same analysis is presented in the following considering in the quantitative evaluations the data of the DAMA/NaI-5 to -7 running periods; it offers a general description of this approach as well.

First of all the time behaviours of the main running parameters acquired with the production data have been investigated. In particular, the modulation amplitudes given in Table 3 (see also next subsections) have been obtained for each annual cycle when fitting the behaviours including a WIMP-like cosine modulation. As it can be seen, all the measured amplitudes are compatible with zero.

6.2.1 The Radon

As already discussed elsewhere [41, 64], the detectors are excluded from the environmental air which contains traces of radioactive Radon gas ($^{222}\text{Rn} - T_{1/2} = 3.82$ days – and of $^{220}\text{Rn} - T_{1/2} = 55$ s – isotopes, which belong to the ^{238}U and ^{232}Th chains, respectively), whose daughters attach themselves to surfaces by various processes. In fact: i) the walls, the floor and the top of the installation are insulated by Supronyl (permeability: $2 \cdot 10^{-11} \text{ cm}^2/\text{s}$ [94]) and a large flux of HP Nitrogen is released in the closed space of that inner barrack; an Oxygen level alarm informs the operator before entering it, when necessary; ii) the whole passive shield is sealed in a plexiglas box and maintained continuously in HP Nitrogen atmosphere in slight overpressure with respect to the environment as well as the upper glove box for calibrating the

detectors; iii) the detectors are housed in an inner sealed Cu box also maintained continuously in HP Nitrogen atmosphere in slight overpressure with respect to the environment; the Cu box can enter in contact only with the upper glove box – during calibrations – which is also continuously maintained in HP Nitrogen atmosphere in slightly overpressure with respect to the external environment.

Notwithstanding the above considerations, the Radon in the installation outside the plexiglas box, containing the passive shield, is continuously monitored; it is at level of sensitivity of the used Radonmeter (see Fig. 14). No modulation of external Radon, from which the detectors are anyhow excluded, is observed as quantitatively reported in Table 3.

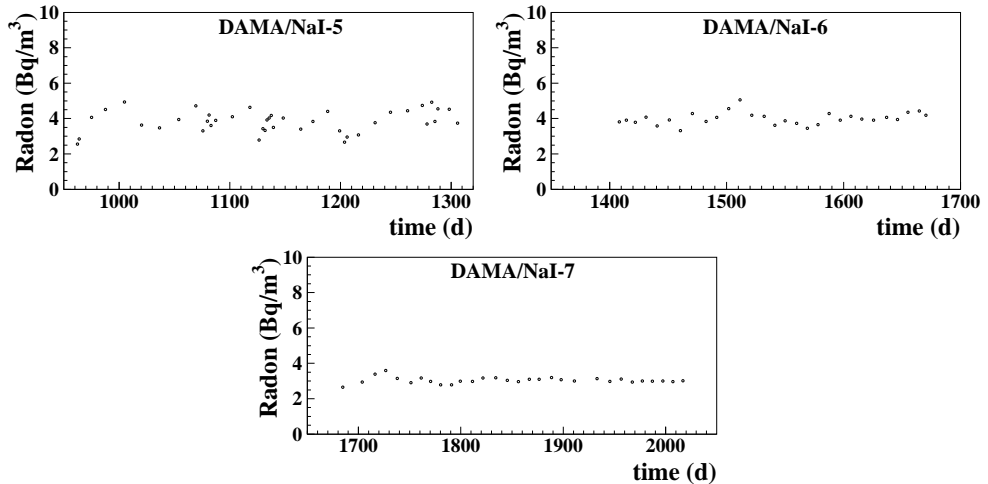


Figure 14: Time behaviours of the environmental Radon in the inner part of the barrack (from which the detectors are however excluded; see text) during the DAMA/NaI-5 to -7 running periods, respectively. The measured values are at the level of sensitivity of the used radonmeter.

In Fig. 15 the distribution of the relative variations of the HP Nitrogen flux in the inner Cu box housing the detectors and of its pressure as measured during the DAMA/NaI-5 to -7 running periods are shown (the typical flux mean value for each annual cycle is of order of $\simeq 260$ l/h and the typical overpressure mean value is of order of 2 mbar).

As already reported in ref. [64], also possible Radon trace in the HP Nitrogen atmosphere inside the Cu box has been estimated by searching for the double coincidences of the gamma-rays (609 and 1120 keV) from ^{214}Bi Radon daughter, obtaining an upper limit on the possible Radon concentration in the Cu box HP Nitrogen atmosphere: $< 4.5 \cdot 10^{-2}$ Bq/m³ (90% C.L.); thus, roughly $< 4 \cdot 10^{-4}$ cpd/kg/keV can be expected from this source in the lowest energy bins of interest from the obtained result on the WIMP annual modulation signature [64]. This has allowed us to show that even an hypothetical, e.g. 10%, modulation of possible Radon in the HP Nitrogen Cu box atmosphere would correspond to $< 0.2\%$ of the observed modulation amplitude.

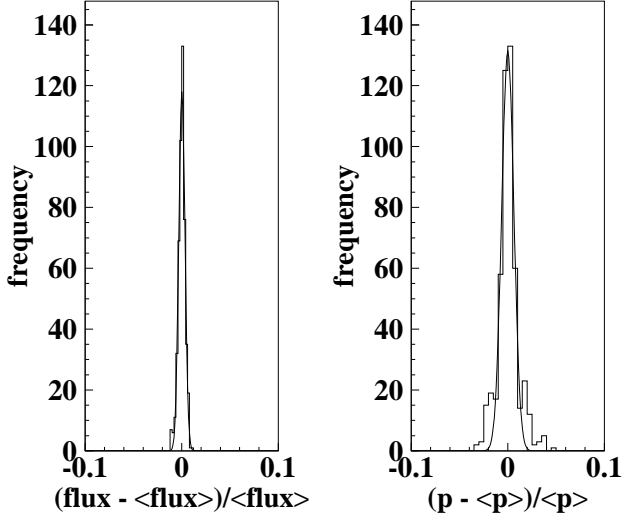


Figure 15: Distribution of the relative variations of the HP Nitrogen flux in the inner Cu box housing the detectors and of its pressure as measured during the DAMA/NaI-5 to -7 running periods.

Finally, it is worth to note that, while the possible presence of a sizeable quantity of Radon nearby a detector would forbid the investigation of the WIMP annual modulation signature (since every Radon variation would induce variation in the measured background and the continuous pollution of the exposed surfaces by the non-volatile daughters), it cannot mimic the WIMP annual modulation signature in experiments such as DAMA/NaI which record the whole energy distribution. In fact, possible presence of Radon variation can be easily identified in this case, since it would induce rate variation also in other energy regions than the one of interest for the WIMP search, that is some of the six requirements of the WIMP annual modulation signature would fail.

In conclusion, no significant effect is possible from the Radon.

6.2.2 The temperature

To avoid any significant temperature variation and, in particular, to maintain suitably stable the temperature of the electronic devices the installation, where the $\simeq 100$ kg NaI(Tl) set-up is operating, is air-conditioned. Moreover, the operating temperature of the detectors in the Cu box (stored with the production data) is read out by a probe located inside the multi-tons passive shield, whose huge heat capacity assures further a relevant stability of the detectors' operating temperature [41, 60, 61, 64, 95].

Information for the new DAMA/NaI-5 to 7 running periods can be derived from Fig. 16; moreover, no evidence of any operating temperature modulation has been observed as quantitatively reported in Table 3. Notwithstanding, to properly evaluate the real effect of possible variations of the detectors' operating temperature on the light output, we consider – according to the procedure given in ref. [64] – the distribution of

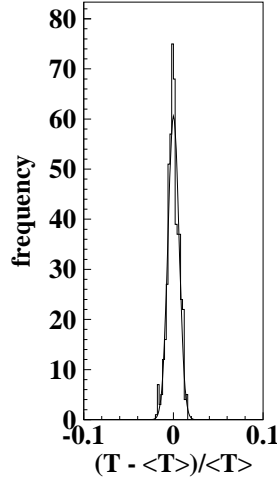


Figure 16: Distribution of the relative variations of the operating temperature measured during the DAMA/NaI-5 to -7 running periods.

the root mean square temperature variation within periods with the same calibration factors (typically $\simeq 7$ days); this is given in Fig. 17 cumulatively for the three data sets.

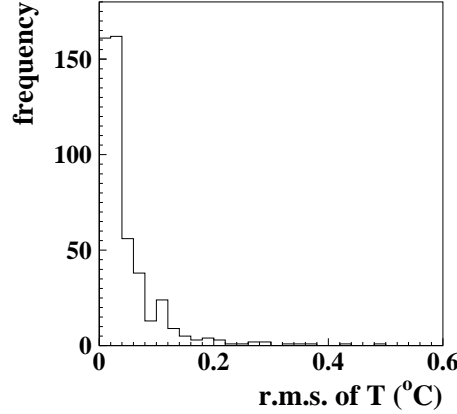


Figure 17: Distribution of the root mean square (r.m.s.) detectors' operating temperature variation within periods with the same calibration factors (typically $\simeq 7$ days) during the DAMA/NaI-5 to -7 running periods. The mean value is 0.05 $^{\circ}\text{C}$.

Considering the obtained mean value of the root mean square detectors' operating temperature variation: $\simeq 0.05$ $^{\circ}\text{C}$, and the known value of the slope of the light output around its value: $\lesssim -0.2\%/\text{ }^{\circ}\text{C}$, the relative light output variation is $\lesssim 10^{-4}$, which corresponds to $\lesssim 0.5\%$ of the modulation amplitude observed in the lowest energy region of the production data, S_m^{obs} , since the counting rate is $\simeq 1.0$ cpd/kg/keV in the region of interest [64, 59] and S_m^{obs} is $\simeq 0.02$ cpd/kg/keV (see previous section).

Thus, any significant effect from the detectors' operating temperature is further excluded. As in ref [64], for the sake of completeness, we comment that sizeable temperature variations could also induce variations in the electronic noise, in the Radon release from the rocks and, therefore, in the environmental background; these specific topics will be further analysed in the following, where cautious upper limits on their possible effect are given.

Finally, it is worth to remark that any hypothetical effect induced by temperature variations would fail at least some of the six requirements needed to mimic the annual modulation signature (such as e.g. the 4th and the 5th).

In conclusion, all the arguments given above exclude any role of possible effects on the observed rate modulation correlated with temperature.

6.2.3 The noise

Despite the stringent used noise rejection procedure (see refs. [41, 61, 63, 64] and the brief mention in §4.1), the role of possible noise tail in the data after the noise rejection has been quantitatively investigated [64].

In particular, the hardware rate of each one of the nine detectors above a single photoelectron, R_{Hj} (j identifies the detector), can be considered; in fact, it is significantly determined by the noise. For this purpose the variable $R_H = \Sigma_j(R_{Hj} - \langle R_{Hj} \rangle)$ can be built (where in our case $\langle R_{Hj} \rangle \lesssim 0.25$ Hz [41]); its time behaviour during the DAMA/NaI-5 to -7 running periods is shown in Fig. 18.

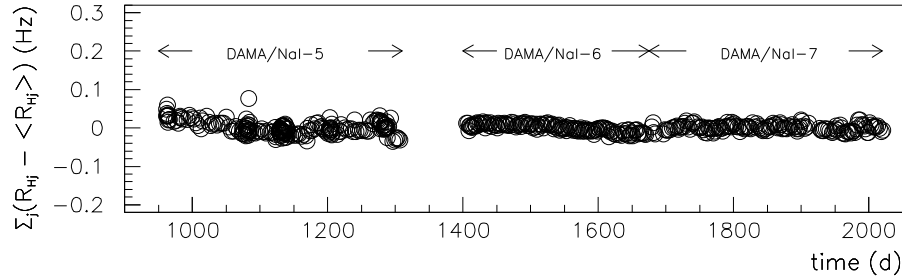


Figure 18: Time behaviour of the variable $R_H = \Sigma_j(R_{Hj} - \langle R_{Hj} \rangle)$, where R_{Hj} is the hardware rate of each one of the nine detectors above single photoelectron threshold (that is including the noise), j identifies the detector and $\langle R_{Hj} \rangle$ is the mean value of R_{Hj} in the corresponding running period.

As it can be seen in Fig. 19, the cumulative distribution of R_H for the DAMA/NaI-5 to -7 running periods shows a gaussian behaviour with $\sigma = 0.5\%$, value well in agreement with that expected on the basis of simple statistical arguments.

Moreover, by fitting the time behaviour of R_H in the three data taking periods – including a WIMP-like modulated term – a modulation amplitude compatible with zero: $-(0.06 \pm 0.11) \cdot 10^{-2}$ Hz, is obtained. From this value the upper limit at 90% C.L. on the modulation amplitude can be derived: $< 1.3 \cdot 10^{-3}$ Hz. Since the typical noise contribution to the hardware rate of each one of the 9 detectors is $\simeq 0.10$ Hz, the upper limit on the noise relative modulation amplitude is given by: $\frac{1.3 \cdot 10^{-3} \text{ Hz}}{9 \times 0.10 \text{ Hz}} \simeq 1.4 \cdot 10^{-3}$ (90% C.L.). Therefore, even in the worst hypothetical case of a 10% contamination

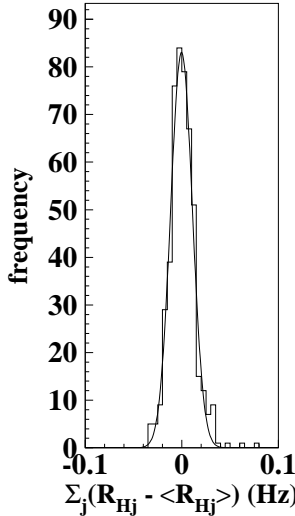


Figure 19: Distributions of R_H during the DAMA/NaI-5 to -7 running periods; see text.

of the residual noise – after rejection – in the counting rate, the noise contribution to the modulation amplitude in the lowest energy bins would be $< 1.4 \cdot 10^{-4}$ of the total counting rate. This means that an hypothetical noise modulation could account at maximum for absolute amplitudes of the order of few 10^{-4} cpd/kg/keV, that is $< 1\%$ of the observed annual modulation amplitude [63].

In conclusion, there is no evidence for any role of an hypothetical tail of residual noise after rejection.

6.2.4 The efficiencies

The behaviour of the used efficiencies during the whole data taking periods has even been investigated. Their possible time variation depends essentially on the stability of the efficiencies related to the previously mentioned acceptance windows, which are regularly measured by dedicated calibrations (see e.g. ref. [41, 61, 63]).

In particular, we show in Fig. 20 the percentage variations of the efficiency values in the (2-8) keV energy interval considering 2 keV bins. They show a gaussian distribution with $\sigma = 0.5\%$ for DAMA/NaI-5 to -7, cumulatively. Moreover, we have verified that the time behaviour of these percentage variations does not show any modulation with period and phase expected for a possible WIMP signal. In Table 4 the modulation amplitudes of the efficiencies in each energy bin between 2 and 10 keV are reported, showing that they are all consistent with zero. In particular, modulation amplitudes – considering the three periods together – equal to $(0.7 \pm 1.0) \cdot 10^{-3}$ and $(0.1 \pm 0.8) \cdot 10^{-3}$ are found in the (2-4) keV and (4-6) keV energy bins, respectively; both consistent with zero.

Thus, also the unlikely idea of a possible role played by the efficiency values in the observed effect is ruled out.

Table 4: Modulation amplitudes obtained by fitting the time behaviour of the efficiencies including a WIMP-like cosine modulation for the DAMA/NaI-5 to -7 running periods.

Energy	Amplitude ($\times 10^{-3}$)		
	DAMA/NaI-5	DAMA/NaI-6	DAMA/NaI-7
2-4 keV	(1.0 \pm 3.3)	(1.8 \pm 1.5)	-(0.4 \pm 1.5)
4-6 keV	(1.6 \pm 2.3)	(0.7 \pm 1.3)	-(0.9 \pm 1.2)
6-8 keV	(1.0 \pm 1.8)	-(0.1 \pm 1.0)	(0.3 \pm 1.0)
8-10 keV	(0.7 \pm 1.3)	(0.3 \pm 0.8)	(1.5 \pm 1.0)

6.2.5 The calibration factor

In long term running conditions, the knowledge of the energy scale is assured by periodical calibration with ^{241}Am source and by continuously monitoring within the same production data (grouping them each \simeq 7 days) the position and resolution of the ^{210}Pb peak (46.5 keV), mentioned in §4.1 [41, 60, 61, 63, 64]. Although it is highly unlikely that a variation of the calibration factor (proportionality factor between the area of the recorded pulse and the energy), $tdcal$, could play any role, according to e.g. ref. [64] a quantitative investigation on that point has been carried out.

For this purpose, the distribution of the relative variations of $tdcal$ – without applying any correction – estimated from the position of the ^{210}Pb peak for all the

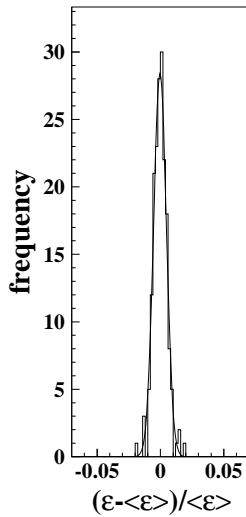


Figure 20: Distribution of the percentage variations of the efficiency values with the respect to their mean values during the DAMA/NaI-5 to -7 running periods; see text.

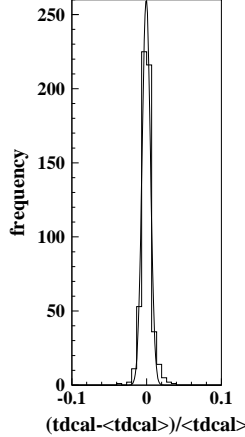


Figure 21: Distribution of the percentage variations of the energy scale factors ($tdcal$) in the DAMA/NaI-5 to -7 running periods without applying any correction; see text. The standard deviation is 0.5%.

9 detectors during the DAMA/NaI-5 to -7 running periods is given in Fig. 21. This distribution shows a gaussian behaviour with $\sigma \lesssim 0.5\%$. Since the results of the routine calibrations are obviously properly taken into account in the data analysis, such a result allows to conclude that the energy calibration factor for each detector is known with an uncertainty $\ll 1\%$ within every 7 days interval.

As discussed also in ref. [64], the variation of the calibration factor for each detector, within each interval of $\simeq 7$ days, would give rise to an additional energy spread (σ_{cal}) besides the detector energy resolution (σ_{res}). The total energy spread can be, therefore, written as: $\sigma = \sqrt{\sigma_{res}^2 + \sigma_{cal}^2} \simeq \sigma_{res} \cdot [1 + \frac{1}{2} \cdot (\frac{\sigma_{cal}}{\sigma_{res}})^2]$; clearly the contribution due to the calibration factor variation is negligible since $\frac{1}{2} \cdot (\frac{\sigma_{cal}}{\sigma_{res}})^2 \lesssim 7.5 \cdot 10^{-4} \frac{E}{20keV}$ (where the adimensional ratio $\frac{E}{20keV}$ accounts for the energy dependence of this limit value). This order of magnitude is confirmed by a MonteCarlo calculation, which credits – as already reported in ref. [64] a maximum value of the effect of similar variations of $tdcal$ on the modulation amplitude equal to $1.6 \cdot 10^{-4}$, giving an upper limit $< 1\%$ of the modulation amplitude measured at very low energy.

Thus, also the unlikely idea that the calibration factor could play a role can be safely ruled out.

6.2.6 The background

Similarly as done for the previous data sets (see e.g. ref. [64]), in order to verify the absence of any significant background modulation, the energy distribution measured during the data taking periods in energy regions not of interest for the WIMP-nucleus elastic scattering can be investigated in order to verify if the modulation detected in the lowest energy region could be ascribed to a background modulation. In fact, the background in the lowest energy region can be essentially due to "Compton" electrons, X-rays and/or Auger electrons, muon induced events, etc., which are strictly correlated

with the events in the higher energy part of the spectrum. Thus, if a modulation with time detected in the lowest energy region would be due to a modulation of the background (instead of the possible signal) with time, an equal or larger (sometimes much larger) modulation in the higher energy regions should be present. For this purpose, we have investigated the rate integrated above 90 keV, R_{90} , as a function of the time.

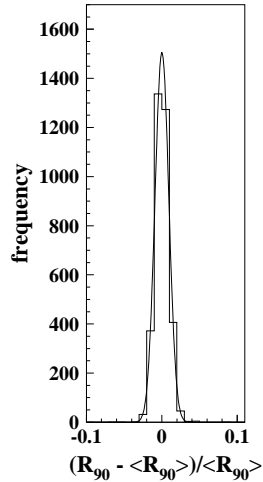


Figure 22: Distributions of the percentage variations of R_{90} with respect to the mean values for all the detectors in the DAMA/NaI-5 to -7 running periods; see text.

In Fig. 22 the distribution of the percentage variations of R_{90} with respect to the mean values for all the nine detectors during the DAMA/NaI-5 to -7 running periods is given. They show cumulative gaussian behaviours with $\sigma \simeq 0.9\%$, well accounted by the statistical spread expected from the used sampling time. This result excludes any significant background variation.

Moreover, fitting the time behaviour of R_{90} , a WIMP-like modulation amplitude compatible with zero is found in each running period: (0.09 ± 0.32) cpd/kg, (0.06 ± 0.33) cpd/kg and $-(0.03 \pm 0.32)$ cpd/kg for DAMA/NaI-5, DAMA/NaI-6 and DAMA/NaI-7, respectively. This excludes the presence of a background modulation in the whole energy spectrum at a level much lower than the effect found in the lowest energy region; in fact, otherwise – considering the R_{90} mean values – a modulation amplitude of order of tens cpd/kg, that is $\simeq 100 \sigma$ far away from the measured value, would be present.

A similar analysis performed on the data collected just above the energy region, where the modulation is observed, that is in $(6 - 10)$ keV, gives: $-(0.0076 \pm 0.0065)$ cpd/kg/keV, (0.0012 ± 0.0059) cpd/kg/keV and (0.0035 ± 0.0058) cpd/kg/keV for the three periods, respectively.

The results of this subsection also demonstrate that the production data satisfy the 4th requirement of the WIMP annual modulation signature.

Notwithstanding the results given above already account also for the background

component due to the neutrons, a further additional independent and cautious analysis to estimate their possible contribution has been given in ref. [64]. In particular, the effect of the about 1 m concrete (made from the Gran Sasso rock material) which, as known, almost fully surrounds (outside the barrack) the DAMA/NaI passive shield – acting as a further neutron moderator – has not been cautiously included in these estimates, which are recalled in the following.

As regards the thermal neutrons, the neutron capture reactions $^{23}\text{Na}(n, \gamma)^{24}\text{Na}$ and $^{23}\text{Na}(n, \gamma)^{24m}\text{Na}$ (cross section to thermal neutrons equal to 0.10 and 0.43 barn, respectively [96]) have been investigated. The capture rate is: $\simeq 0.2$ captures/day/kg since the thermal neutron flux has been measured to be $1.08 \cdot 10^{-6}$ neutrons $\cdot \text{cm}^{-2} \cdot \text{s}^{-1}$ [38]¹¹. Assuming cautiously a 10% modulation of the thermal neutrons flux, the corresponding modulation amplitude in the lowest energy region has been calculated by MonteCarlo program to be $< 10^{-5}$ cpd/kg/keV, that is $< 0.05\%$ of the modulation amplitude we found in the lowest energy interval of the production data. In addition, a similar contribution cannot anyhow mimic the annual modulation signature since it would fail some of the six requirements quoted in §3.3 (such as e.g. the 4th and the 5th).

A similar analysis has also been carried out for the fast neutrons case [64]. From the fast neutron flux measured at the Gran Sasso underground laboratory, $0.9 \cdot 10^{-7}$ neutrons $\cdot \text{cm}^{-2} \cdot \text{s}^{-1}$ [39], the differential counting rate above 2 keV has been estimated by MonteCarlo to be $\simeq 10^{-3}$ cpd/kg/keV. Therefore, assuming – also in this case – cautiously a 10% modulation of the fast neutron flux, the corresponding modulation amplitude is $< 0.5\%$ of the modulation amplitude found in the lowest energy interval. Moreover, also in this case some of the six requirements mentioned above would fail.

Finally, possible side reactions have been also carefully searched for. The only process which has been found as an hypothetical possibility is the muon flux modulation reported by the MACRO experiment [37]. In fact, MACRO has observed that the muon flux shows a nearly sinusoidal time behaviour with one year period and maximum in the summer with amplitude of $\simeq 2\%$; this muon flux modulation is correlated with the temperature of the atmosphere. A simple calculation to estimate the modulation amplitude expected from this process in our set-up has been introduced in ref. [64] and is recalled in the following. In fact, the muon flux (Φ_μ) and the yield of neutrons produced by muons measured at the underground Gran Sasso National Laboratory (Y) are: $\Phi_\mu \simeq 20$ muons $\text{m}^{-2}\text{d}^{-1}$ [37] and $Y \simeq (1 - 7) \cdot 10^{-4}$ neutrons per muon per g/cm^2 [97], respectively. Thus, the fast neutron rate produced by muons is given by: $R_n = \Phi_\mu \cdot Y \cdot M_{eff}$, where M_{eff} is the effective mass where muon interactions can give rise to events detected in the DAMA set-up. Consequently, the annual modulation amplitude in the lowest energy region induced in our experiment by a muon flux modulation as measured by MACRO [37] can be estimated as: $S_m^{(\mu)} = R_n \cdot g \cdot \epsilon \cdot f_{\Delta E} \cdot f_{single} \cdot 2\% / (M_{set-up} \cdot \Delta E)$, where g is a geometrical factor, ϵ is the detection efficiency for elastic scattering interactions, $f_{\Delta E}$ is the acceptance of the considered energy window ($E \geq 2$ keV), f_{single} is the "single hit" efficiency and 2% is the MACRO measured effect. Since $M_{set-up} \simeq 100$ kg and $\Delta E \simeq 4$ keV, assuming the very cautious values $g \simeq \epsilon \simeq f_{\Delta E} \simeq f_{single} \simeq 0.5$ and $M_{eff} = 15$ t, one obtains:

¹¹Consistent upper limit on the thermal neutron flux have been obtained with the $\simeq 100$ kg DAMA NaI(Tl) set-up considering these same capture reactions [41].

$S_m^{(\mu)} < (1 - 7) \cdot 10^{-5}$ cpd/kg/keV, that is $< 0.3\%$ of the modulation amplitude we observe [63]. We stress that – in addition – the latter value has been overestimated of orders of magnitude both because of the extremely cautious values assumed in the calculation and, as mentioned, of the omission of the effect of the $\simeq 1$ m concrete neutron moderation. Finally, we remark that not only the modulation of the muon flux observed by MACRO would give rise in our set-up to a quantitatively negligible effect, but – in addition – some of the six requirements necessary to mimic the annual modulation signature (such as e.g. the 4th and the 5th) would fail. Therefore, it can be safely ignored.

Just for the sake of completeness, we remind that the contribution of solar neutrinos, whose flux is also expected to be modulated, is many orders of magnitude lower than the measured rate [98].

In conclusion, the results presented in this section demonstrate that the production data satisfy the 4th requirement of a WIMP induced effect and – at the same time – exclude that the annual modulation observed in the lowest energy region could be ascribed to modulation of any kind of possible background.

6.3 Conclusions on the DAMA/NaI model independent result

No modulation has been found in any of the considered possible source of systematics; thus, upper limits (90% C.L.) on the possible contributions to a modulated amplitude have been calculated and are summarized in Table 5. In particular, they cannot account for the measured modulation because quantitatively not relevant and, as discussed in details already in ref. [64], none of them is able to mimic the observed effect; in fact, none can satisfy all the above mentioned peculiarities of the signature.

The quantitative investigations discussed above offer a complete analysis of known sources of possible systematic effects. We can conclude that a relative systematic error, affecting the energy spectrum, of order of $\lesssim 10^{-3}$ is credited by these investigations, while the results on the analysis of R_{90} exclude the presence of a possible background modulation even at more stringent level. Furthermore, no systematic effect or side reaction able to mimic a WIMP induced effect, that is to be not only quantitatively significant, but also able to satisfy all the many requirements of the signature (see §3.3), has been found.

In conclusion, the presence of an annual modulation in the residual rate in the lowest energy interval (2 – 6) keV with all the features expected for a WIMP component in the galactic halo is supported by the data at 6.3σ C.L.

7 Corollary results: quests for a candidate particle in some model frameworks

On the basis of the previous main result, a corollary investigation can also be pursued on the nature and coupling of a WIMP candidate. This latter investigation is instead model dependent and – considering the large uncertainties which exist on the astrophysical, nuclear and particle physics assumptions and parameters needed in the

Table 5: Summary of the results obtained by investigating possible sources of systematics or of side reactions in the data of the DAMA/NaI-5 to 7 running periods. None able to give a modulation amplitude different from zero has been found; thus cautious upper limits (90% C.L.) on the possible contributions to a modulation amplitude have been calculated and are shown here in terms of the measured model independent modulation amplitude, S_m^{obs} , we have observed (see §6.1). As it can be seen none (nor their cumulative) effect could account for the measured modulation; moreover, as discussed in details already in ref.[64], none of them could mimic the signature.

Source	Main comment	Cautious upper limit (90% C.L.)
Radon	Sealed Cu Box in HP Nitrogen atmosphere	$< 0.2\%S_m^{obs}$
Temperature	Air conditioning	$< 0.5\%S_m^{obs}$
Noise	Efficient rejection	$< 1\%S_m^{obs}$
Energy scale	Routine + intrinsic calibrations	$< 1\%S_m^{obs}$
Efficiencies	Mainly routine measurements	$< 1\%S_m^{obs}$
Background	No modulation observed above 6 keV; this limit includes possible effect of thermal and fast neutrons	$< 0.5\%S_m^{obs}$
Side reactions	From muon flux variation measured by MACRO	$< 0.3\%S_m^{obs}$
In addition: no effect can mimic the signature		

calculations – has no general meaning (as it is also the case of exclusion plots and of the WIMP parameters evaluated in indirect search experiments). Thus, it should be handled in the most general way as we have preliminarily pointed out with time in the past [60, 61, 62, 63, 64, 65, 66, 11] and we will again show in the following sections. The results we will discuss are, of course, not exhaustive and many other different allowed regions can be obtained by varying the assumptions within the many possible model frameworks, which at present level of knowledge cannot be disentangled (e.g. open questions: i) which is the right nature for the WIMP particle; ii) which is its right couplings with ordinary matter; iii) which are the right form factors and related parameters for each target nucleus; iv) which is the right spin factor for each target nucleus; v) which are the right scaling laws; vi) which is the right halo model and related parameters; vii) which are the right values of the experimental parameters which we can determine only with associated uncertainties; etc.). The situation is analogous for results presented in form of exclusion plots, which also have not an "universal" meaning, as well as for the results of WIMP specific parameters inferred by indirect searches.

7.1 Estimates of WIMP direct detection rates

In the following the main bases necessary to perform model dependent analyses in this field are given. The approximations and intrinsic uncertainties can be inferred straight-forward.

7.1.1 WIMP-nucleus elastic scattering

The studied process is the WIMP-nucleus elastic scattering and the measured quantity is the recoil energy. In the general form the differential energy distribution of the recoil nuclei can be calculated [46, 99] by means of the differential cross section of the WIMP-nucleus elastic processes

$$\begin{aligned} \frac{d\sigma}{dE_R}(v, E_R) &= \left(\frac{d\sigma}{dE_R} \right)_{SI} + \left(\frac{d\sigma}{dE_R} \right)_{SD} = \\ &= \frac{2G_F^2 m_N}{\pi v^2} \{ [Zg_p + (A-Z)g_n]^2 F_{SI}^2(E_R) + 8\Lambda^2 J(J+1)F_{SD}^2(E_R) \}, \end{aligned} \quad (8)$$

where: G_F is the Fermi coupling constant; m_N is the nucleus mass; v is the WIMP velocity in the laboratory frame; $E_R = m_{WN}^2 v^2 (1 - \cos\theta^*) / m_N$ (with m_{WN} WIMP-nucleus reduced mass and θ^* scattering angle in the WIMP-nucleus c.m. frame) is the recoil energy; Z is the nuclear charge and A is the atomic number; $g_{p,n}$ are the effective WIMP-nucleon coupling strengths for SI interactions; $\Lambda^2 J(J+1)$ is a spin factor. Moreover, $F_{SI}^2(E_R)$ is the SI form factor (see later), while $F_{SD}^2(E_R)$ is the SD form factor (see later) for which an universal formulation is not possible since in this case the internal degrees of the WIMP particle model (e.g. supersymmetry in case of neutralino) cannot be completely decoupled from the nuclear ones. It is worth to note that this adds significant uncertainty in the model dependent results.

Furthermore, it can be demonstrated that $\Lambda = \frac{a_p < S_p > + a_n < S_n >}{J}$ with J nuclear spin, with $a_{p,n}$ effective WIMP-nucleon coupling strengths for SD interaction and with $< S_{p,n} >$ mean values of the nucleon spins in the nucleus. Therefore, the differential cross section and, consequently, the expected energy distribution depend on the WIMP mass and on four unknown parameters of the theory: $g_{p,n}$ and $a_{p,n}$.

The total cross section for WIMP-nucleus elastic scattering can be obtained by integrating equation (8) over E_R up to $E_{R,max} = \frac{2m_{WN}^2 v^2}{m_N}$:

$$\begin{aligned} \sigma(v) &= \int_0^{E_{R,max}} \frac{d\sigma}{dE_R}(v, E_R) dE_R = \frac{4}{\pi} G_F^2 m_{WN}^2 \{ [Zg_p + (A-Z)g_n]^2 G_{SI}(v) + \\ &+ 8 \frac{J+1}{J} [a_p < S_p > + a_n < S_n >]^2 G_{SD}(v) \}. \end{aligned} \quad (9)$$

Here $G_{SI}(v) = \frac{1}{E_{R,max}} \int_0^{E_{R,max}} F_{SI}^2(E_R) dE_R$; $G_{SD}(v)$ can be derived straightforward.

The standard point-like cross section can be evaluated in the limit $v \rightarrow 0$ (that is in the limit $G_{SI}(v)$ and $G_{SD}(v) \rightarrow 1$). Knowing that $< S_{p,n} > = J = 1/2$ for single nucleon, the SI and SD point-like cross sections on proton and on neutron can be written as:

$$\sigma_{p,n}^{SI} = \frac{4}{\pi} G_F^2 m_{W(p,n)}^2 g_{p,n}^2 \quad \sigma_{p,n}^{SD} = \frac{32}{\pi} \frac{3}{4} G_F^2 m_{W(p,n)}^2 a_{p,n}^2, \quad (10)$$

where $m_{Wp} \simeq m_{Wn}$ are the WIMP-nucleon reduced masses.

As far as regards the SI case, the first term within squared brackets in eq. (9) can be arranged in the form

$$[Zg_p + (A - Z)g_n]^2 = \left(\frac{g_p + g_n}{2}\right)^2 \left[1 - \frac{g_p - g_n}{g_p + g_n} \left(1 - \frac{2Z}{A}\right)\right]^2 A^2 = g^2 \cdot A^2. \quad (11)$$

Considering $\frac{Z}{A}$ nearly constant for the nuclei typically used in direct searches for Dark Matter particles, the coupling term g is generally assumed – in a first approximation – as independent on the used target nucleus. Under this assumption, the nuclear parameters can be decoupled from the particle parameters and a generalized SI WIMP-nucleon cross section: $\sigma_{SI} = \frac{4}{\pi} G_F^2 m_{Wp}^2 g^2$, can be conveniently introduced.

As far as regards the SD couplings, let us now introduce the useful notations [65]

$$\bar{a} = \sqrt{a_p^2 + a_n^2}, \quad tg\theta = \frac{a_n}{a_p}, \quad \sigma_{SD} = \frac{32}{\pi} \frac{3}{4} G_F^2 m_{Wp}^2 \bar{a}^2, \quad (12)$$

where σ_{SD} is a suitable SD WIMP-nucleon cross section. The SD cross sections on proton and neutron can be, then, written as:

$$\sigma_p^{SD} = \sigma_{SD} \cdot \cos^2\theta \quad \sigma_n^{SD} = \sigma_{SD} \cdot \sin^2\theta. \quad (13)$$

In conclusion, equation (8) can be re-written in terms of σ_{SI} , σ_{SD} and θ as:

$$\frac{d\sigma}{dE_R}(v, E_R) = \frac{m_N}{2m_{Wp}^2 v^2} \cdot \Sigma(E_R), \quad (14)$$

with

$$\begin{aligned} \Sigma(E_R) = & \{ A^2 \sigma_{SI} F_{SI}^2(E_R) + \\ & + \frac{4}{3} \frac{(J+1)}{J} \sigma_{SD} [\langle S_p \rangle \cos\theta + \langle S_n \rangle \sin\theta]^2 F_{SD}^2(E_R) \}. \end{aligned} \quad (15)$$

The mixing angle θ is defined in the $[0, \pi]$ interval; in particular, θ values in the second sector account for a_p and a_n with different signs. As it can be noted from its definition [99], $F_{SD}^2(E_R)$ depends on a_p and a_n only through their ratio and, consequently, depends on θ , but it does not depend on \bar{a} .

Finally, setting the local WIMP density, $\rho_W = \xi \rho_0$, where ρ_0 is the local halo density and ξ ¹² ($\xi \leq 1$) is the fractional amount of local WIMP density, and the WIMP mass, m_W , one can write the energy distribution of the recoil rate (R) in the form

$$\begin{aligned} \frac{dR}{dE_R} = & N_T \frac{\rho_W}{m_W} \int_{v_{min}(E_R)}^{v_{max}} \frac{d\sigma}{dE_R}(v, E_R) v f(v) dv = \\ & N_T \frac{\rho_0 \cdot m_N}{2m_W \cdot m_{Wp}^2} \xi \Sigma(E_R) I(E_R), \end{aligned} \quad (16)$$

¹²Pay attention that in ref. [61, 63, 65, 66] the same symbol indicates instead a different quantity: $\xi = \rho_W / (0.3 \text{GeV} \text{cm}^{-3})$.

where: N_T is the number of target nuclei and $I(E_R) = \int_{v_{min}(E_R)}^{v_{max}} dv \frac{f(v)}{v}$ with $f(v)$ WIMP velocity distribution in the Earth frame; $v_{min} = \sqrt{\frac{m_N \cdot E_R}{2m_{WN}^2}}$ is the minimal WIMP velocity providing E_R recoil energy; v_{max} is the maximal WIMP velocity in the halo evaluated in the Earth frame.

The differential distribution of the detected energy, E_{det} , for a multiple-nuclei detector (as e.g. the NaI(Tl)) can be easily derived:

$$\frac{dR}{dE_{det}}(E_{det}) = \int K(E_{det}, E') \cdot \sum_{x=nucleus} \frac{dR_x}{dE_R} \left(E_R = \frac{E'}{q_x} \right) \cdot dE', \quad (17)$$

where q_x is the quenching factor for the x recoiling nucleus and $K(E_{det}, E')$ takes into account the response and energy resolution of the detector; generally it has a gaussian behaviour.

It is worth to remark, as it can be inferred by eq. (8), that only nuclei with spin different from zero are sensitive to WIMPs with both SI and SD couplings. This is the case of the ^{23}Na and ^{127}I nuclei, odd-nuclei with an unpaired proton, constituents of the DAMA/NaI detectors. Thus, the purely SI coupling scenario widely considered in this field represents only a particular case of the more general framework of a WIMP candidate with both mixed SI and SD couplings. Therefore, in the following analyses, we will consider some of the possible scenarios for the mixed SI and SD couplings and, then, also the sub-cases of pure SI and pure SD couplings.

7.1.2 WIMPs with *preferred inelastic scattering*

It has been suggested [27] also the possibility that the annual modulation of the low energy rate observed by DAMA/NaI could be induced by WIMPs with *preferred inelastic scattering*: relic particles that cannot scatter elastically off nuclei. As discussed in ref. [27], the inelastic Dark Matter could arise from a massive complex scalar split into two approximately degenerate real scalars or from a Dirac fermion split into two approximately degenerate Majorana fermions, namely χ_+ and χ_- , with a δ mass splitting. In particular, a specific model featuring a real component of the sneutrino, in which the mass splitting naturally arises, has been given in ref. [27] and mentioned here in §2. The detailed discussion of the theoretical arguments on such inelastic Dark Matter can be found in ref. [27]. In particular, there has been shown that for the χ_- inelastic scattering on target nuclei a kinematical constraint exists which favours heavy nuclei (such as ^{127}I) with respect to lighter ones (such as e.g. ^{nat}Ge) as target-detectors media. In fact, χ_- can only inelastically scatter by transitioning to χ_+ (slightly heavier state than χ_-) and this process can occur only if the χ_- velocity, v , is larger than:

$$v_{thr} = \sqrt{\frac{2\delta}{m_{WN}}}. \quad (18)$$

This kinematical constraint becomes increasingly severe as the nucleus mass, m_N , is decreased [27]. For example, if $\delta \gtrsim 100$ keV, a signal rate measured e.g. in Iodine will be a factor about 10 or more higher than that measured in Germanium [27]. Moreover, this model scenario implies some peculiar features when exploiting the WIMP annual

modulation signature [53]; in fact – with respect to the case of WIMP elastically scattering – it would give rise to an enhanced modulated component, S_m , with respect to the unmodulated one, S_0 , and to largely different behaviours with energy for both S_0 and S_m (both show a higher mean value) [27].

The *preferred inelastic* Dark Matter scenario [27] offers further possible model frameworks and has also the merit to naturally recover the sneutrino as a WIMP candidate (see e.g. §7.1.2).

The differential energy distribution of the recoil nuclei in the case of inelastic processes can be calculated by means of the differential cross section of the WIMP-nucleus inelastic processes:

$$\frac{d\sigma}{d\Omega^*} = \frac{G_F^2 m_{WN}^2}{\pi^2} [Zg_p + (A - Z)g_n]^2 F_{SI}^2(q^2) \cdot \sqrt{1 - \frac{v_{thr}^2}{v^2}}, \quad (19)$$

where $d\Omega^*$ is the differential solid angle in the WIMP-nucleus c.m. frame; q^2 is the squared three-momentum transfer.

In the inelastic process the recoil energy depends on the scatter angle, θ^* , in the c.m. frame according to:

$$E_R = \frac{2m_{WN}^2 v^2}{m_N} \cdot \frac{1 - \frac{v_{thr}^2}{2v^2} - \sqrt{1 - \frac{v_{thr}^2}{v^2}} \cdot \cos\theta^*}{2}. \quad (20)$$

Thus, we can write:

$$dE_R = \frac{2m_{WN}^2 v^2}{m_N} \cdot \sqrt{1 - \frac{v_{thr}^2}{v^2}} \cdot \frac{d\Omega^*}{4\pi}. \quad (21)$$

From eq. (19) and (21) we derive the differential cross section as a function of the recoil energy, E_R , and the WIMP velocity, v :

$$\frac{d\sigma}{dE_R}(v, E_R) = \frac{2G_F^2 m_N}{\pi v^2} [Zg_p + (A - Z)g_n]^2 F_{SI}^2(E_R). \quad (22)$$

Here we apply the relation $q^2 = 2m_N E_R$.

The minimal WIMP velocity, $v_{min}(E_R)$, providing E_R recoil energy in the inelastic process is:

$$v_{min}(E_R) = \sqrt{\frac{m_N E_R}{2m_{WN}^2}} \cdot \left(1 + \frac{m_{WN}\delta}{m_N E_R}\right), \quad (23)$$

and it is always $\geq v_{thr}$.

Finally, one can write the energy distribution of the recoil rate (R) in the form

$$\begin{aligned} \frac{dR}{dE_R} &= N_T \frac{\rho_W}{m_W} \int_{v_{min}(E_R)}^{v_{max}} \frac{d\sigma}{dE_R}(v, E_R) v f(v) dv = \\ &= N_T \frac{\rho_0 \cdot m_N}{2m_W \cdot m_{Wp}^2} \cdot A^2 \xi \sigma_p F_{SI}^2(E_R) \cdot I(E_R). \end{aligned} \quad (24)$$

Moreover, as derived in the case discussed in the previous subsection, also in the present case a generalized SI point-like WIMP-nucleon cross section: $\sigma_p =$

$\frac{4}{\pi} G_F^2 m_{Wp}^2 g^2$, can be defined. Finally, the extension of formula (24) e.g. to detectors with multiple nuclei can be easily derived.

In this scenario the modulated and the unmodulated components of the signal are function of $\xi\sigma_p$, m_W and δ .

7.1.3 The halo models

As discussed above, the expected counting rate for the WIMP elastic scattering depends on the local WIMP density, ρ_W , and on the WIMP velocity distribution, $f(v)$, at Earth's position. The experimental observations regarding the dark halo of our Galaxy do not allow to get information on them without introducing a model for the Galaxy matter density. An extensive discussion about models has been reported in ref. [11]. Here we present a brief introduction on this argument both to allow the reader to understand the complexity of this aspect and in the light of the results given in following subsections on the discussed quests.

Important information on the dark halo in the Galaxy can be derived from measurements of the rotational velocities of objects bounded in the gravitational galactic field. In fact, the following relation between the rotational velocity of an object placed at distance $r \equiv |\vec{r}|$ from the center of the Galaxy and the total mass, $M_{tot}(r) = \int_{r' < r} d^3r' \rho_{tot}(\vec{r}')$, inside the radius r can be obtained from the virial theorem:

$$v_{rot}^2(r) = \frac{GM_{tot}(r)}{r} \quad (25)$$

where G is the Newton's constant. The total mass density, $\rho_{tot}(\vec{r})$, can be expressed as the sum of the mass density of the dark halo, $\rho_{DM}(\vec{r})$, and the mass density of the visible component, $\rho_{vis}(\vec{r})$ that constitutes the bulge and the disk of the Galaxy. The gravitational potential $\Psi(\vec{r})$ is related to ρ_{tot} through the Poisson's equation:

$$\nabla^2 \Psi = -4\pi G \rho_{tot}. \quad (26)$$

The halo density profile $\rho_{DM}(\vec{r})$ can also be expressed in term of the distribution function of the WIMP in the six-dimensional phase space $F(\vec{r}, \vec{v})$:

$$\rho_{DM}(\vec{r}) \equiv \int F(\vec{r}, \vec{v}) d^3v \quad (27)$$

where \vec{r} and \vec{v} represent the position and velocity vectors in the rest frame of the Galaxy respectively.

Inverting eq. (27) and taking into account observational data it is, in principle, possible to calculate $F(\vec{r}, \vec{v})$ and, then, the WIMP velocity distribution function at the Earth position in the Galaxy:

$$f(\vec{v}) \equiv F(\vec{R}_0, \vec{v}) \quad (28)$$

where $R_0 \simeq 8.5$ kpc corresponds to the Earth distance from the center of the Galaxy along the direction of the galactic plane ($\vec{R}_0 \equiv (R_0, 0, 0)$). The inversion of eq. (27)

presents degeneracy problem that can be solved only requiring some degree of symmetry for the system. The velocity distribution function represents therefore an important source of uncertainties in the evaluation of expected counting rate for the WIMP component in the galactic halo.

As well as the velocity distribution function, two other quantities are of great importance to estimate the expected counting rate: the WIMP local velocity, $v_0 = v_{rot}(\vec{R}_0)$, and the local halo density $\rho_0 \equiv \rho_{DM}(\vec{R}_0)$ that appears as a multiplicative factor in the formula giving the expected counting rate. Since we are interested in the evaluation of local and rotational velocity of the WIMP at distance $r = R_0$, it is not necessary for our purpose a detailed description of the inner part of the Galaxy ($r \ll R_0$) where disk and bulge are dominant. Thus, it is possible to consider the bulge as a spherical density distribution with relevant contribution up to about 1 kpc and truncated at $r \simeq 2$ kpc from the center of Galaxy, and the disk as an exponential distribution which (according to most of the models) decreases up to 4 kpc where it can safely be neglected. Therefore, it is generally assumed that for $r \gtrsim R_0$ the dark matter is the dominant component.

The contribution of the visible matter has been considered in the calculation of the WIMP local velocity:

$$v_0^2 = v_{rot}^2(R_0) = \frac{G}{R_0} [M_{vis}(R_0) + M_{halo}(R_0)]. \quad (29)$$

A *maximal halo*, ρ_0^{max} , occurs when $M_{vis}(R_0) \ll M_{halo}(R_0)$; in this case the contribution to the rotational velocity is due to the halo; on the other hand, when for M_{vis} the maximum value compatible with observations is considered, a *minimal halo*, ρ_0^{min} , occurs and only a fraction of v_0 is supported by the dark halo.

The WIMP halo can be represented as a collisionless gas of particles whose distribution function satisfy the Boltzmann equation [100]. In general case the Boltzmann equation cannot be solved without reducing the complexity of the system. It is possible to consider models based on the Jeans or on the virial equations that describe a wide range of systems, but one cannot be sure that these models describe systems with realizable equilibrium configuration [100].

The dark halo model widely used in the calculations carried out in the WIMP direct detection approaches is the simple isothermal sphere that corresponds to a spherical infinite system with a flat rotational curve. The halo density profile is:

$$\rho_{DM}(r) = \frac{v_0^2}{4\pi G} \frac{1}{r^2} \quad (30)$$

corresponding to the following potential:

$$\Psi_0(r) = -\frac{v_0^2}{2} \log(r^2). \quad (31)$$

In this case, when a maximal halo density is considered, the WIMP velocity distribution is the Maxwell function:

$$f(v) = N \exp\left(-\frac{3v^2}{2v_{rms}^2}\right) \quad (32)$$

where N is the normalization constant. The mean square velocity results: $v_{r.m.s.}^2 = (3/2)v_0^2$; this relation descends from the hypothesis of an halo formed by particles in hydrostatic equilibrium with an isotropic velocity distribution. Despite the simplicity of this model has favoured its wide use in the calculation of expected rate of WIMP-nucleus interaction, it doesn't match with astrophysical observations regarding the sphericity of the halo and the absence of rotation, the flatness of the rotational curve and the isotropy of the dispersion tensor, and it presents unphysical behavior: the density profile, in fact, has a singularity in the origin and implies a total infinite mass of the halo unless introducing some cut-off at large radii.

In the ref. [11] the analysis of the first 4 DAMA/NaI annual cycles in a particular case for a SI coupled WIMP candidate has been extended by considering a large number of self-consistent galactic halo models, in which the variation of the velocity distribution function is originated from the change of the halo density profile or of the potential. The different models have been classified in 4 classes according to the symmetry properties of the density profile or of the gravitational potential and of the velocity distribution function. The same strategy has been followed to obtain the new cumulative results given later. The considered halo model classes correspond to: spherically symmetric matter density with isotropic velocity dispersion (A); spherically symmetric matter density with non-isotropic velocity dispersion (B); axisymmetric models (C); triaxial models (D). The models are summarized in Table 6 where, according to ref. [11], are identified by a label.

We will present briefly in the following these models since they will be considered in the new results on the quest for possible candidate particle given in the following subsections. For a detailed discussion refers to the ref. [11].

I. Spherical halo models with isotropic velocity dispersion (A)

The first class groups models with spherical density profile; for these models $\rho(\vec{r}) = \rho(r)$ and $f(\vec{v}) = f(v)$. The first type of model is a generalization of the spherical isothermal sphere in which a core radius R_c is introduced. The density profile becomes (model A1):

$$\rho_{DM}(r) = \frac{v_0^2}{4\pi G} \frac{3R_c^2 + r^2}{(R_c^2 + r^2)^2}, \quad (33)$$

with, in case of maximal halo, corresponding potential:

$$\Psi_0(r) = -\frac{v_0^2}{2} \log(R_c^2 + r^2). \quad (34)$$

In the limit $R_c \rightarrow 0$ the profile (30) and the potential (31) is obtained. These models are also named *logarithmic* because of the analytic form of the potential.

A second class of spherical models are defined by the following matter density profile (models A2 and A3):

$$\rho_{DM}(r) = \frac{\beta \Psi_a R_c^\beta}{4\pi G} \frac{3R_c^2 + r^2(1 - \beta)}{(R_c^2 + r^2)^{(\beta+4)/2}}, \quad (35)$$

Table 6: Summary of the consistent halo models considered in the analysis of ref. [11] and in the following. The labels in the first column identify the models. In the third column the values of the related considered parameters are reported [11]; Other choices are also possible as well as other halo models. In the last column references to the corresponding equations in the text are listed. The models of the Class C have also been considered including possible co-rotation and counter-rotation of the dark halo (see eq. (44).)

Class A: spherical ρ_{DM} , isotropic velocity dispersion			eq.
A0	Isothermal Sphere	$R_c = 5 \text{ kpc}$	(30)
A1	Evans' logarithmic [101]	$R_c = 16 \text{ kpc}$	(33)
A2	Evans' power-law [102]	$R_c = 2 \text{ kpc}, \beta = 0.7$	(35)
A3	Evans' power-law [102]	$R_c = 2 \text{ kpc}, \beta = -0.1$	(35)
A4	Jaffe [103]	$\alpha = 1, \beta = 4, \gamma = 2, a = 160 \text{ kpc}$	(37)
A5	NFW [104]	$\alpha = 1, \beta = 3, \gamma = 1, a = 20 \text{ kpc}$	(37)
A6	Moore et al. [105]	$\alpha = 1.5, \beta = 3, \gamma = 1.5, a = 28 \text{ kpc}$	(37)
A7	Kravtsov et al. [106]	$\alpha = 2, \beta = 3, \gamma = 0.4, a = 10 \text{ kpc}$	(37)
Class B: spherical ρ_{DM} , non-isotropic velocity dispersion (Osipkov–Merritt, $\beta_0 = 0.4$)			
B1	Evans' logarithmic	$R_c = 5 \text{ kpc}$	(33)(39)
B2	Evans' power-law	$R_c = 16 \text{ kpc}, \beta = 0.7$	(35)(39)
B3	Evans' power-law	$R_c = 2 \text{ kpc}, \beta = -0.1$	(35)(39)
B4	Jaffe	$\alpha = 1, \beta = 4, \gamma = 2, a = 160 \text{ kpc}$	(37)(39)
B5	NFW	$\alpha = 1, \beta = 3, \gamma = 1, a = 20 \text{ kpc}$	(37)(39)
B6	Moore et al.	$\alpha = 1.5, \beta = 3, \gamma = 1.5, a = 28 \text{ kpc}$	(37)(39)
B7	Kravtsov et al.	$\alpha = 2, \beta = 3, \gamma = 0.4, a = 10 \text{ kpc}$	(37)(39)
Class C: Axisymmetric ρ_{DM}			
C1	Evans' logarithmic	$R_c = 0, q = 1/\sqrt{2}$	(40)(41)
C2	Evans' logarithmic	$R_c = 5 \text{ kpc}, q = 1/\sqrt{2}$	(40)(41)
C3	Evans' power-law	$R_c = 16 \text{ kpc}, q = 0.95, \beta = 0.9$	(42)(43)
C4	Evans' power-law	$R_c = 2 \text{ kpc}, q = 1/\sqrt{2}, \beta = -0.1$	(42)(43)
Class D: Triaxial ρ_{DM} [107] ($q = 0.8, p = 0.9$)			
D1	Earth on maj. axis, rad. anis.	$\delta = -1.78$	(45)(46)
D2	Earth on maj. axis, tang. anis.	$\delta = 16$	(45)(46)
D3	Earth on interm. axis, rad. anis.	$\delta = -1.78$	(45)(46)
D4	Earth on interm. axis, tang. anis.	$\delta = 16$	(45)(46)

and potential for a maximal halo:

$$\Psi_0(r) = \frac{\Psi_a R_c^\beta}{(R_c^2 + r^2)^{\beta/2}} \quad (\beta \neq 0). \quad (36)$$

We will refer to these models as *power-law* halo models. They represent the spherical limit of the more general axisymmetric model discussed later. When the parameter $\beta \rightarrow 0$, the logarithmic models are obtained.

The last family of spherical models is described by the matter density distribution

(models *A4 – A7*):

$$\rho_{DM}(r) = \rho_0 \left(\frac{R_0}{r} \right)^\gamma \left[\frac{1 + (R_0/a)^\alpha}{1 + (r/a)^\alpha} \right]^{(\beta-\gamma)/\alpha}. \quad (37)$$

The different choice of the parameters: α, β, γ and a , used in the calculations given later are reported in Table 6; other choices are possible. The density profile of these models, except for the Jaffe case, has been obtained from numerical simulations of Galaxy evolution.

II. Spherical halo models with non-isotropic velocity dispersion (B)

These models have been studied in the simple case in which the velocity distribution function depends on the two integrals of motion energy and angular momentum vector ($L = |\vec{L}|$) only through the so called Osipkov-Merrit variable [100, 108]:

$$Q = \epsilon - \frac{L^2}{2r_a^2}, \quad (38)$$

where the parameter r_a appears in the definition of the β_0 , the degree of anisotropy of the velocity dispersion tensor on the Earth's position [108]:

$$\beta_0 = 1 - \frac{\overline{v_\phi}^2}{\overline{v_r}^2} = \frac{R_0^2}{R_0^2 + r_a^2}. \quad (39)$$

In this definition the velocity is expressed in spherical coordinates and $\overline{v_\phi} = \overline{v_\theta} \neq \overline{v_r}$ (con $\overline{v_i}^2 \equiv \langle v_i^2 \rangle - \langle v_i \rangle^2, i = \phi, \theta, r$).

The considered models are the same as in the isotropic case and the velocity distribution function has been calculated introducing the Osipkov-Merrit term in the equations. The degree of anisotropy of the models depends on the β_0 values; for $\beta_0 \rightarrow 1$, or $\overline{v_\phi}^2 = \overline{v_r}^2$, the distribution function becomes isotropic.

III. Axisymmetric models (C)

In these models the velocity distribution depends in general at least on the energy ϵ and on the component L_z of the angular momentum along the axis of symmetry. The velocity distribution can be written as the sum of an even and an odd contribution with respect to L_z . It can be shown [101, 102] that the ρ_{DM} depends only on the even part and the velocity distribution can be calculated up to an arbitrary odd part. The axisymmetric generalizations of the Evans' logarithmic and power-law models have been considered in ref. [11]. For these models the velocity distribution has been calculated analytically by Evans [101, 102] and corresponds to a maximal halo. The axisymmetric logarithmic potential (models *C1* and *C2*) is:

$$\Psi_0(R, z) = -\frac{v_0^2}{2} \log \left(R_c^2 + R^2 + \frac{z^2}{q^2} \right), \quad (40)$$

where $R = (x^2 + y^2)$, is the radial coordinate along the galactic plane and R_c is the core radius; q is the flatness parameter. The corresponding matter density distribution results:

$$\rho_{DM}(R, z) = \frac{v_0^2}{4\pi G q^2} \frac{(2q^2 + 1)R_c^2 + R^2 + (2 - q^{-2})z^2}{(R_c^2 + R^2 + z^2 q^{-2})^2}. \quad (41)$$

If an asymptotically non-flat rotational curve is considered, the axisymmetric power-law potential is obtained [102] (models *C3* and *C4*):

$$\Psi_0(R, z) = \frac{\Psi_a R_c^\beta}{(R_c^2 + R^2 + z^2 q^{-2})^{\beta/2}} \quad (\beta \neq 0). \quad (42)$$

with the distribution function:

$$\rho_{DM}(R, z) = \frac{\beta \Psi_a R_c^\beta}{4\pi G q^2} \frac{(2q^2 + 1)R_c^2 + (1 - \beta q^2)R^2 + [2 - q^{-2}(1 + \beta)]z^2}{(R_c^2 + R^2 + z^2 q^{-2})^{(\beta+4)/2}}. \quad (43)$$

The related velocity distribution functions for these two cases can be found in ref. [11].

IV. Co-rotating and counter-rotating halo models

In the case of axisymmetric models it is possible to include an halo rotation considering that the velocity distribution function is known up to an arbitrary odd component. An odd component of velocity distribution function can easily be defined starting from an even solution. The velocity distribution function, linear combination of even and odd function, is able to describe an halo configuration where a particle population moves clockwise around the axis of symmetry and a population moves in opposite sense. In this case the velocity distribution can be written as [11]:

$$F(\epsilon, L_z) = \eta F_{right}(\epsilon, L_z) + (1 - \eta) F_{left}(\epsilon, L_z). \quad (44)$$

The η parameter ranges from 1 (maximal co-rotation) to 0 (maximal counter-rotation) and it is related to the dimensionless spin parameter λ of the Galaxy by: $\lambda = 0.36|\eta - 0.5|$ [109].

Considering the limit $\lambda < 0.05$ obtained from numerical work on Galaxy formation [110], η can range in the interval $0.36 \lesssim \eta \lesssim 0.64$. For the Evans' axisymmetric models of class C we have also considered possible co-rotation and counter-rotation of the halo assuming $\eta = 0.36$ and $\eta = 0.64$.

V. Triaxial models (D)

The models, belonging to this class, arise from the triaxial potential discussed in ref. [107]:

$$\Psi_0(x, y, z) = -\frac{1}{2} v_0^2 \log \left(x^2 + \frac{y^2}{p^2} + \frac{z^2}{q^2} \right), \quad (45)$$

This potential, in the case of a maximal halo, corresponds to the density profile:

$$\rho_{DM}(x, y, z) = \frac{v_0^2}{4\pi G} \frac{Ax^2 + By^2/p^2 + Cz^2/q^2}{(x^2 + y^2/p^2 + z^2/q^2)^2}, \quad (46)$$

where $A = (p^{-2} + q^{-2} - 1)$, $B = (1 + q^{-2} - p^{-2})$ and $C = (1 + p^{-2} - q^{-2})$. In ref.[107], the velocity distribution is approximated by a Gaussian with \bar{v}_r^2 , \bar{v}_θ^2 , \bar{v}_ϕ^2 depending on v_0 , δ , p and q parameters an on the Earth position: i) Earth on the major axis of

the equipotential ellipsoid (models $D1$ and $D2$); ii) Earth on the intermediate axis (Models $D3$ and $D4$). In these cases the free parameter δ appears; this parameter, in the limit of spherical halo ($p = q = 1$), measures the degree of anisotropy of the velocity dispersion tensor: $\frac{\bar{v}_\phi^2}{\bar{v}_r^2} = \frac{2+\delta}{2}$.

VI. Constraining the models

The parameters of each halo model, given above, have been chosen in ref. [11] taking into account the available observational data. Anyhow, information on galactic dark halo can be obtained only in indirect way [111, 112] and considering hypotheses on its form and characteristic.

The allowed range of values for the WIMP local velocity has been estimated there considering the information coming from the rotational curve of our Galaxy. The considered interval is:

$$v_0 = (220 \pm 50) \text{ km s}^{-1} \quad (90\% \text{ C.L.}), \quad (47)$$

that conservatively relies on purely dynamical observations [113]. Similar estimates of the v_0 central value with smaller uncertainty have been obtained studying the proper motion of nearby stars in the hypothesis of circular orbit of these objects [114]. In the analyses given in the following, for simplicity, we have considered the three representative values of local velocity: $v_0 = 170, 220, 270 \text{ km/s}$.

Table 7: Allowed intervals of ρ_0 for the halo models quoted in Table 6 as evaluated in ref. [11]. The ρ_0^{max} and ρ_0^{min} values (in GeV cm^{-3}) are here used in the quests for a candidate particle (see later) for the class A and B , while only the case of ρ_0^{max} is used for the class C and D .

Model	$v_0 = 170 \text{ km s}^{-1}$		$v_0 = 220 \text{ km s}^{-1}$		$v_0 = 270 \text{ km s}^{-1}$	
	ρ_0^{min}	ρ_0^{max}	ρ_0^{min}	ρ_0^{max}	ρ_0^{min}	ρ_0^{max}
A0	0.18	0.28	0.30	0.47	0.45	0.71
A1 , B1	0.20	0.42	0.34	0.71	0.62	1.07
A2 , B2	0.24	0.53	0.41	0.89	0.97	1.33
A3 , B3	0.17	0.35	0.29	0.59	0.52	0.88
A4 , B4	0.26	0.27	0.44	0.45	0.66	0.67
A5 , B5	0.20	0.44	0.33	0.74	0.66	1.11
A6 , B6	0.22	0.39	0.37	0.65	0.57	0.98
A7 , B7	0.32	0.54	0.54	0.91	0.82	1.37
C1	0.36	0.56	0.60	0.94	0.91	1.42
C2	0.34	0.67	0.56	1.11	0.98	1.68
C3	0.30	0.66	0.50	1.10	0.97	1.66
C4	0.32	0.65	0.54	1.09	0.96	1.64
D1 , D2	0.32	0.50	0.54	0.84	0.81	1.27
D3 , D4	0.19	0.30	0.32	0.51	0.49	0.76

Moreover, in the analyses given in the following, for each model – after fixing the local velocity – the local density ρ_0 has been assumed to be equal either to the ρ_0^{\min} or to the ρ_0^{\max} value as obtained in ref. [11] when imposing the following physical constraints: i) the amount of flatness of the rotational curve of our Galaxy, considering conservatively $0.8 \cdot v_0 \lesssim v_{\text{rot}}^{100} \lesssim 1.2 \cdot v_0$, where v_{rot}^{100} is the value of rotational curve at distance of 100 kpc from the galactic center; ii) the maximal non dark halo components in the Galaxy, considering conservatively $1 \cdot 10^{10} M_{\odot} \lesssim M_{\text{vis}} \lesssim 6 \cdot 10^{10} M_{\odot}$ [111, 112]. In particular, the allowed intervals for ρ_0 are reported in Table 7. For the models of class C and D, as discussed before, only the case of maximal halo (which correspond to $M_{\text{vis}} = 0$) has been considered in the analyses discussed in the following.

7.1.4 The form factors

In order to take into account the finite dimension of the nucleus in the scattering processes, it is necessary to introduce the nuclear form factor, F , that generally also depends on the nature of the interaction.

In the case of SI interactions, we can factorize the total cross section, pointing out the contribution given by the form factor:

$$\sigma(q) = \sigma_{SI} F_{SI}^2(q), \quad (48)$$

here σ_{SI} is the total cross section when the transfer momentum q is 0. When neglecting possible neutron and proton differences, the nuclear form factor can be reasonably described by the Fourier transform of charge density $\rho(r)$ in the nucleus:

$$F_{SI}(q) = \frac{1}{A} \int \rho(r) e^{i\vec{q} \cdot \vec{r}} d^3 r = \frac{1}{A} \frac{4\pi}{q} \int_0^\infty r \sin(qr) \rho(r) dr. \quad (49)$$

In the theoretical calculations and data analysis DAMA/NaI has adopted, for the SI form factor, the expression suggested by Helm in [115]:

$$F_{SI}(q) = \frac{3j_1(qr_0)}{qr_0} \exp\left[-\frac{1}{2}s^2 q^2\right], \quad (50)$$

where $r_0 = \sqrt{r_n^2 - 5s^2}$, r_n is the effective nuclear radius, $s \simeq 1$ fm is a parameter that allows to take into account the thickness of the nuclear surface and $j_1(qr_0)$ is the spherical Bessel function of index 1. We remind that this expression of SI form factor is derived assuming a Fermi distribution for the nuclear charge.

In Fig. 23 on the right, the effect of a relatively small variation (20%) of the nuclear radius, r_n , and the nuclear surface thickness parameter, s , in the Helm SI form factor is shown; as it can be seen, even a relative small variation of these parameters can produce sizeable change in the behaviour of the form factor and, therefore, in the expected SI signal rate and in the final result.

In addition, also other expressions have been considered in literature for the SI nuclear form factors of the various nuclei. Just as an example, in Fig. 23 on the left, SI form factors discussed e.g. in ref. [116] are depicted for the Iodine nucleus; the continuous line represents the nuclear form factor obtained when using expression (50) at the fixed assumed values for the related parameters.

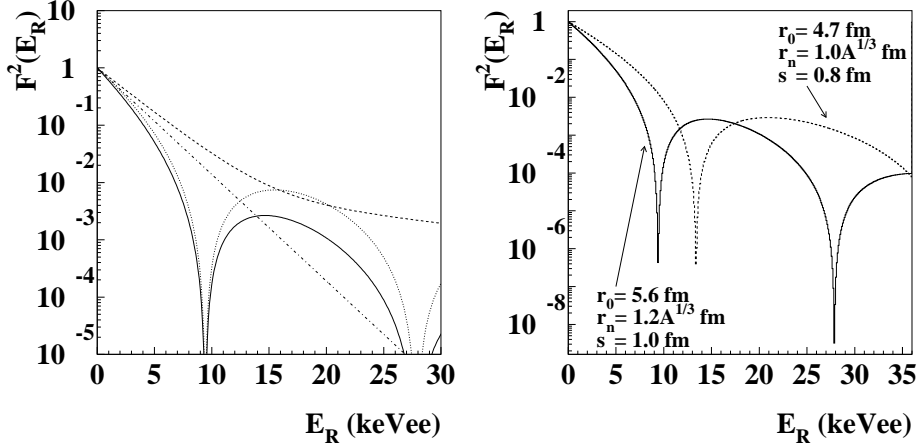


Figure 23: Left panel: some SI nuclear form factors considered so far in the literature (e.g. in ref. [116]) calculated for the Iodine nucleus. Right panel: example of the variation of the SI nuclear form factor, calculated according to ref. [115], when some uncertainties on its parameters are considered; as it can be seen, even a relative small variation can produce sizeable change in the behaviour of the nuclear form factor and, therefore, in the expected SI signal rate. Note that here the notation keVee is explicitly mentioned in the panels to indicate keV electron equivalent in order to remind that the recoil energy has been quenched there by using the quenching factor value measured by DAMA in ref. [46].

As mentioned, in the analyses given in the following the most cautious Helm SI form factor has been adopted taking into account some uncertainties on the nuclear radius and on the nuclear surface thickness parameters. As it can be seen, this form factor is the less favourable one for Iodine and requires larger SI cross sections for a given signal rate. For example, in case the other form factor profiles considered in literature would be used, the allowed regions given in the following sections would extend to lower cross sections.

In the case of SD interactions an analytical universal expression for the form factor does not exist. In fact, in this case, the internal degrees of the WIMP particle model (e.g. supersymmetry in the case of neutralino) cannot be completely decoupled from the nuclear ones. Therefore, in order to take into account the property of the nucleus interested in the interaction, we have to refer not only to a particular nuclear model but also to a particular particle physics model. As an example, if we consider the case of the neutralino in the MSSM model, the differential SD cross section can be written from eq. (8):

$$\left(\frac{d\sigma}{dE_R} \right)_{SD} = \frac{16G_F^2}{\pi v^2} m_N \Lambda^2 J(J+1) F_{SD}^2(E_R), \quad (51)$$

where $F_{SD}(E_R)$ is the SD nuclear form factor defined (see e.g. ref. [117]) as

$F_{SD}^2(E_R) = S(q)/S(0)$ with $\pi S(0) = (2J+1)\Lambda^2 J(J+1)$ and:

$$S(q) = a_0^2 S_{00}(q) + a_1^2 S_{11}(q) + a_0 a_1 S_{01}(q), \quad (52)$$

with $a_0 = a_p + a_n$ and $a_1 = a_p - a_n$, where a_p and a_n are the effective neutralino-nucleon SD coupling strengths defined in §7.1.1. The functions $S_{ij}(q)$ generally depend on the considered nuclear model. For nuclei of interest for Dark Matter detection, (as the ^{127}I and ^{23}Na), the $S_{ij}(q)$ have been parameterized in ref. [117] as function of the variable $y = (qb/2)^2$ (where b is a parameter of the theoretical model, $b \simeq A^{1/6}$ fm):

$$S_{ij}(q) = e^{-2y} \sum_{l=0}^8 C_l y^l, \quad (53)$$

where the coefficients C_l generally depend on the adopted nucleon-nucleon potential. For the ^{23}Na nucleus only the first three orders of the previous expression have been considered in ref. [117], while for the ^{127}I nucleus two different nuclear potentials (the Nijmegen II and the Bonn-A ones) have been used in the evaluation of ref. [117].

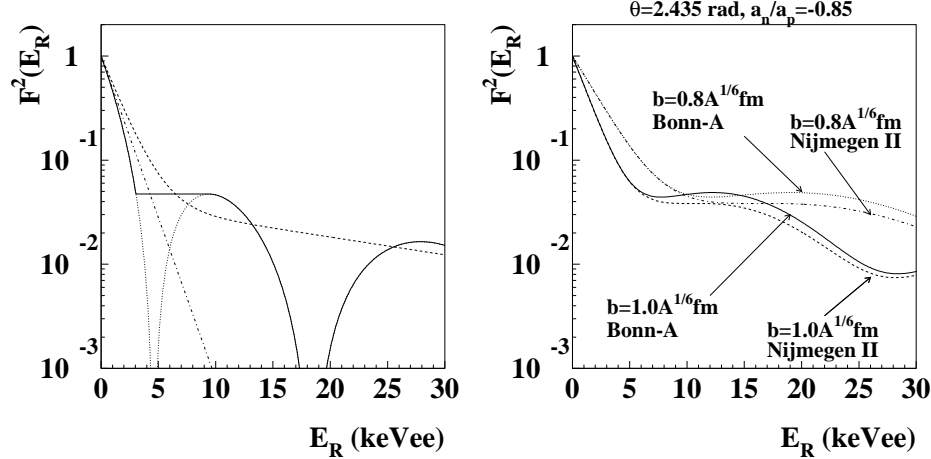


Figure 24: Left panel: some SD nuclear form factors considered so far in the literature (e.g. in ref. [116]) calculated for the Iodine nucleus. Right panel: example of variation of the Iodine SD nuclear form factor, calculated according to ref. [117] for two different choices of the nucleon-nucleon potential and including also a possible small variation (20%) of its b parameter. As it can be seen, even a relative small variation either of this parameter or of the nuclear potential can produce sizeable change in the behaviour of the nuclear form factor and, therefore, in the expected SD signal rate. Note that here the notation keVee is explicitly mentioned in the panels to indicate keV electron equivalent in order to remind that the recoil energy has been quenched there by using the quenching factor value measured by DAMA in ref. [46].

It is worth to note that the SD form factor depends on the nature of the interacting WIMP and on the nuclear potential. Therefore, the SD form factor is an important source of uncertainties in the calculation of the expected rate. As an example, in Fig. 24 on the right the effect of the different choice of the nucleon-nucleon potential

and of a relatively small variation (20%) of the b parameter in the Iodine SD nuclear form factor, calculated according to ref. [117], is shown (we report here, for simplicity, only the case with $\theta = 2.435$ or $a_n/a_p = -0.85$, that is pure Z_0 coupling). Similar uncertainties are present for every nucleus.

There are other expressions considered in literature for the SD nuclear form factor; they can be very different. Just as an example Fig. 24 on the left shows some SD form factors discussed e.g. in ref. [116] calculated for the Iodine nucleus.

In the analyses, presented in the following, the SD form factors in the neutralino case for Sodium and Iodine nuclei calculated by [117] using – for the Iodine case – the nuclear potential by Nijmegen II have been adopted. Analogously, as for the SI case, here uncertainties on the b parameter have been included in the evaluations of the results.

For the sake of completeness, let us remind that typically only purely SI or purely SD Z_0 coupling WIMP interactions are considered in the evaluations of the results in this field among all the wide available possibilities and that the uncertainty on the form factors also largely affects comparisons among results obtained by using different target nuclei.

7.1.5 The spin factors

Further significant uncertainties in the evaluation of the SD interaction rate arise also from the adopted spin factor for the single target-nucleus [117, 118]. As an example, the spin factors of some target-nuclei calculated in different models are reported in Table 8. Moreover, also for a fixed nuclear model, differences arise from the use – in the calculations – of different nuclear potentials as it is e.g. the case of the ^{129}Xe and of the ^{127}I nuclei, for which similar calculations are already available.

As it can be noted in Table 8, since the spin factor is a multiplicative factor in the expected SD signal rate, its value can also drastically affect the expectations in direct search experiments and, therefore, also the inferred exclusion plots or allowed regions can largely vary as well as the results of any comparison.

Moreover, for a complete analysis of a SD component it is worth to remind that θ (whose tangent is the ratio between the SD WIMP-neutron and SD WIMP-proton effective strengths; see §7.1.1), can continuously assume values in the range 0 to π . For example, in Table 9 spin factors calculated on the basis of ref. [117] are given for some θ values considering few target nuclei and two different nuclear potentials.

In conclusion, not only large differences in the rate can be expected when using target nuclei sensitive to the SD component of the interaction (such as e.g. ^{23}Na and ^{127}I) with respect to those largely insensitive to such a coupling (such as e.g. ^{nat}Ge and ^{nat}Si), but also when using different target nuclei although all – in principle – sensitive to such a coupling (compare e.g. the Xenon and Tellurium case with the Sodium and Iodine case in Table 9).

Moreover, other nuclear models and calculations beyond those reported here are possible, introducing large uncertainties in the right estimate of the used spin factor for each given target-nucleus.

Table 8: Some spin factors estimates assuming simple different models. The values given in this Table are $\Lambda^2 J(J+1)/a_x^2$, where a_x is either a_p or a_n depending on the unpaired nucleon.

Target-Nucleus	single particle	odd group	Comment
^{29}Si	0.750	0.063	
^{73}Ge	0.306	0.065	
^{129}Xe	0.750	0.124	
^{131}Xe	0.150	0.055	
^1H	0.750	0.750	
^{19}F	0.750	0.647	
^{23}Na	0.350	0.041	
^{27}Al	0.350	0.087	
^{69}Ga	0.417	0.021	
^{71}Ga	0.417	0.089	
^{75}As	0.417	0.000	
^{127}I	0.250	0.023	

Table 9: Spin factors calculated on the basis of ref. [117] for some of the possible θ values considering some target nuclei and two different nuclear potentials. The values given in this Table are $\Lambda^2 J(J+1)/\bar{a}^2$, where \bar{a}^2 has been defined in §7.1.1.

Target-Nucleus / nuclear potential	$\theta=0$	$\theta=\pi/4$	$\theta=\pi/2$	$\theta=2.435$ (pure Z_0 coupling)
^{23}Na	0.102	0.060	0.001	0.051
$^{127}\text{I}/\text{Bonn A}$	0.134	0.103	0.008	0.049
$^{127}\text{I}/\text{Nijmegen II}$	0.175	0.122	0.006	0.073
$^{129}\text{Xe}/\text{Bonn A}$	0.002	0.225	0.387	0.135
$^{129}\text{Xe}/\text{Nijmegen II}$	0.001	0.145	0.270	0.103
$^{131}\text{Xe}/\text{Bonn A}$	0.000	0.046	0.086	0.033
$^{131}\text{Xe}/\text{Nijmegen II}$	0.000	0.044	0.078	0.029
$^{125}\text{Te}/\text{Bonn A}$	0.000	0.124	0.247	0.103
$^{125}\text{Te}/\text{Nijmegen II}$	0.000	0.156	0.313	0.132

7.1.6 The quenching factors

The proper knowledge of other quantities is also necessary for a WIMP direct search such as e.g. the recoil/electron response ratio for the given nucleus in the given detector (named *quenching factor*, q). The recoil/electron response ratio can be measured with a neutron source or at a neutron generator (see as an example ref. [72]). In

the latter case a set-up similar to that reported in Fig. 25 can be used on a quasi-monochromatic neutron beam tagging the scattered neutrons. Let us comment that

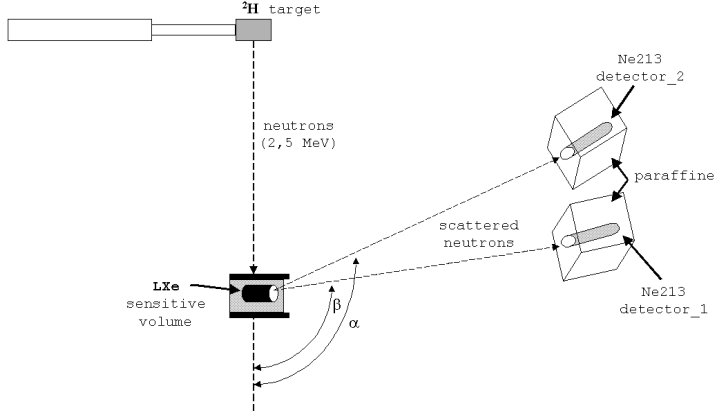


Figure 25: Example of a set-up for the measurement of the recoil/electron response ratio of a detector. This example is taken from ref. [72].

while this configuration works out well for the measurements of recoil/electron response ratio, it is unsuitable to determine the absolute detection efficiency for recoils because of the uncertain knowledge of the elastic cross sections, of the background due to inelastic scatterings, of the electromagnetic and hadronic background from neutron interaction in the environment, of the cuts for noise rejection in a very high rate environment, of the duty cycle (which is very small), etc.

Of course, significant differences are often present in literature for the measured value of this recoil /electron response ratio for the same nucleus in similar detectors as it can be clearly deduced from Table 10, where the quenching factors measured for the detectors most commonly used in this field are reported. As it can be seen, significant differences in the measured values are present also for the same nucleus in the same kind of detectors. This is generally due to different peculiarities of the detectors themselves, besides possible additional experimental uncertainties. For example, in doped scintillator it can depend on the dopant concentration, in liquid Xenon on the residual trace contaminants due to specific experimental features (such as the initial purity of the used Xenon gas, the inner surface treatment, the level of vacuum reached before filling, the used purification line components and the degassing/release features of all the materials of the inner vessel) and in Ge or Si on impurities, etc. Moreover, some dependence of the recoil /electron response ratio on the energy has been quoted in several cases (see Table 10).

As far as regards the bolometers, no direct measurement of the recoil energy of the target-nucleus has been reported up to now by any of the groups involved in this activity, although several bolometers have been irradiated with neutrons along the past

Table 10: Quenching factor, q , values measured by using neutron sources or neutron beams for some detectors and nuclei. When a significant q dependence on the energy has been explicitly given, only the maximum and the minimum central values are reported for the given energy interval without quoting here – for simplicity – the associated errors.

Nucleus/Detector	Recoil Energy (keV)	q	Reference
NaI(Tl)	(6.5-97)	(0.30 ± 0.01) for Na	[46]
	(22-330)	(0.09 ± 0.01) for I	[46]
	(20-80)	(0.25 ± 0.03) for Na	[119]
	(40-100)	(0.08 ± 0.02) for I	[119]
	(4-252)	(0.275 ± 0.018) for Na	[120]
	(10-71)	(0.086 ± 0.007) for I	[120]
	(5-100)	(0.4 ± 0.2) for Na	[121]
	(40-300)	(0.05 ± 0.02) for I	[121]
CaF ₂ (Eu)	(30-100)	(0.06-0.11) for Ca	[120]
	(10-100)	(0.08-0.17) for F	[120]
	(90-130)	(0.049 ± 0.005) for Ca	[45]
	(75-270)	(0.069 ± 0.005) for F	[45]
	(53-192)	(0.11-0.20) for F	[122]
	(25-91)	(0.09-0.23) for Ca	[122]
CsI(Tl)	(25-150)	(0.15-0.07)	[123]
	(10-65)	(0.17-0.12)	[124]
	(10-65)	(0.22-0.12)	[125]
CsI(Na)	(10-40)	(0.10-0.07)	[125]
Ge	(3-18)	(0.29-0.23)	[126]
	(21-50)	(0.14-0.24)	[127]
	(10-80)	(0.18-0.34)	[128]
	(20-70)	(0.24-0.33)	[129]
Si	(5-22)	(0.23-0.42)	[130]
	22	(0.32 ± 0.10)	[131]
Liquid Xe	(30-70)	(0.46 ± 0.10)	[72]
	(40-70)	(0.18 ± 0.03)	[132]
	(40-70)	(0.22 ± 0.01)	[133]
Bolometers	-	none available at time of writing this paper (assumed 1)	

decade. For the sake of completeness, we remind that a measurement of the response of a TeO₂ bolometer to surface ²²⁴Ra recoiling nuclei has been reported in ref. [134]; this measurement, although its importance, does not represent a determination of the quenching factor of the target- (either Te or O) nuclei of the TeO₂ bolometer. In fact,

the recoiling nuclei are not the Te and O ones and the “external” recoils are generated on the detector surface where the sensors are located and, thus, do not involve the response of the whole bulk of the target-detector. Anyhow, these values cannot of course be extended to whatever kind of bolometer.

7.1.7 Some miscellaneous

Besides the uncertainties already discussed, there exist a large number of experimental details that have to be considered in the calculations of the signal expectations. For example, it must be suitably studied, checked, monitored and discussed the role played by the stability of the energy scale, by its right evaluation (see also §7.1.6), by a reliable identification of the energy threshold and of the residual noise above it (as it can be effectively done in NaI(Tl) detectors with adequate number of photoelectrons/keV, see e.g. [41]), by external veto (especially when “high” rate anticoincidences are used) and by the rejection procedures used in some experiments to filter the data, etc.. In the case of DAMA/NaI details have been given along the last about ten years and published (see e.g. [41, 61, 63, 64]).

Finally, let us remind that – when results obtained by using different target nuclei are considered – also the effect of the uncertainty on the scaling laws of the nuclear cross sections to the *reference* ones (e.g., generally, on nucleon) must be taken into account. In fact, it is common practice to use the WIMP-nucleon cross sections σ_{SI} and σ_{SD} and the scaling laws reported in §7.1.1; but – in principle – other scaling laws cannot be excluded at the present knowledge of the real nature of a WIMP candidate. This can be an additional uncertainty in quests for a candidate and in comparisons among experiments using different target nuclei.

7.1.8 Priors

It is common practice in extracting physical information from the data to account for related priors.

In particular, in the quest for the candidate particle two main priors have been considered in the DAMA/NaI first quests for a candidate [60, 61, 62, 63, 65, 66, 11].

The first prior, which has been properly included in ref. [63, 65, 66, 11] and also considered in the following, accounts for the upper limits measured on the recoil fractions in the data of the DAMA/NaI-0 running period [46, 64], which was carefully and especially devoted to such an investigation.

The second prior regards the mass limit for supersymmetric candidates, achieved – within some assumed model frameworks – by experiments at accelerators. In particular, because of this prior, WIMP masses above 30 GeV (25 GeV in ref. [60]) have been investigated in refs. [61, 63, 65, 66, 11] for few (of the many possible) model frameworks. Specifically, it accounted for the lower bound on the neutralino mass as derived from the LEP data in the adopted supersymmetric schemes based on GUT assumptions [78]. However, other model assumptions are possible and would imply significant variations of some accelerators bounds. As an example, we mention the recent ref. [135] where the assumption on the gaugino-mass unification at GUT scale

has been released ¹³. The development of these schemes is very interesting since – as well known – DAMA/NaI is intrinsically sensitive both to low and high WIMP mass having both a light (the ^{23}Na) and a heavy (the ^{127}I) target-nucleus.

However, still following the present model dependent results quoted by LEP in the supersymmetric schemes based on GUT assumptions the considered lower bound is at present 37 GeV [138] ¹⁴. It is worth to note that this mass limit selects the WIMP-Iodine elastic scattering as dominant because of the adopted scaling laws and of kinematical arguments.

7.2 Results on the quest for a candidate in some of the possible model frameworks

Just as a corollary of the model independent result given in §6.1, in the following some of the many possible model dependent quests for a WIMP candidate is carried out using the data collected during all the seven annual cycles and considering all the halo models summarized in §7.1.3 for three of the possible values of the local velocity v_0 : 170 km/s, 220 km/s and 270 km/s. The used halo density follows the prescriptions of §7.1.3.VI. The escape velocity has been maintained at the fixed value: 650 km/s; of course, it is worth to note that the present existing uncertainties affecting the knowledge of the escape velocity will significantly extend allowed regions e.g. in the cases of *preferred inelastic* WIMPs and of light mass WIMP candidates; its effect would be instead marginal at large WIMP masses (see e.g. the case for exclusion plots given in Fig. 3).

In particular, possible scenarios have been exploited for the halo models described in §7.1.3 in some discrete cases either considering the mean values of the parameters of the used nuclear form factors and of the measured quenching factors (case *A*) or adopting the same procedure as in refs. [65, 66] ¹⁵ (case *B*) or in one of the possible more extreme cases where the Iodine nucleus parameters are fixed at the values of case *B*, while for the Sodium nucleus one considers: i) ^{23}Na quenching factor at the lowest value measured in literature (see Table 10); ii) the nuclear radius, r_n , and the nuclear surface thickness parameter, s , in the SI Form Factor [115] from their central values up to +20%; iii) the b parameter in the considered SD form factor from the given value [117] up to +20% (case *C*).

In the following sections, for simplicity, the results of these corollary quests for a candidate particle is presented in terms of allowed regions obtained as superposition of the configurations corresponding to likelihood function values *distant* more than 4σ from the null hypothesis (absence of modulation) in each of the several (but still a

¹³In this case also neutralino masses down to $\simeq 6$ GeV are possible, this lower bound being determined by current upper limit on relic abundance for cold dark matter (somewhat higher values of 15–18 GeV are obtained for the neutralino mass lower bound, if Higgs masses are assumed large (1 TeV) [136, 137].

¹⁴Higher limits are available for other more constrained models. These latter ones as well as possible future increase of the present 37 GeV lower bound would further select - for these scenarios - the possible models in the quest for the candidate from the DAMA/NaI data favouring, in particular, halo models with small local velocity and/or co-rotation.

¹⁵that is, by varying either: i) the mean values of the measured ^{23}Na and ^{127}I quenching factors [46] up to +2 times the errors; ii) the nuclear radius, r_n , and the nuclear surface thickness parameter, s , in the SI Form Factor [115] from their central values down to -20%; iii) the b parameter in the considered SD form factor from the given value [117] down to -20%.

limited number) of the possible model frameworks considered here. Priors have been discussed in §7.1.8.

Obviously, larger sensitivities than those reported in the following would be reached when including the effect of other existing uncertainties on assumptions and related parameters, as it can be also inferred from the previous sections.

7.2.1 WIMPs with mixed SI&SD interaction in some of the possible model frameworks

The most general scenario of WIMP nucleus elastic interaction, to which the DAMA/NaI target nuclei are fully sensitive, is the one where both the SI and the SD components of the cross section (see §7.1.1) are present. Thus, as first we introduce here the case for a candidate with both SI and SD couplings to ordinary matter similarly as in ref. [65].

As already described in §7.1.1, in this most general scenario the space of the free parameters is a 4-dimensional volume defined by m_W , $\xi\sigma_{SI}$, $\xi\sigma_{SD}$ and θ (which varies from 0 to π). Thus, the general solution would be a four dimensional allowed volume for each considered model framework. Since the graphic representation of this allowed volume is quite difficult, we show in Fig. 26 the obtained regions in the plane $\xi\sigma_{SI}$ vs $\xi\sigma_{SD}$ for some of the possible θ and m_W values in the model frameworks considered here. In particular, we report just four couplings, which correspond to the following values of the mixing angle θ : i) $\theta = 0$ ($a_n = 0$ and $a_p \neq 0$ or $|a_p| >> |a_n|$) corresponding to a particle with null SD coupling to neutron; ii) $\theta = \pi/4$ ($a_p = a_n$) corresponding to a particle with the same SD coupling to neutron and proton; iii) $\theta = \pi/2$ ($a_n \neq 0$ and $a_p = 0$ or $|a_n| >> |a_p|$) corresponding to a particle with null SD couplings to proton; iv) $\theta = 2.435$ rad ($\frac{a_n}{a_p} = -0.85$) corresponding to a particle with SD coupling through Z_0 exchange. The case $a_p = -a_n$ is nearly similar to the case iv).

To offer an example of how the allowed regions have been built, Fig. 27 shows explicitly the superposition of the slices obtained for each one of the model frameworks considered here in the particular case of $m_W = 90$ GeV and $\theta = 2.435$ (pure Z_0 coupling).

From the given figures it is clear that at present either a purely SI or a purely SD or a mixed SI&SD configurations are supported by the experimental data of the seven annual cycles.

Some other comments related to the effect of a SD component different from zero will be also addressed in the following.

7.2.2 WIMPs with dominant SI interaction in some of the possible model frameworks

Generally, mainly the case of purely spin-independent coupled WIMP is considered in literature. In fact, often the spin-independent interaction with ordinary matter is assumed to be dominant since e.g. most of the used target-nuclei are practically not sensitive to SD interactions (as on the contrary ^{23}Na and ^{127}I are) and the theoretical calculations are even much more complex and uncertain.

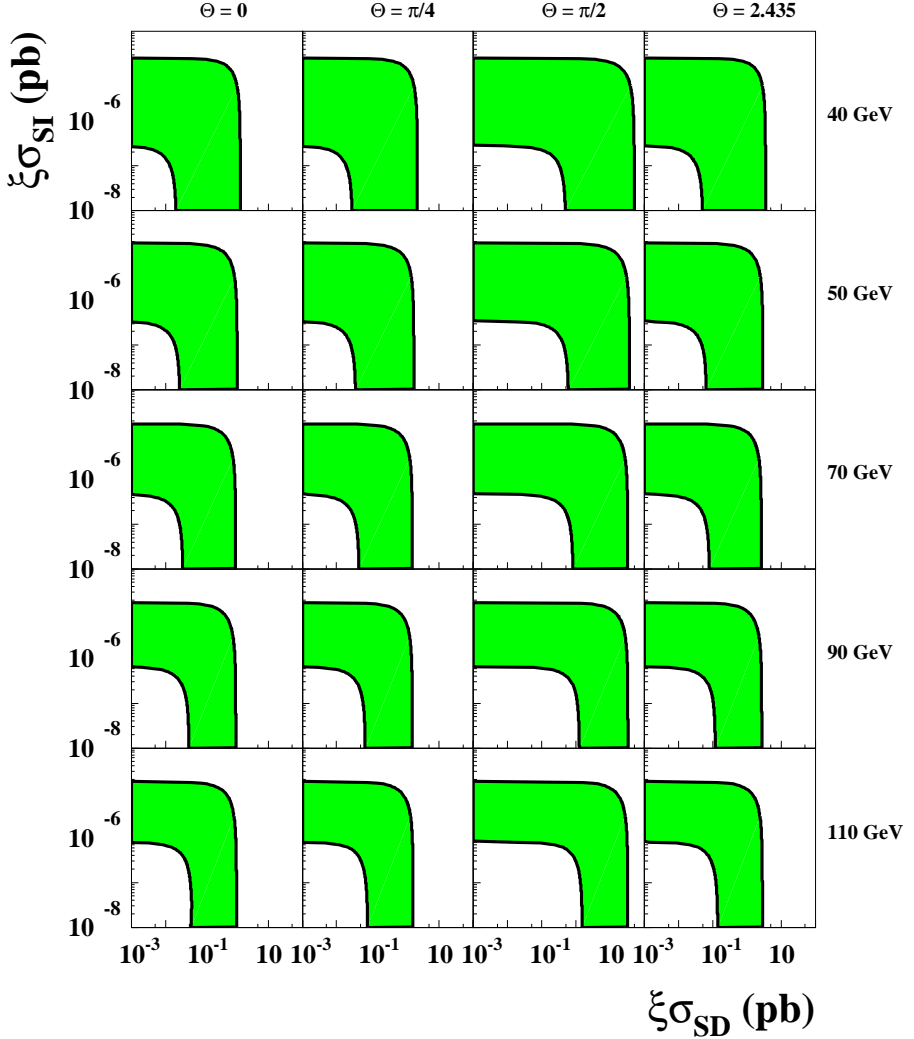


Figure 26: *A case of a WIMP with mixed SI&SD interaction in the model frameworks given in the text.* Colored areas: example of slices (of the allowed volume) in the plane $\xi\sigma_{SI}$ vs $\xi\sigma_{SD}$ for some of the possible m_W and θ values. See §7.2. Inclusion of other existing uncertainties on parameters and models (as previously discussed to some extent in this paper) would further extend the regions; for example, the use of more favourable form factors than those we considered here (see §7.1.4) alone would move them towards lower cross sections.

Thus, following an analogous procedure as for the previous case, we have exploited for the same model frameworks the purely SI scenario alone. In this case the free parameters are two: m_W and $\xi\sigma_{SI}$.

In Fig. 28 the region allowed in the plane m_W and $\xi\sigma_{SI}$ for the considered model frameworks is reported. The vertical dotted line represents the model dependent prior discussed in §7.1.8, that is the present lower bound on supersymmetric candidate as

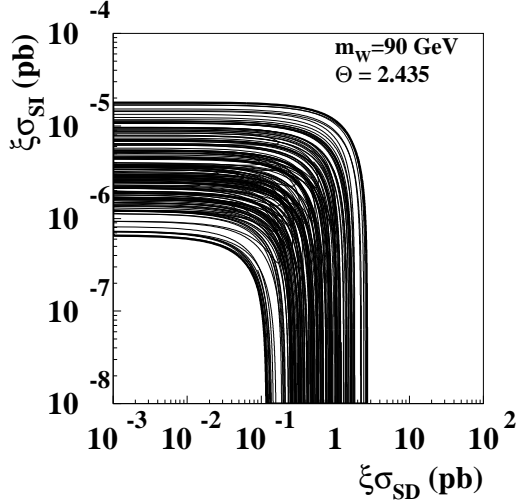


Figure 27: This figure explicitly shows all the slices (of the allowed volume) in the plane $\xi\sigma_{SI}$ vs $\xi\sigma_{SD}$ obtained for $m_W = 90$ GeV and $\theta = 2.435$ (pure Z_0 coupling) for each one of the considered model frameworks (see §7.2). The region included in between the two extreme lines is that shown for the same m_W and θ values in Fig. 26 (see also the related caption).

derived from the LEP data in supersymmetric scheme with gaugino-mass unification at GUT (see §7.1.8). The configurations below the vertical line can be of interest for neutralino when other schemes are considered (see §7.1.8) and for generic WIMP candidate. As shown in Fig. 28, also WIMP masses above 200 GeV are allowed, in particular, for every set of parameters' values when considering low local velocity and: i) the Evans' logarithmic $C1$ and $C2$ co-rotating halo models; ii) the triaxial $D2$ and $D4$ non-rotating halo models; iii) the Evans power-law $B3$ model, but only with parameters as in set A).

Of course, best fit values of cross section and WIMP mass span over a large range depending on the model framework. Just as an example, in the triaxial $D2$ halo model with maximal ρ_0 , $v_0 = 170$ km/s and parameters as in the case C , the best fit values are $m_W = (74^{+17}_{-12})$ GeV and $\xi\sigma_{SI} = (2.6 \pm 0.4) \cdot 10^{-6}$ pb.

Effect of a SD component different from zero on allowed SI regions

Let us now point out, in addition, that configurations with $\xi\sigma_{SI}$ even much lower than those shown in Fig. 28 would be accessible also if an even small SD contribution would be present in the interaction as described in §7.2.1. This possibility is clearly pointed out in Fig. 29 where an example of regions in the plane $(m_W, \xi\sigma_{SI})$ corresponding to different SD contributions are reported for the case $\theta = 0$. In this example the Evans' logarithmic axisymmetric $C2$ halo model with $v_0 = 170$ km/s, ρ_0 equal to the maximum value for this model (see Table 7) and the set of parameters A have been considered. The values of $\xi\sigma_{SD}$ range there from 0 to 0.08 pb. As it can be seen, increasing the SD contribution the regions allowed in the $(m_W, \xi\sigma_{SI})$ plane involve SI cross sections much lower than 1×10^{-6} pb. It can be noted that for $\sigma_{SD} \geq 0.08$ pb the

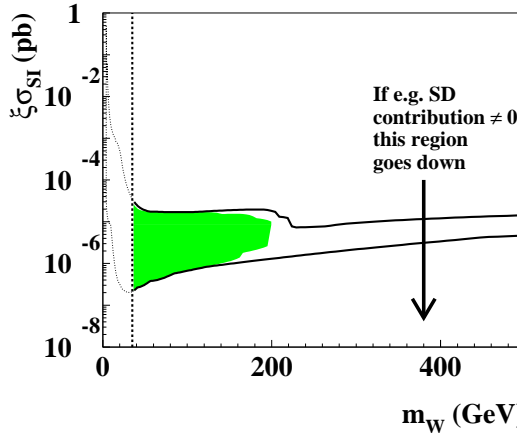


Figure 28: *Case of a WIMP with dominant SI interaction for the model frameworks given in the text.* Region allowed in the plane $(m_W, \xi\sigma_{SI})$. See §7.2; the vertical dotted line represents the model dependent prior discussed in §7.1.8. The area at WIMP masses above 200 GeV is allowed for low local velocity – $v_0=170\text{km/s}$ – and all considered sets of parameters by the Evans’ logarithmic $C1$ co-rotating halo model, by the Evans’ logarithmic $C2$ co-rotating halo model, by the triaxial $D2$ and $D4$ non-rotating halo models and also by the Evans power-law $B3$ model with parameters of the set A). The inclusion of other existing uncertainties on parameters and models (as previously discussed to some extent in this paper) would further extend the region; for example, the use of more favourable SI form factor for Iodine (see §7.1.4) alone would move it towards lower cross sections.

annual modulation effect observed is also compatible – for $m_W \simeq 40 - 75$ GeV – with a WIMP candidate with no SI interaction at all in this particular model framework.

These arguments clearly show that also a relatively small SD contribution can drastically change the allowed region in the $(m_W, \xi\sigma_{SI})$ plane; therefore, e.g. there is not meaning in the bare comparison between regions allowed in experiments that are also sensitive to SD coupling and exclusion plots achieved by experiments that are not. The same is when comparing regions allowed by experiments whose target-nuclei have unpaired proton with exclusion plots quoted by experiments using target-nuclei with unpaired neutron when the SD component of the WIMP interaction would correspond either to $\theta \simeq 0$ or $\theta \simeq \pi$.

7.2.3 WIMPs with dominant SD interaction in some of the possible model frameworks

Let us now focus on the case of a candidate with purely spin-dependent coupling to which DAMA/NaI is – as mentioned – fully sensitive.

When the SD component is different from zero, a very large number of possible configurations is available (see §7.1.1). In fact, in this scenario the space of free parameters is a 3-dimensional volume defined by $m_W, \xi\sigma_{SD}$ and θ (which can vary from

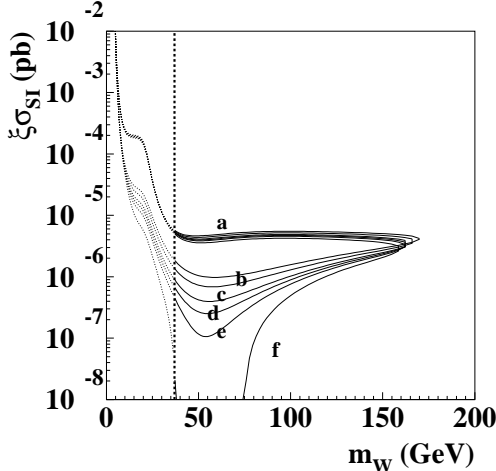


Figure 29: Example of the effect induced by the inclusion of a SD component different from zero on the allowed regions given in the plane $\xi\sigma_{SI}$ vs m_W . In this example the Evans' logarithmic axisymmetric $C2$ halo model with $v_0 = 170$ km/s, ρ_0 equal to the maximum value for this model (see Table 7) and the set of parameters A have been considered. The different regions refer to different SD contributions for the particular case of $\theta = 0$: $\sigma_{SD} = 0$ pb (a), 0.02 pb (b), 0.04 pb (c), 0.05 pb (d), 0.06 pb (e), 0.08 pb (f). See §7.2; the vertical dotted line represents the model dependent prior discussed in §7.1.8.

0 to π). Here, for simplicity as already done in §7.2.1, we show the results obtained only for 4 particular couplings, which correspond to the following values of the mixing angle θ : i) $\theta = 0$ ($a_n = 0$ and $a_p \neq 0$ or $|a_p| >> |a_n|$); ii) $\theta = \pi/4$ ($a_p = a_n$); iii) $\theta = \pi/2$ ($a_n \neq 0$ and $a_p = 0$ or $|a_n| >> |a_p|$); iv) $\theta = 2.435$ rad ($\frac{a_n}{a_p} = -0.85$).

Fig. 30 shows the regions allowed in the plane $(m_W, \xi\sigma_{SD})$ for the same model frameworks quoted above; other configurations are possible varying the θ value. The area at WIMP masses above 200 GeV is allowed for low local velocity – $v_0=170$ km/s – and all considered sets of parameters by the Evans' logarithmic $C2$ co-rotating halo model.

Moreover, the accounting for the uncertainties e.g. on the spin factors as well as different possible formulations of the SD form factors would extend the allowed regions, e.g. towards lower $\xi\sigma_{SD}$ values.

Finally, $\xi\sigma_{SD}$ lower than those corresponding to the regions shown in Fig. 30 are possible also e.g. in case of an even small SI contribution, as shown in Fig. 31.

7.2.4 WIMPs with *preferred* inelastic interaction in some of the possible model frameworks

An analysis considering the same model frameworks has been carried out for the case of WIMPs with *preferred* inelastic interaction (see §7.1.2).

In this inelastic Dark Matter scenario an allowed volume in the space $(\xi\sigma_p, m_W, \delta)$ is obtained. For simplicity, Fig. 32 shows slices of such an allowed volume at some

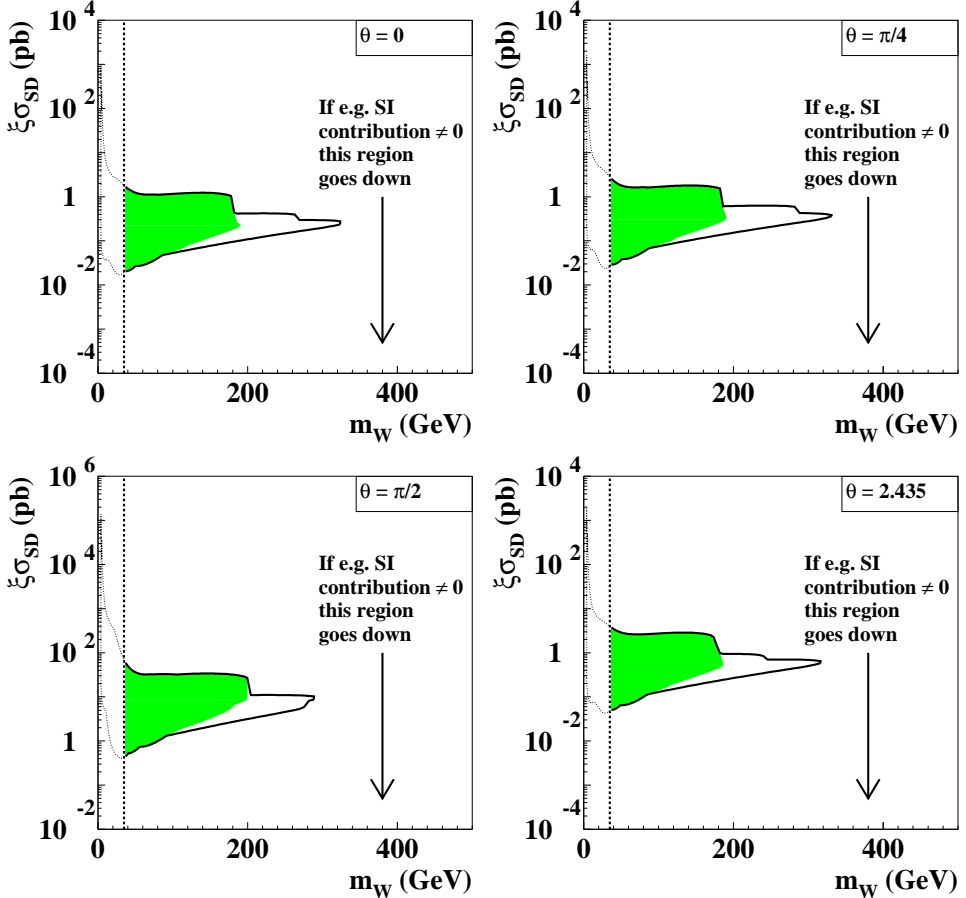


Figure 30: *Case of a WIMP with dominant SD interaction in the model frameworks given in the text.* Regions allowed in the plane $(m_W, \xi\sigma_{SD})$. See §7.2; the vertical dotted line represents the model dependent prior discussed in §7.1.8. The panels refer to only few particular cases for θ (which can instead vary between 0 and π). The area at WIMP masses above 200 GeV is allowed for low local velocity – $v_0=170\text{km/s}$ – and all considered sets of parameters by the Evans' logarithmic $C2$ co-rotating halo model. Inclusion of other existing uncertainties on parameters and models (as previously discussed to some extent in this paper) would further extend the regions; for example, the use of more favourable SD form factors (see §7.1.4) alone would move them towards lower cross sections.

given WIMP masses.

There the superpositions of the allowed regions obtained, when varying the model framework within the considered set, are shown for each m_W . As a consequence, the cross section value at given δ can span over several orders of magnitude. The upper border of each region is reached when v_{thr} approximates the maximum WIMP velocity in the Earth frame for each considered model framework. It can also be noted that when $m_W \gg m_N$, the expected differential energy spectrum is trivially

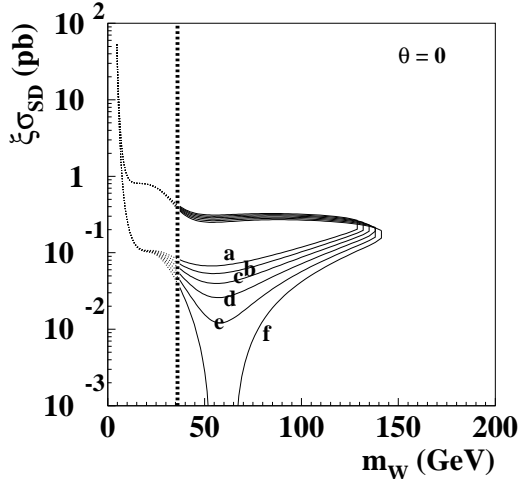


Figure 31: Example of the effect induced by the inclusion of a SI component different from zero on the allowed regions in the plane $\xi\sigma_{SD}$ vs m_W . In this example the Evans' logarithmic axisymmetric C2 halo model with $v_0 = 170$ km/s, ρ_0 equal to the maximum value for this model (see Table 7) and the set of parameters A for $\theta = 0$ have been considered. The different regions refer to different SI contributions with: $\sigma_{SI} = 0$ pb (a), 2×10^{-7} pb (b), 4×10^{-7} pb (c), 6×10^{-7} pb (d), 8×10^{-7} pb (e), 10^{-6} pb (f). See §7.2; the vertical dotted line represents the model dependent prior discussed in §7.1.8.

dependent on m_W and, in particular, it is proportional to the ratio between $\xi\sigma_p$ and m_W ; therefore for very high mass the allowed region can be obtained straightforward. We remind that in these calculations v_{esc} has been assumed at fixed value, while its present uncertainties can play a significant role in the scenario of WIMP with *preferred inelastic* scattering as mentioned in §7.1.2.

Note that each set of values (within those allowed by the associated uncertainties) for the previously mentioned parameters gives rise to a different expectation, thus to a different best fit values. As an example we mention the best fit values for $m_W = 70$ GeV in the NFW B5 halo model with $v_0 = 170$ km/s, maximal ρ_0 in this model and parameters as in case B): ($\delta = 86^{+6}_{-8}$) keV and $\xi\sigma_p = (1.2 \pm 0.2) \times 10^{-5}$ pb.

7.2.5 Conclusion on the quest for a candidate in some of the possible model frameworks

In this section the possible nature of a candidate, which could account for the observed model independent evidence, has been investigated by exploring – as already done on the partial statistics [60, 61, 62, 63, 64, 65, 66, 11] – various kinds of possible couplings and some (of the many) possible model frameworks.

We stress that, although several scenarios have been investigated, the analyses are not exhaustive at all of the existing possibilities because of the poor present knowledge on many astrophysical, nuclear and particle physics assumptions and related parame-

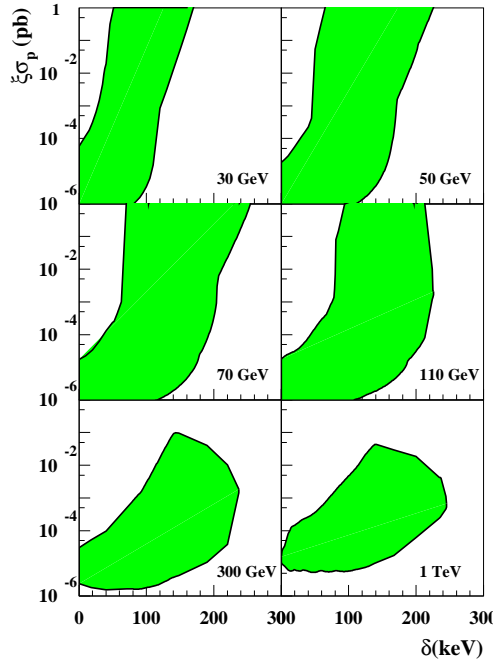


Figure 32: *Case of a WIMP with preferred inelastic interaction in the model frameworks given in the text.* Examples of slices (colored areas) of the allowed volumes ($\xi\sigma_p$, δ , m_W) for some m_W values for the considered model frameworks for WIMP with *preferred* inelastic interaction. See §7.2. In these calculations v_{esc} has been assumed at fixed value, while its present uncertainties would play a significant role in the obtained results. Inclusion of other existing uncertainties on parameters and models (as previously discussed to some extent in this paper) would further extend the regions; for example, already the use of a more favourable SI form factor for Iodine (see §7.1.4) alone would move them towards lower cross sections.

ters as well as of the existing uncertainties in the determination of some experimental parameters which are necessary in the calculations. For example, other parameters values can be considered for the investigated halo models as well as other different halo models too, other form factors and related parameters, other spin factors etc.. We remind that analogous uncertainties are present in every model dependent result (such as e.g. exclusion plots and WIMP parameters from indirect searches); thus, intrinsically, bare comparisons have always only a very relative meaning.

The discussion, carried out in this section, has also allowed to introduce the main general arguments related to the model dependent calculations in WIMP direct searches.

8 Conclusion

In this paper general aspects of the Dark Matter direct search have been reviewed in the light of the activity and results achieved by the DAMA/NaI experiment at the Gran Sasso National Laboratory of I.N.F.N.. DAMA/NaI has been a pioneer experiment running at LNGS for several years and investigating as first the WIMP annual modulation signature with suitable sensitivity and control of the running parameters. During seven independent experiments of one year each one, it has pointed out the presence of a modulation satisfying the many peculiarities of a WIMP induced effect, reaching a significant evidence. As a corollary result, it has also pointed out the complexity of the quest for a WIMP candidate because of the present poor knowledge on the many astrophysical, nuclear and particle physics aspects.

As regards other experiments – to have a realistic comparison – experiments investigating with the same sensitivity and control of the running condition the annual modulation signature are necessary. Of course, the target nuclei also play a crucial role, since they can offer significantly different sensitivities depending e.g. on the nature of the WIMP particle and on their nuclear properties.

The growing in the field of serious and independent efforts searching for WIMP model independent signatures will certainly contribute to increase the knowledge in the field as well as efforts to more deeply investigate models and parameters.

Some of the most competitive activities for the near future, exposing a significantly large target-mass, are starting at the Gran Sasso National Laboratory: CUORICINO, GENIUS-TF (which will also be devoted to the investigation of double beta decay processes) and our new experiment DAMA/LIBRA. In fact, on our behalf, after the completion of the data taking of the $\simeq 100$ kg NaI(Tl) set-up (on July 2002), as a result of our continuous efforts toward the creation of ultimate radiopure set-ups, the new DAMA/LIBRA has been installed (see ref. [139]). The LIBRA set-up is made by 25 NaI(Tl) detectors, 9.70 kg each one. The new detectors have been realised thanks to a second generation R&D with Crismatec/SaintGobain company, by exploiting in particular new radiopurification techniques of the NaI and TlI selected powders. In the framework of this R&D new materials have been selected, prototypes have been built and devoted protocols have been fixed and used. The whole installation has largely been modified. This new DAMA/LIBRA set-up, having a larger exposed mass and an higher overall radiopurity, will offer a significantly increased sensitivity to contribute to further efforts in improving the understanding of this field.

9 Acknowledgements

The authors take this opportunity to thank those who significantly contributed to the realization of the DAMA/NaI experiment. In particular, they thank the INFN Scientific Committee II for the effective support and control and the INFN – Sezione Roma2, the INFN – Sezione Roma, the Gran Sasso National Laboratory and the IHEP/Beijing for the continuous assistance. They are also indebted to the referees of the experiment in that Committee, that allowed them several times to improve the quality of their efforts, and to the Directors and to the coordinators of the INFN involved units for their support. They thank Dr. C. Arpesella, Ing. M. Balata, Dr.

M. Laubenstein, Mr. M. De Deo, Prof. A. Scacco and Prof. L. Trincherini, for their contribution to sample measurements and related discussions and Prof. I. R. Barabanov and Prof. G. Heusser for many useful suggestions on the features of low radioactive detectors. They also wish to thank Dr. M. Amato, Prof. C. Bacci, Mr. V. Bidoli, Mr. F. Bronzini, Dr. D.B. Chen, Prof. L.K. Ding, Dr. W. Di Nicolantonio, Dr. H.L. He, Dr. G. Ignesti, Dr. V. Landoni, Mr. G. Ranelli, Dr. X.D. Sheng, Dr. G.X. Sun and Dr. Z.G. Yao for their contribution to the collaboration efforts in various periods and Dr. M. Angelone, Dr. P. Batistoni and Dr. M. Pillon for their effective collaboration in the neutron measurements at ENEA-Frascati. They thank Dr. R. McAlpine and Dr. T. Wright, from EMI-THORN/Electron-Tubes, for their competent assistance and the Crismatec company for the devoted efforts in the realization of the low background NaI(Tl) crystals. They also thank Mr. A. Bussolotti and A. Mattei for their qualified technical help and the LNGS, INFN – Sezione di Roma and INFN – Sezione di Roma2 mechanical and electronical staffs for support as well as the ACF, GTS, SEGEA staffs for the effective support in hardware works and assistance. They thank Prof. A. Bottino, Dr. F. Donato, Dr. N. Fornengo and Dr. S. Scopel for useful discussions on theoretical aspects. Finally they are grateful to the dark matter community for the continuous discussions about their work and to their families for the patience and forbearance demonstrated in helping to manage them.

References

- [1] F. Zwicky, *Helv. Phys. Acta* 6 (1933) 110
- [2] S. Smith, *Astrophys. J.* 83 (1936) 23
- [3] V.C. Rubin and W.K. Ford, *Astrophys. J.* 159 (1970) 379; M. Roberts and A.H. Rots, *Astron. Astrophys.* 26 (1973) 483
- [4] J.R. Primack, *Nucl. Phys. B* (Proc. Suppl.) 87 (2000) 3 and references therein
- [5] D. N. Spergel et al., *astro-ph/0302209*
- [6] J. E. Ruhl et al., *astro-ph/0212229*
- [7] S. Masi et al., *astro-ph/0201137*
- [8] A. Riess et al., *Astronom. J.* 116 (1998) 1009; E.D. Perlmutter et al., *Astrophys. J.* 517 (1999) 565
- [9] C. L. Bennett et al., *astro-ph/0302207*
- [10] R.A. Flores, *Phys. Lett. B* 215 (1998) 73
- [11] P. Belli et al., *Phys. Rev. D* 66 (2002) 043503
- [12] D.N. Schramm, M.S. Turner, *Rev. Mod. Phys.* 70 (1998) 303
- [13] S. Burles et al., *Astrophys. J.*, 552 (2001) L1; D. Tytler et al., *Physica Scripta*, T85 (2000) 12; O'Meara et al., *Astrophys. J.* 552 (2001) 718
- [14] J.M. Uson, *Nucl. Phys. B* (Proc. Suppl.) 87 (2000) 31 and references therein
- [15] C. Alfonso et al., *astro-ph/0212176v2* and references therein
- [16] R.A.C. Croft et al., *Phys. Rev. Lett.* 83 (1999) 1092; O. Elgaroy et al. *astro-ph/0204152*
- [17] P. Sikivie, *Nucl. Phys. B* (Proc. Suppl.) 87 (2000) 41

- [18] R. Bernabei et al., *Phys. Lett.* B 515 (2001) 6
- [19] S. Cebrian et al. *Astrop. Phys.* 10 (1999) 397; S. Morijama et al., *Phys. Lett.* B 434 (1998) 147
- [20] J. Preskill, *Phys. Rev. Lett.* 43 (1979) 1365
- [21] G.D. Starkman et al., *Phys. Rev.* D 41 (1990) 3594
- [22] R. Bernabei et al., *Phys. Rev. Lett.* 83 (1999) 4918
- [23] M. Ambrosio et al, Macro collaboration hep-ex/0009002
- [24] F. Cappella et al., *Eur. Phys. J.-direct* C14 (2002) 1
- [25] A.M. Green, *Phys. Rev.* D 63 (2001) 043005; N.W. Evans et al., *Mon. Not. Roy. Astron. Soc.* 318 (2000) 1131
- [26] D. Fargion et al., *Pis'ma Zh. Eksp. Teor. Fiz.* 68, (JETP Lett. 68, 685) (1998); *Astrop. Phys.* 12 (2000) 307
- [27] D. Smith and N. Weiner, *Phys. Rev.* D 64 (2001) 043502
- [28] D. Fargion et al., *Phys. Rev.* D52 (1995) 1828
- [29] B.W. Lee e S. Weinberg, *Phys. Rev. Lett.* 39 (1977) 165
- [30] T. Falk et al., *Phys. Lett.* B339 (1994) 248
- [31] L.J. Hall et al., *Phys. Lett.* B424 (1998) 305
- [32] N. Arkami-Hamed et al., *hep-ph/0007001*
- [33] K. Fushimi et al., *Nucl. Phys.* B35 (Proc. Suppl.) (1994) 400
- [34] P. Belli et al., *Phys. Lett.* B 387 (1996) 222; *Phys. Lett.* B 389 (1996) 783 (err.)
- [35] R. Bernabei et al., *New Journal of Physics* 2 (2000) 15.1
- [36] R. Bernabei, *Prog. Part. Nucl. Phys.* 48 (2002) 263
- [37] M. Ambrosio et al., *Astrop. Phys.* 7 (1997) 109
- [38] P. Belli et al., *Il Nuovo Cimento* A 101 (1989) 959
- [39] M. Cribier et al., *Astrop. Phys.* 4 (1995) 23
- [40] C. Arpesella et al., *Health Phys.* 72 (1997) 629
- [41] R. Bernabei et al., *Il Nuovo Cim.* A112 (1999) 545
- [42] I.R. Barabanov et al., *Nucl. Phys.* B 546 (1999) 19
- [43] G. Heusser, *Annual Rev. of Nucl. and Part. Scie.* 45 (1995) 543
- [44] F.T. Avignone et al., *Nucl. Instr. & Methods* A 292 (1990) 37
- [45] C. Bacci et al., *Astrop. Phys.* 2 (1994) 117
- [46] R. Bernabei et al., *Phys. Lett.* B 389 (1996) 757
- [47] R. Bernabei et al., *Phys. Lett.* B 436 (1998) 379
- [48] CDMS collaboration, *Phys. Rev. Lett.* 84 (2000) 5699
- [49] EDELWEISS collaboration, *Phys. Lett.* B 513 (2001) 15
- [50] C. Bucci et al., Proposal to the Gran Sasso Laboratory for a Second Phase of the CRESST Dark Matter Search, MPI-PhE/2000-04 and update MPI-PhE/2001-02.
- [51] S. Cebrian et al., *Astrop. Phys.* 15 (2001) 79
- [52] D. Cline et al., *Astrop. Phys.* 12 (2000) 373
- [53] K.A. Drukier et al., *Phys. Rev.* D 33 (1986) 3495; K. Freese et al., *Phys. Rev.* D 37 (1988) 3388

- [54] R. Bernabei et al., *Eur. Phys. J.* C28 (2003) 203.
- [55] O. Besida, in the *The dark side of the Universe*, World scientific (1994) 277
- [56] D.P. Snowden-Ifft et al., in the volume *The identification of Dark Matter*, World Sc. (2000) 463
- [57] P. Belli et al., *Il Nuovo Cimento* C 15 (1992) 475
- [58] J.I. Collar and F.T. Avignone, *Phys. Lett.* B 275 (1992) 181; *Phys. Rev.* D 47 (1993) 5238
- [59] R. Bernabei et al., *Il Nuovo Cimento* A 112 (1999) 1541
- [60] R. Bernabei et al., *Phys. Lett.* B 424 (1998) 195
- [61] R. Bernabei et al., *Phys. Lett.* B 450 (1999) 448
- [62] P. Belli et al., *Phys. Rev.* D 61 (2000) 023512
- [63] R. Bernabei et al., *Phys. Lett.* B 480 (2000) 23
- [64] R. Bernabei et al., *Eur. Phys. J.* C18 (2000) 283
- [65] R. Bernabei et al., *Phys. Lett.* B 509 (2001) 197
- [66] R. Bernabei et al., *Eur. Phys. J.* C23 (2002) 61
- [67] P.J.T. Leonard and S. Tremaine, *Astrophys. J.* 353 (1990) 486; C.S. Kochanek, *Astrophys. J.* 457 (1996) 228; K.M. Cudworth, *Astron. J.* 99 (1990) 590
- [68] P. Belli et al., *Il Nuovo Cimento* C 19 (1996) 537
- [69] P. Belli et al., *Astrop. Phys.* 5 (1996) 217 ; R. Bernabei et al., *Astrop. Phys.* 7 (1997) 73 ; R. Bernabei et al., *Il Nuovo Cimento* A 110 (1997) 189 ; R. Bernabei et al., *Phys. Lett.* B 408 (1997) 439 ; P. Belli et al., *Astrop. Phys.* 10 (1999) 115; P. Belli et al., *Nucl. Phys.* B 563 (1999) 97 ; P. Belli et al., *Phys. Lett.* B 465 (1999) 315 ; P. Belli et al., *Phys. Rev.* C60 (1999) 065501; P. Belli et al., *Phys. Rev.* D 61 (2000) 117301 ; R. Bernabei et al., *Phys. Lett.* B 493 (2000) 12 ; R. Bernabei et al., *Phys. Lett.* B 527 (2002) 182 ; R. Bernabei et al., *Nucl. Phys.* A 705 (2002) 29 ; R. Bernabei et al., INFN/AE-01/19, to appear on XENON-01, World Sci. Pub.; R. Bernabei et al., *Phys. Lett.* B 546 (2002) 23 P.Belli et al *Nucl. Instr. & Methods* A 498 (2003) 352
- [70] R. Bernabei et al., *Nucl. Instr. & Methods* A 482 (2002) 728
- [71] P. Belli et al., *Phys. Lett.* B460 (1999) 236
- [72] R. Bernabei et al., *Eur. Phys. J. direct* C11 (2001) 1
- [73] P. Belli, R. Bernabei, C. Bacci, A. Incicchitti, R. Marcovaldi, D. Prosperi, DAMA proposal to INFN Scientific Committee II, April 24th 1990.
- [74] A. D'Ambrosio and S. d'Angelo, ROM2F/1998-07
- [75] S. d'Angelo and L. Zanotti, private communication
- [76] R. Cerulli, Ph.D. thesis, Universita' di "Tor Vergata" 2002
- [77] P. Belli, talk at TAUP 97, LNGS (1997); R. Bernabei et al., *Nucl. Phys.* B (Proc. Suppl.) 70 (1999) 79
- [78] D.E. Groom et al., *Eur. Phys. J.* C 15 (2000) 1
- [79] A. Bottino et al., *Phys. Lett.* B 402 (1997) 113 ; *Phys. Lett.* B 423 (1998) 109 ; *Phys. Rev.* D 59 (1999) 095004 ; *Phys. Rev.* D 59 (1999) 095003 ; *Astrop. Phys.* 10 (1999) 203 ; *Astrop. Phys.* 13 (2000) 215 ; *Phys. Rev.* D 62 (2000) 056006 ; *Phys. Rev.* D 63 (2001) 125003 ; *Nucl. Phys.* B 608 (2001) 461

[80] R.W. Arnowitt and B. Dutta, *hep-ph/0211417*; R.W. Arnowitt and P. Nath, *Phys. Rev. D* 60 (1999) 044002; E. Gabrielli et al., *Phys. Rev. D* 63 (2001) 025008; E. Accomando et al., *Nucl. Phys. B* 585 (2000) 124

[81] N. Smith, talk given at IDM02, York, september 2002

[82] P. Belli et al., in the volume “Relativistic Astrophysics”, 20th Texas Symp., AIP (2001) 95; R. bernabei et al., in the volume “Dark Matter in Astro- and Particle Physics”, Dark2002 (2002) 459; ROM2F/2002/26 to appear in the Proc. of “Beyond the Desert 2002”, Oulu, Finland, available on DAMA homepage on <http://www.lngs.infn.it>

[83] R. Luscher , talk given at Moriond, march 2003

[84] A. Bottino and N. Fornengo: ”Particle candidates for dark matter”, Sixth School on Non-accelerator astroparticle physics (ICTP, Trieste, 2001), (Eds. R.A. Carrigan, G. Giacomelli, A. Masiero and N. Paver, World Scientific 2002), 118

[85] M. Ambrosio et al., *Phys. Rev. D* 60 (1999) 082002

[86] P. Picozza and A. Morselli, *astro-ph/0211286*

[87] G.L. Kane et al., *hep-ph/0108138*

[88] A. Morselli et al., *astro-ph/0211327*

[89] R. Battiston, in the volume “Dark Matter in Astrophysics and Particle Physics” IoP (1998) 815

[90] A. Morselli, talk given at Vulcano 2002

[91] A. Strong et al., *Astrophys. J.* 537 (2000) 763

[92] W. Atwood et al., *Nucl. Instr. & Methods A* 342 (1994) 302

[93] W.H. Press and G. B. Rybicki, *Astrophys. J.* 338 (1989) 277; J.D. Scargle, *Astrophys. J.* 263 (1982) 835

[94] M. Wojcik: *Nucl. Instrum. & Methods* B61 (1991) 8

[95] P. Belli et al., in the volume ”3K-Cosmology”, AIP pub. (1999) 65

[96] *Table of Isotopes*, ed. by C.M. Lederer and V.S. Shirley, 7th ed. (John Wiley, N.Y., 1978)

[97] M. Aglietta et al., *Il Nuovo Cimento* C12 (1987) 467; *hep-ex/9905047*

[98] R. Bernabei et al., *Astrop. Phys.* 4 (1995) 45

[99] A. Bottino et al., *Phys. Lett.* B402 (1997) 113

[100] J. Binney and S. Tremaine, ”Galactic Dynamics” (1987), Princeton Univ. Press.

[101] N.W. Evans, *Mon. Not. R. Astron. Soc.* 260 (1993) 191

[102] N.W. Evans, *Mon. Not. R. Astron. Soc.* 267 (1994) 333

[103] W. Jaffe, *Mon. Not. R. Astron. Soc.* 202 (1993) 995

[104] J.F. Navarro, C.S. Frenk e S.D.M. White, *Astrophys. J.* 462 (1996) 563

[105] B. Moore et al., *Mon. Not. R. Astron. Soc.* 310 (1990) 1147

[106] A. V. Kravtsov et al., *Astrophys. J.* 502 (1998) 48

[107] N.W. Evans, C.M. Carollo and P.T. de Zeeuw, *Mon. Not. R. Astron. Soc.* 318 (2000) 1131

[108] L.P. Osipkov, *Pris'ma Astron* 55 (1979) 77; D. Merritt, *Astrophys. J.* 90 (1985) 1027

- [109] M. Kamionkowski and A. Kinkhabwala, *Phys. Rev.* D57 (1998) 3256
- [110] S. Warren, P. J. Quinn, J. K. Salmon and W. H. Zurek, *Astrophys. J.* 399 (1992) 405; S. Cole and C. Lacey, *Mon. Not. R. Astron. Soc.* 281 (1996) 7126
- [111] W. Dehnen and J. Binney, *Mon. Not. R. Astron. Soc.* 294 (1998) 429
- [112] E. I. Gates, G. Gyuk, M. S. Turner, *Phys. Rev.* D53 (1996) 4138
- [113] C. S. Kochanek, *Astrophys. J.* 457 (1996) 228
- [114] M. Feast and P. Whitelock, *Mon. Not. R. Astron. Soc.* 291 (1997) 683
- [115] R.H. Helm, *Phys. Rev.* 104 (1956) 1466 ; A. Bottino et al., *Astrop. Phys.* 2 (1994) 77
- [116] J. D. Lewin and P.F. Smith, *Astrop. Phys.* 6 (1996) 87
- [117] M.T. Ressell et al., *Phys. Rev.* C 56 (1997) 535
- [118] J. Ellis and R.A. Flores, *Phys. Lett.* B263 (1991) 259
- [119] G. Gerbier et al., *Astrop. Phys.* 11 (1999) 287
- [120] D.R. Tovey et al., *Phys. Lett.* B 433 (1998) 150
- [121] K. Fushimi et al., *Phys. Rev.* C 47 (1993) R425
- [122] R. Hazama et al., *nucl-ex/0107001*
- [123] S. Pécourt et al., *Astrop. Phys.* 11 (1999) 457
- [124] V.A. Kudryavtsev et al., *hep-ex/0005031*
- [125] H. Park et al., *nucl-ex/0202014*
- [126] Y. Messous et al., *Astrop. Phys.* 3 (1995) 361
- [127] A.R. Sattler et al., *Phys. Rev.* 143, 2 (1966) 588
- [128] C. Cashman et al., *Phys. Rev. Lett.* 15 (1965) 245; 21 (1968) 1431
- [129] T. Shutt et al., *Phys. Rev. Lett.* 69 (1992) 3425; 69 (1992) 3531
- [130] G. Gerbier et al., *Phys. Rev.* D 42 (1990) 3211
- [131] A.R. Sattler, *Phys. Rev.* A 138 (1965) 1815
- [132] F. Arneodo et al., *Nucl. Instr. & Methods A* 449 (2000) 147
- [133] D. Akimov et al., *Phys. Rev.* D 524 (2002) 245
- [134] A. Alessandrello et al., *Nucl. Instr. & Methods A* 409 (1998) 451
- [135] A. Bottino et al., *Phys. Rev.* D 67 (2003) 063519 ; A. Bottino et al., *hep-ph/0304080*
- [136] D. Hooper and T. Plehn, MADPH-02-1308, CERN-TH/2002-29, *hep-ph/0212226*
- [137] G. Bélanger, F. Boudjema., A. Pukhov and S. Rosier-Lees, *hep-ph/0212227*
- [138] K. Hagiwara et al., *Phys. Rev.* D 66 (2002) 010001
- [139] for some pictures see the DAMA web site at www.lngs.infn.it